AN ABSTRACT OF THE DISSERTATION OF

Joshua D. Fishler for the degree of Doctor of Philosophy in Nuclear Engineering presented on June 14, 2018.

Title: Experimental Investigation of the Transition to Natural Convection in HTGR Applications using the Oregon State SFSETF.

Abstract approved: ____

Andrew C. Klein

High Temperature Gas Reactors (HTGRs) are positioned to disrupt local and global markets via their unique ability to produce carbon-free process heat, high efficiency power generation, and passively safe operational features. However, significant impediments still exist to delay deployment of this particular technology, including a lack of experimental data, verified code application, and lack of consensus with regards to severe accident progression. In particular, air ingress accidents represent a particular challenge to designers and engineers, as they represent low probability, but highly complex, accident scenarios. Including phenomena such as molecular diffusion, free convection, and complex heat and mass transfer paths, experimental and traceable data is essential to maturing the state of the industry. Therefore, this work presents an experimental investigation of the transition to natural convection in HTGR applications using the Stratified Flow Separate Effects Test Facility, housed at Oregon State University. In particular, this work will present data that challenges the assumption that molecular diffusion is a significant factor in this severe accident in the reference facility of the General Atomic 600 MW_{th} Gas Turbine-Modular Helium Reactor (GT-MHR). Rather, pre-existing convective currents, produced via thermal gradients within coolant channels and at the core

barrel wall, will drive convective flow within the core region, and any diffusive action is due to precluding air access to those currents. This will be done using a simplified cross duct that may be positioned in one of two ways so as to provide either horizontal or vertical access to the lower plenum area. Onset of natural convection (ONC) is measured using an oxygen sensor probe, immersed in the helium working fluid, so as to provide direct indication of air presence in the upper plenum.

Experimental Investigation of the Transition to Natural Convection in HTGR Applications using the Oregon State SFSETF

by

Joshua D. Fishler

A DISSERTATION

submitted to

Oregon State University

in partial fulfillment of

the requirements for the

degree of

Doctor of Philosophy

Presented June 14, 2018

Commencement June 2019

Doctor of Philosophy dissertation of Joshua D. Fishler presented on June 14, 2018

APPROVED:

Major Professor, representing Nuclear Engineering

Head of the School of Nuclear Science and Engineering

Dean of the Graduate School

I understand that my dissertation will become part of the permanent collection of Oregon State University libraries. My signature below authorizes release of my dissertation to any reader upon request.

Joshua D. Fishler, Author

ACKNOWLEDGEMENTS

It is with the deepest sincerity and gratitude that I acknowledge the support of my wife, Hillary. She has sustained me in the darkest moments, and comforted me when all seemed lost. She has helped, silently and lovingly, in ways that I did not know that I needed. For all the meals I did not make, for all dog-walking I did not do, and for all the small and weary maintenance I did not complete – thank you. This couldn't have been done without her tending for all the things that I could not.

Thank you.

Additionally, I would like to acknowledge the patient guidance and support of Dr. Andrew Klein. There are few people who would take the risks that he has on my research, or committed to it as fully as he has. He has also been the example that patience and silent effort over time, even in the face of great and (seemingly) crushing challenge, will give way to something marvelous. Similarly, I'd like to thank the other members of committee: Dr. Brian Woods, Dr. Wade Marcum, Dr. Sourabh Apte, and Dr. Henri Jansen.

Thank you.

Last, but certainly not least, I would like to thank Ian White, Michael Castillo, and Matt Hertel. This could not have been done without their help, and all credit that is due to me belongs rightfully with them. And, should any happen to read this, I would like them all to know that I think they are all excellent engineers, technicians, and scientists, and I have tried very hard to learn from your examples. You were better than I could have asked.

Thank you.

TABLE OF CONTENTS

TABLE OF CONTENTS (Continued)

TABLE OF CONTENTS (Continued)

LIST OF FIGURES

LIST OF FIGURES (Continued)

LIST OF FIGURES (Continued)

LIST OF TABLES (Continued)

1 Introduction

High temperature gas reactors (HTGRs) are poised to contribute to the next generation of nuclear energy. Featuring very high operational temperatures, facilities like the General Atomics Gas Turbine – Modular Helium Reactor (GT-MHR), can generate chemically and radiologically stable helium at temperature in excess of 1200C [1]; however, they also pose commensurate challenges. In no particular order, they face the following, which do not in any way represent the totality of challenges, but rather a helpful sampling:

i. Lack of historical development and decades of federal support.

ii. Lack of operational data with respect to critical safety systems and components.

iii. Lack of experimental data regarding normal and off-normal operational conditions.

Several gap analyses support these gaps in the industry expertise, and have been performed by numerous researchers and industry experts [2].

1.1 Motivation

Significant progress has been made recently with respect to addressing the gaps of knowledge.

This work investigates the air ingress scenario, which is of particular concern to HTGR facilities. Defined similarly to a depressurized conduction cooldown, an air ingress accident additionally features a significant volume of ambient fluid ingress – a useful analogy with respect to the light water reactors (LWRs) may be the double-ended guillotine break.

While the details of this particular accident will be discussed later, it is worth mentioning that such an accident poses a critical threat to any HTGR facility across the following formats:

i. Loss of forced convection via scram, as well as communication path to the heat sink/turbine present a threat to core thermal rejection.

ii. Large opening on the coaxial cross duct allows ambient fluid to ingress and interact with core support structures, presenting a chemical threat to those components.

iii. Potential oxidation reactions are exothermic, and may present a threat to core heat generation, in addition to the expected amount of decay heat.

These challenges have given way to numerous experimental thermal-hydraulic studies; some are integrated effects test facilities that seek to reproduce dominant physical phenomena over the whole (or partial) duration of a transient event. Such efforts as the High Temperature Test Facility (HTTF) at Oregon State University, the 1/8th Facility at Ohio State University, as well as the NACOK facility are all examples of such efforts. However, separate effects test facilities have also grown to meet these challenges. These facilities only seek to examine limited physical processes, capturing in part what the IETFs present in whole.

Such approaches are often useful in examining scenarios that defy straightforward simulation and/or interpretation within the context of a larger facility. Air ingress scenarios are an excellent example, as they are a significant challenge to describe physically, and the dominant parameters surrounding them are not clear.

Previous studies, especially those produced by IETF efforts, present a four stage process to describe the dominant physics in each stage of an air ingress accident, outlined below:

i. Depressurization, down from operation pressure (12 MPa) to assumed ambient (or equilibrium pressure in containment).

ii. Stratified shear flow, as ambient air ingresses into the lower plenum.

iii. Diffusion, front propagation upwards through the core region, driven by chemical diffusion.

iv. Natural convection, a global current will establish, drawing yet further air into the core region.

The duration of time necessary for this series of events to happen, defined here as the *natural convection onset time*, is of significant interest to design, operational, and regulatory personnel. Estimates form previous works, like JAERI a la Hishida and Takeda [3] estimate such values on the order of minutes: 100 min for a hot leg temperature of 750C, for example. Others present confident estimations on the order of days, 100 hours [4] by some estimates.

This variation highlights not only experimental differences with respect apparatus configuration, which is to be expected, but perhaps also first order biasing of results based on those expectations. Oh and Kim present analyses to suggest that diffusion bias is possible via comparisons of duct height and front height [5].

1.2 Experimental Objectives

The objective of this work is to isolate, examine, and quantify the role of cross duct orientation on the onset of natural convection. It is the hypothesis of this work that this particular boundary condition, cross duct injection, plays a critical role in determining ingress mechanisms, and therefore onset time of global natural convection within the primary pressure vessel. This hypothesis will be interrogated through an experimental effort that is presented in the following steps:

1. Implement a scaling analysis using the Hierarchical Two-Tiered Methodology in order to maintain applicability of experimental results, and inform design efforts.

2. Generate experimental data from Stratified Flow Separate Effects Test Facility (SFSETF) according to an experimental program focused on cross duct orientation effects.

3. Compare experimental data to relevant scaling parameter(s) in order to establish correlation according to dimensionless parameter and/or boundary conditions.

1.3 Document Overview

This document is organized as follows:

Chapter 1: Introduction – Introduction to the topic and motivation for the work.

Chapter 2: Survey of Literature – Background information, a survey of available literature on related topics, including: integral effects test facilities, separate effects test facilities, other related experimental efforts, free convection, HTGRs, and air ingress.

Chapter 3: Hypothesis – This brief section clearly states the experimental hypothesis of this research effort, and provides additional clarification via the Thesis Statement subsection.

Chapter 4: Model and Methodology – Comprehensive description of experimental apparatus used to investigate the experimental hypothesis, the Stratified Flow Separate Effects Test Facility (SFSETF). The Hierarchical Two-Tiered (H2TS) scaling analysis is presented, along with relation to design efforts. Further analysis regarding design stage uncertainty and experimental procedure are also discussed.

Chapter 5: Results and Observations – Presentation of experimental data and discussion of the phenomena captured as a part of this work. Broader observation regarding facility behavior are also captured in this section.

Chapter 6: Conclusion – Concluding remarks and observations relevant to this dissertation work, and commentary on future work areas to extend its applicability and improve data quality.

Appendix A: Shakedown Testing and Lessons Learned – This section captures the quantification of experimental quantities, including mass leakage and upper plenum thermal inertia. Additionally, the lessons learned regarding sealing efforts, as well as the design calculations for the sealing augmentation, are provided.

This document concludes with lists of referenced works, relevant nomenclature and symbols, and appendices with additional details and documentation either not captured in this document, or beyond its scope.

2 Survey of Literature

HTGRs are certainly unique among advanced reactor platforms. While some reactor types have seen significant scientific interest, HTGRs are singular in the continuity of their devotees, in addition to their shared academic and technical pedigrees, as well as their operational history. Where some formats see limited development, sometimes limited to the draft stage, HTGRs have seen significant deployment, sufficient to generate unique design features across various efforts. This section seeks to examine a portion of those formats and features via a survey of the literature, with a specific focus on previous and/or concurrent research efforts in a similar setting.

2.1 HTGR Overview

This section provides a comprehensive overview of HTGR facilities, and provide descriptions of the reference facility for this work: the General Atomics Gas Turbine – Modular Helium Reactor (GT-MHR).

The GT-MHR facility was developed by General Atomics, beginning in 1995 [6], with the objective of providing a passively safe, economic nuclear commercial power generation facility, each consisting of four (4) identical 550 MW_{th} reactors. Each reactor would be licensed to 600 MW_{th}.

Motivated by the reduction in plant equipment, among other financial considerations, General Atomics cited reduced staffing requirements, facility cost reduction, and high degree of modularization as key concepts in the development of this technology. A unit module consists of a reactor connected to a power conversion system, which is deliberately placed below grade of the reactor unit. This is shown in Figure 1.

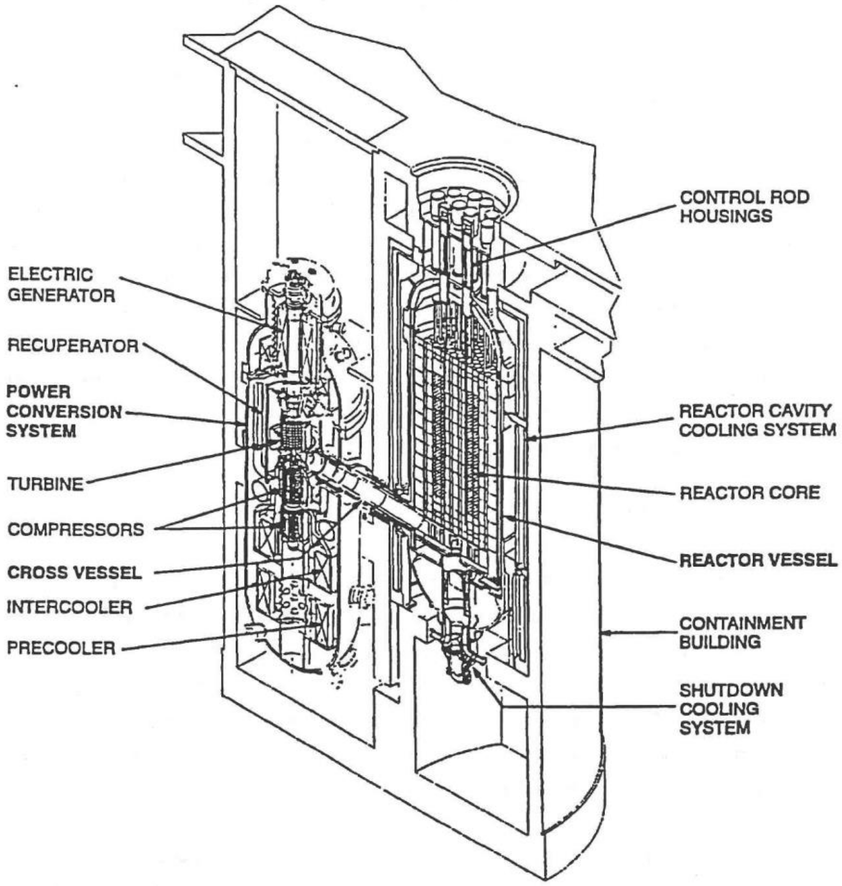

Figure 1. Cut away view of GT-MHR unit module.

This facility, while not the only such design, is representative of general facility layouts. Consider this facility shown in Figure 2, from FRAMATOMME (previously AREVA). Of course, these facilities are should be considered alongside Fort St. Vrain facility of blessed memory [7].

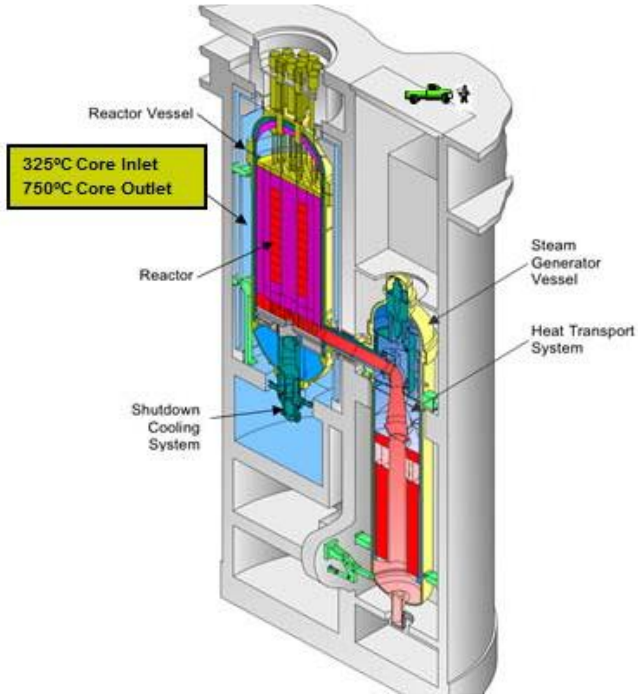

Figure 2. Cut away view of a FRAMATOMME facility design.

HTGR facilities, as one may clearly see, differ from Light Water Reactors in several ways, many of which are not worth examining here. However, Table 1 outlines several operational (or design, if appropriate) characteristics of LWR and HTGR types [8].

Table 1. Typical characteristics of a PWR and HTGR facility.

Characteristic	*PWR*	*HTGR*
Manufacturer/Station	Westinghouse/Sequoyah	General Atomic/Fulton
Gross Thermal Power (MW_{th})	3579	3000
Moderator	H_2O	Helium
Primary Coolant	H_2O	Graphite
Secondary Coolant	H_2O	H_2O
Primary Coolant		
Pressure (MPa)	15.5	4.90
Inlet Temp (C)	286	348
Avg. Outlet Temp (C)	324	741

Secondary Coolant		
Pressure (MPa)	5.7	17.2
Inlet Temp (C)	224	188
Avg. Outlet Temp (C)	273	513

The high temperature helium, even at the modest 740C reported here, is the primary factor of interest, as one might expect from a High Temperature Gas Reactor (HTGR). This is of interest primarily due to its application as process heat. In fact, colocation of a nuclear facility and industrial users (say, petrochemical, chemical processing, metallurgical, or other energy-intensive processes) is an area of research that has seen significant development and advocacy over several years [9] in order to reduce greenhouse gas emissions on a national scale.

2.2 HTGR Research Efforts

2.2.1 Definition of Air Ingress Accident

Air Ingress Accident: An air ingress event is an off-normal event occurring in HTGR facilities that requires the following conditions:

i. Loss of forced convection.

ii. Loss of primary pressure boundary integrity, leading to primary system depressurization.

iii. Significant ingress of air, or ambient fluid, mass.

In some instances, this work included, this event may describe a double-ended guillotine break of the coaxial cross duct, shown in Figure 1 as the “Cross Vessel” in General Atomics’ Design Description Report [6].

For the purposes of this work, the following conditions are also assumed:

i. Reactor Core Cooling System (RCCS) is both functional, available, and operating at nominal capacity.

ii. Complete loss of helium inventory to the atmosphere – zero mass retention within containment following depressurization.

The following basis presents the basis for this decision, as it speaks to a greater context surrounding the HTGR and advanced reactor community, generally.

2.2.2 Regulatory Influence

HTGR research and development has experienced, as all nuclear technology has, a significant degree of interface with national regulatory body: the United States Nuclear Regulatory Commission. While a full description regarding the scope and magnitude of the NRC's influence and motivations is well beyond the scope of this document, it is important to acknowledge the ways it has interacted and influenced this work.

HTGRs, as a nuclear technology, may be characterized as a fairly mature technology. However, if it is mature, then the regulatory framework surrounding it has not matured at the same pace, leaving a critical knowledge and experience gap that may severely challenge the NRC's ability to respond to advanced reactor types. This was initially addressed via the Next Generation Nuclear Plant (NGNP) Project, which sought to bring HTGR technology to deployment by 2020. Simultaneously, this effort was a nominal opportunity to develop regulatory familiarity and expertise regarding this reactor type and address some of the challenges, many falling into the following categories:

i. Establishing an acceptable HTGR licensing basis

ii. Establishing a technical bases for the plant safety analysis

iii. Reviewing HTGR applications in pebble bed configurations

These are very broad, but this may largely be summarized as follows: the NRC has spent its operational history developing expertise to review LWR applications, and the institutional body of knowledge to regulate and review HTGR applications (and other advanced reactor concepts) does not exist. While this challenge is daunting, significant efforts have risen to address it, and have done so from an early stage. Numerous researchers housed at INL and elsewhere, in the 2010 INL/EXT-10-19521, "*Licensing Basis Event Selection,"* document, the approach to select licensing basis events was described. Of particular interest are the following definitions:

i. Anticipated operational occurrence (AOO) – event sequences with mean frequencies > 10^{-2}/plant-year.

ii. Design basis events (DBE) – event sequences with mean frequencies < 10^{-2}/plant-year, and >10^{-4}/plant-year.

iii. Beyond design basis events (BDBEs) – event sequences with mean frequencies < 10^{-4}/plant-year, and > 5 x 10^{-7}/plant-year.

These criteria are consistent with evolving efforts to adopt a probabilistic rather than deterministic regulatory perspective. However, certain similarities continue to persist with respect to accident definition. That is, if an analog exists in an LWR application, it should be considered in HTGRs in the same fashion as in LWRs. This is captured quite elegantly in the SECY-93-092 policy statement [10], "*Issues Pertaining to the Advanced Reactor (PRISM, MHTGR, and PIUS) and CANDU 3 Designs and Their Relationship to Current Regulatory Requirements,"* where it is very clearly specified that:

External events will be chosen deterministically on a basis consistent with that used for LWRs.

This is a particularly challenging position for designers for a variety of reasons, many of which are beyond this document. However, it is of interest to examine the feedback and NRC position regarding regulator-imposed bounding conditions:

'In this regard, the SRM specifically directs the staff to consider "chimney-effect" air ingress events (i.e., concurrent with helium pressure boundary breaks above and below the core).'

This may be interpreted to mean that the regulatory staff reserves the right to impose 'worst-case scenario' conditions on the designers. That is not to say that it is done so arbitrarily, the next paragraph goes on to say that the selected siting even sequences should be physically plausible event sequences; however, it does drive the need for experimental investigation in plenum-to-plenum heat and mass transfer in these systems, as that will drive the rate of air in-leakage.

But to summarize the significance of this regulatory overview to this work, consider this: Definitive boundary conditions for air-ingress scenarios have not been issued by the Nuclear Regulatory Commission. Moreover, given the regulatory history of the Commission, in addition to the conservatism bias implicit to most nuclear engineering applications, an excessively conservative experimental program, and commensurate initial/boundary conditions, was deliberately chosen.

While a case may be made that such events as the air-ingress scenario need not be considered as a BDBE, the work of Syd Ball and Matt Richards [11] would be an example of such a case. In fact, based on parameterized studies from the same research group, one may well argue that sufficient delay exists, as well as sufficient design confidence in penetration selection, so as to preclude this from even BDBE occurrence ranges. However, as current researchers engaged in such arguments acknowledge that it Commission consideration is still required [12].

This of course begs the following question: Why consider the air-ingress scenario as a credible threat to HTGR safety?

While a comprehensive and definitive answer is beyond the expertise of the author, one might hazard the following design bases as motivations to this, and future, work:

i. The facility design as selected by the NGNP, and therefore the model of this research, features a horizontally oriented coaxial inlet/outlet line: The Cross Duct. Such a configuration may well remove all passive safety features credited by molecular diffusion, as it permits air ingress via helium displacement rather than diffusion.

ii. Regarding feedback from above regarding pressure boundary failure, a credible situation where a regulator may reasonably require little to no credit taken for the helium inventory in the core being retained in containment exists at time of writing.

iii. If no credit may be taken for the primary helium inventory, and a ‘leak-tight’ containment is not provided, then maximally conservative boundary conditions may be applied by the regulator – historical evidence re: Large break LOCAs support this, as does the Commission’s willingness to treat such external events similarly across technology platforms.

To summarize: Sufficient regulatory uncertainty exists so as to make extremely unlikely accident boundary conditions as reasonable within an experimental context in order to inform future design efforts. Further, a consistent (and probabilistic) regulatory vision for HTGR technology does not currently exist so as to preclude experimental investigation from ongoing V&V needs.

2.3 Previous Experimental Efforts

2.3.1 Definition and Role of Integral Effects Test Facilities

The need for experimental data has been well established by numerous contributors [2]. Unsurprisingly, the needs are both varied and voluminous; integral effects test facilities are a natural response to such broad needs.

Integral effects test facilities are defined as an experimental facility for which the primary interrogative focus is on the interactions between several parameters and processes.

An excellent example of such a facility would the Gas Reactor Test Section (GRTS) [13], which became the High Temperature Test Facility. These integral facilities (usually) implement a form of scaling analysis in order to interrogate transfer rates and then seek to preserve the relative magnitudes of those transfer rates in order to accurately simulate accident progression. This process is called Hierarchical Two-Tiered Scaling Analysis [14]. A general example is provided to illustrate the efficacy of this process.

Consider a conserved property per unit volume (such as mass, linear momentum, or energy), represented as $\boldsymbol{\psi_i}$. This unit occupies volume, $\boldsymbol{V_i}$, and is the ith constituent of the working fluid. The flux driving the transfer process in this example is given $\boldsymbol{j_{ik}}$, as it transfers from the ith constituent to the kth, and $\boldsymbol{A_{ik}}$ represents the transfer area shared by the two constituents. A generalized control volume balance of these variables for the ith constituent may be written as shown in Equation 1.1.

$$\frac{dV_i\psi_i}{dt} = \Delta[Q_i\psi_i] \pm \sum_{k=1}^{m-1} j_{ik}A_{ik} \qquad 1.1$$

Dividing through by initial and boundary conditions, defined as

$$V_i^* = \frac{V_i}{V_{i.0}} \qquad \psi_i^* = \frac{\psi_i}{\psi_{i.0}} \qquad Q_i^* = \frac{Q_i}{Q_{i.0}} \qquad A_i^* = \frac{A_i}{A_{i.0}} \qquad j_i^* = \frac{j_i}{j_{i.0}}$$

Substituting these into Equation 1.1 yields the results presented in Equation 1.2. The important coefficient to note is the time constant, $\boldsymbol{\tau_i}$, which represents the characteristic time constant for the transfer process.

$$\frac{V_{i.0}\psi_{i,o}}{\tau_i}\frac{dV_i^*\psi_i^*}{dt^*} = Q_{i.0}\psi_{i.0}\Delta[Q_i^*\psi_i^*] \pm \sum_{k=1}^{m-1}(j_{ik,0}A_{ik,0})j_{ik}^*A_{ik}^* \qquad 1.2$$

Importantly, dividing through by the convective term on the left hand side, that is, the conserved property and the volume it occupies, produces the dimensionless expression shown in Equation 1.3.

$$\tau_i \frac{dV_i^* \psi_i^*}{dt^*} = \Delta[Q_i^* \psi_i^*] \pm \sum_{k=1}^{m-1} \Pi_{ik}\, j_{ik}^* A_{ik}^* \qquad 1.3$$

$$\tau_i = \frac{V_{i,0}}{Q_{i,0}} \qquad \Pi_{ik} = \frac{j_{ik,0} A_{ik,0}}{Q_{i,o} \psi_{i,0}}$$

The power of this analysis technique is that it provides a systematic way of determining the transfer parameters that influence a process. And, as would surprise no one, one analysis may produce several dimensionless scaling ratios, or Π-groups.

These scaling ratios are evaluated at model and prototypical values, Π_m and Π_p, respectively and the ratio of these values is called the degree of similarity. A value of unity indicates perfect preservation, whereas deviation leads to either acceleration or retardation of the process. An integral effects test facility uses those ratio values, or degrees of similarity, to inform design choices regarding the experimental, or model, facility.

For example, such analysis may demonstrate the importance of maintaining heated length, or power input, or other flow parameter to the importance of transient progression. That is not to say that implementing this analysis will lead all facilities to a similar design – quite the opposite. Rather, this process helps designers and engineers to deliberately make informed choices regarding facility parameters. The following sections present examples of how this process may be used to meaningfully interrogate accident scenarios in an experimental setting.

2.3.2 High Temperature Test Facility – Oregon State University

The HTTF is a 1:4 height and radial scale facility meant to simulate the Gas Turbine Modular Helium Reactor facility designed by General Atomics [1]. Designed to achieve a center core temperature of 1600C, it provides a nominal 2.2 MW of thermal energy to achieve this. Table 2 presents operational conditions for the HTTF under various configurations. Remarkably versatile, the HTTF simulates the following accident scenarios to various degrees of similarity:

i. Pressurized Conduction Cooldown [15]

ii. Depressurized Conduction Cooldown [16]

iii. Air Ingress Mitigations [17]

Table 2. Operating parameters for the HTTF in different configurations.

	Normal	*PCC Config.*	*DCC Config.*
Fluid Temperature (C)	740	1200	1200
Pressure (MPa)	0.8	0.8	0.8
Flow Rate (kg/s)	1.0	0.1	1.0

The general facility layout, shown in Figure 3, features a Reactor Pressure Vessel (RPV), as well as a Reactor Cavity Simulation Tank (RCST). A horizontal cross duct is also shown, which provides access between the two volumes. Heat rejection is provided via the Reactor Cavity Cooling System (RCCS), which features water cooled panels and accepts heat transfer via radiative transfer from the RPV walls.

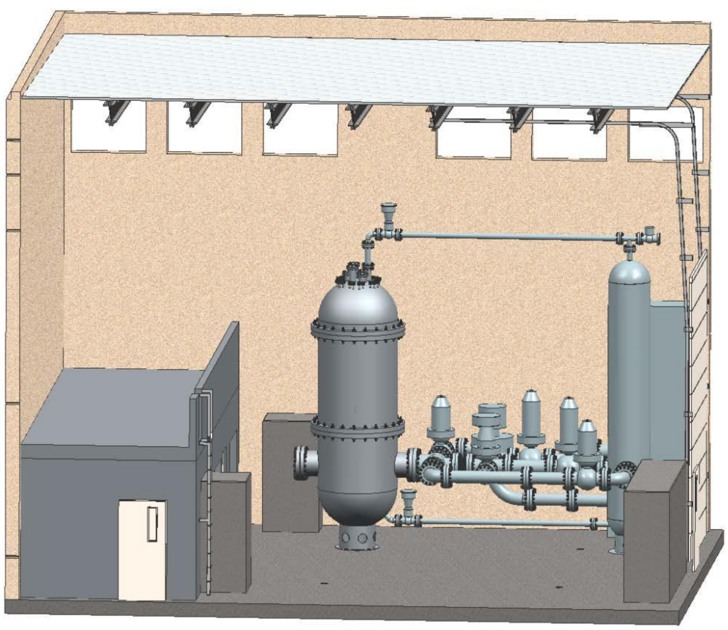

Figure 3. HTTF experimental facility layout, including the RPV (left), the RCST (right), and connecting cross duct.

The core region, which is modular, may be configured in either a prismatic core or pebble bed; however, this work will only concern itself with the prismatic configuration, as no data for the pebble bed setup exists at time of writing. Additionally, this work is unconcerned with pebble bed configurations, generally. The core features ceramic block, as shown in Figure 4, which stack on top of one another to form the core region, which also houses the graphite heaters which supply the operational heat for the facility.

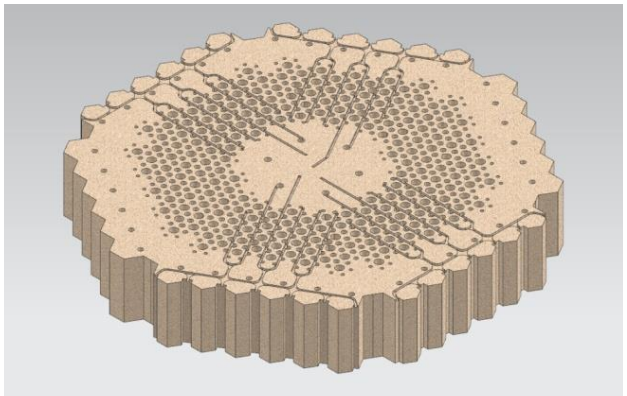

Figure 4. HTTF core block, isometric view.

2.3.3 The NACOK Facility

The NACOK experimental facility was an experimental facility set up by Forschungzentrum Juelich GmbH to examine free convection effects in pebble bed high temperature gas reactor facilities, in particular the “aerodynamic aspects.” [18] As shown in Figure 5, it features an inverted “h-bend” tube, along with a coaxial cross duct connecting the heated channel and return tube. Table 3 presents the operational characteristics of the facility.

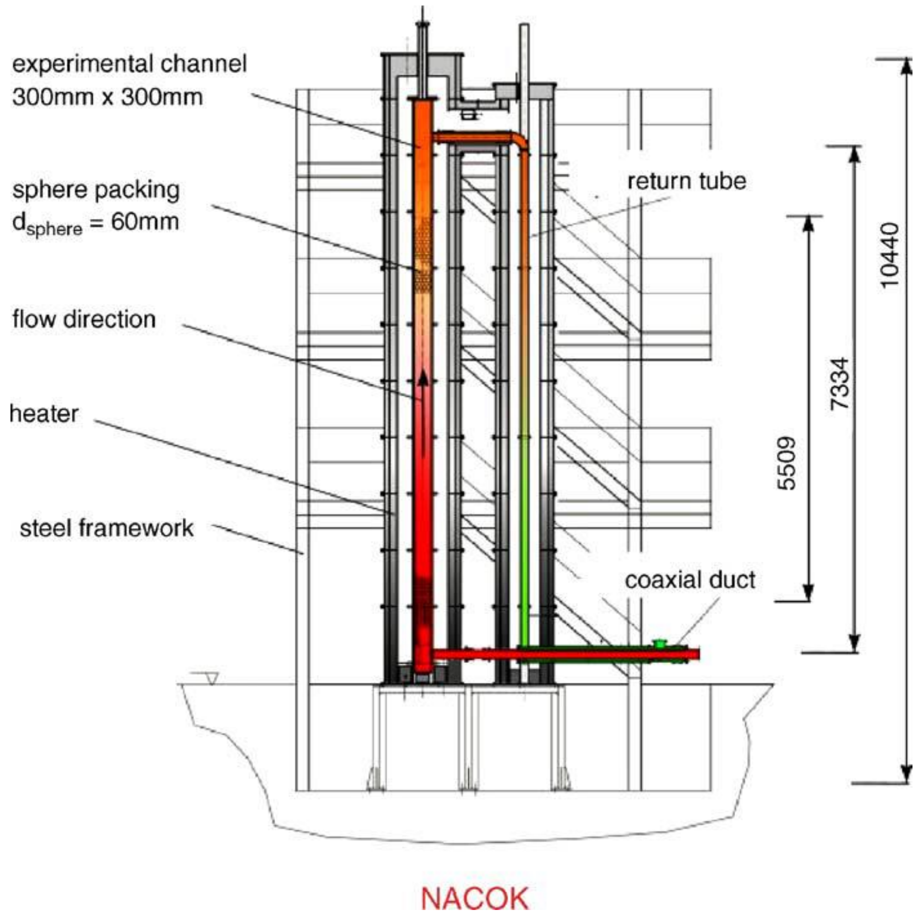

Figure 5. Physical layout of the NACOK experimental facility.

Table 3. Operational characteristics for the NACOK experiment.

Process Parameter	*Magnitude*
Max. Channel Temp.	1200C
Max Return Tube Temp	600C
Max Air Flow Rate	17 g/s
Number of Thermal Measurement Locations	82
Number of Gas Analysis Measurement Points	26

Gas Velocity Measurement Points	2
Max Thermal Power	147 kW
Active Height	7.334 m
Channel Cross Section	300 x 300 mm

As an experimental facility, it is usually quite helpful to examine experimental objectives when possible to inform comparative analyses between efforts. According Schaaf et al [18], the experimental program sought to investigate the following questions:

i. What is the buoyancy-driven air mass flow in relation to different relevant parameters, such as core temperatures, return duct temperatures, etc.?

ii. What is the delay time between the end of the heat-up period and the onset of natural convection?

iii. Which locally and time dependent processes of corrosion on formation of reaction gases (CO, CO_2) are caused by the air flow, to what extent do corrosion and gas flow influence each other, e.g. through local temperature increase due to exothermic reactions?

iv. Verification of the computer codes, which are used for accident calculations.

These are very broad goals; though early emphasis was placed on the “aerodynamic questions,” nominally the first two posed above. However, it is the emphasis on free convection onset that interests this work, as the core configuration was a “pebble bed” type, featuring a void fraction of 0.395. Of potential interest, that same void fraction applies to random packing, though the experimental model selected a regular arrangement.

Results came from two series of tests, in which the experimental channel was heated a homogenous temperature, and the return channel was maintained at an equally homogenous temperature. Table 3 presents the experimental conditions for each series.

Table 4. Experimental conditions used in the NACOK facility.

Return Channel Temp=200C		*Return Channel Temp=400C*	
Experimental Channel Temperatures (C)		*Experimental Channel Temperatures (C)*	
250	650	450	850
300	700	500	900
350	750	550	950
400	800	600	1000
450	850	650	
500	900	700	
550	950	750	
600	1000	800	

This active control of the experimental and return channel temperature speaks to a very similar experimental procedure to that of Hishida and Takeda previously. Results from this series present the free convective mass flow rate against the imposed driving temperature difference, shown in Figure 6. The report notes that thermal gradients were informed via computational analysis, as radiative transport from the experimental channel biased thermocouple output in the horizontal connection pipe length. Of greatest note is the strong effect exhibited by return tube temperature, while the mean driving temperature plays a much weaker role.

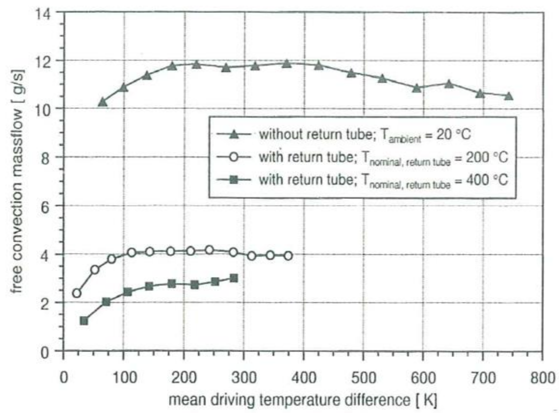

Figure 6. Measured air mass flow rate in the NACOK facility as a function of driving temperature difference.

Further, the effort reports a delay time of 5.6 hours, along with a high degree of reproducibility; however, calculated predictions of onset times were on the order of 14-39 hours [19]. This lack of agreement is attributed to leaks in the pressure boundary, providing the following as evidence to support the assertion:

Table 5. Influence of hole size at the top of the U-tube in determining onset of natural convection.

Hole Size – OD	*ONC Time (minutes)*
Control Case	205
1 mm	98
1.6	17

While the work goes on to say that welding the vessels would have achieved a "perfect tightness", it cites disadvantages during experimentation as a basis for doing so. This informs the need for comparison across platforms via mass loss analysis, which is executed as part of SFSETF shakedown testing.

If one assumes operational temperature and pressure given as 2 atm, 300C, consider the Bernoulli-predicted mass leakage rate presented in Equation 2.3.

$$P_g = P_{atm} + \frac{1}{2}\rho v_{out}^2 \tag{2.1}$$

$$v_{out} = \sqrt{2 \times \frac{\Delta P}{\rho}} = \sqrt{2 \times \frac{101.325\ kPa}{0.0802\,\frac{kg}{m^3}}} = 1589.4\ m/s \tag{2.2}$$

$$\dot{m}_{leak} = \rho v_{out} A = 0.08022\,\frac{kg}{m^3} \times 1589.4\,\frac{m}{s} \times \left[\pi \times \frac{(1.0\ mm)^2}{4}\right] \tag{2.3}$$
$$= 1E-7\,\frac{kg}{s} = 8.64\,\frac{g}{day}$$

This mass leakage rate is several orders of magnitude greater than that reported in this experimental work. The mass leakage calculations are presented in Appendix A of this document, along with equivalent diameters.

2.3.4 Influence of Previous Research on Integral Effects Test Facilities

While it is a slight temporal deviation, the following section would like to draw particular parallels between this and other pioneering research performed by Hishida and Takeda that will be discussed in the next section [3]. In particular, the adoption of phenomenological progression despite differing initial boundary conditions. This section will do this through a presentation of relevant scaling analysis as performed on the GRTS [13]. The highlights of this analysis will be presented, and should be held in mind when reading the section proceeding this one.

Early efforts of the Next Generation Nuclear Project included a scaling analysis of a gas reactor test section in order to produce data for a host of needs [20]. In order to maximize utility of the data, the hierarchical scaling analysis from above was implemented in order to quantify and preserve dominant physical phenomena. Among the transients of interest was the air ingress event, which is represented conceptually by that effort, in a subsection of the lower plenum as well as a cutaway view of the model facility, in Figure 7.

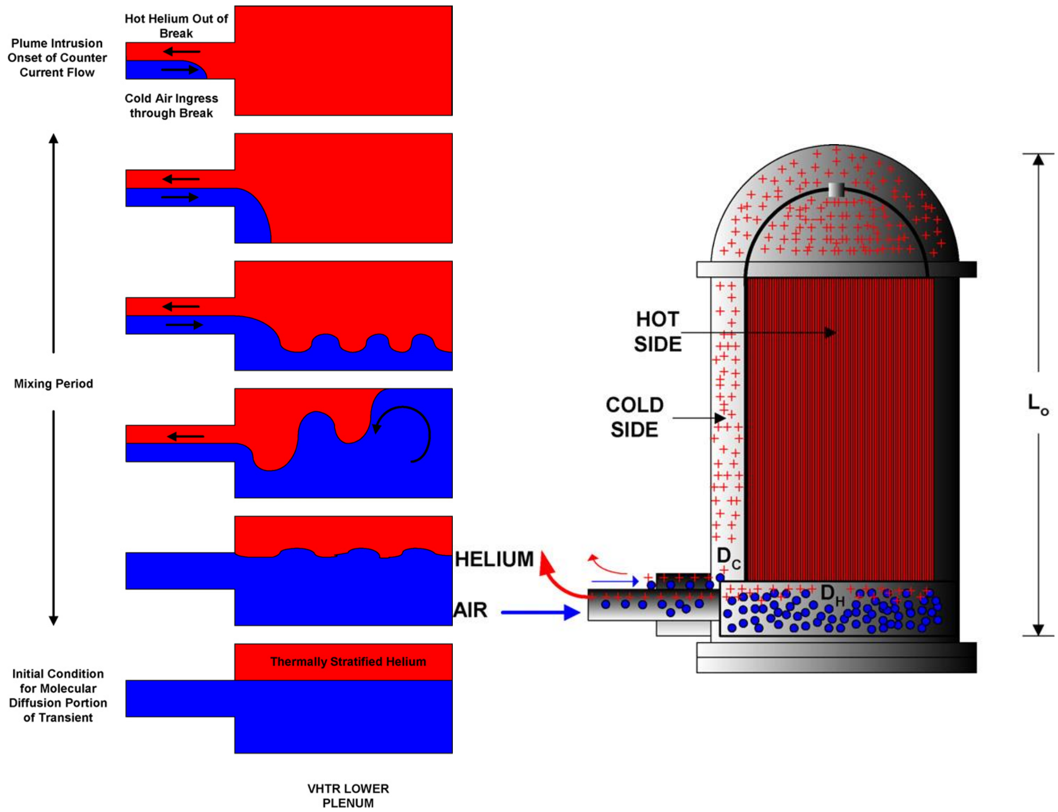

Figure 7. Representation of initial plume ingress, turbulent mixing, and quiescence, along with cutaway of the experimental facility.

The following assumptions are placed on the scaling analysis

i. Fluid flow is one dimensional along the loop axis; constant fluid properties at a cross section.

ii. Boussinesq approximation is applicable

iii. Incompressible flow (Ma <0.3)

iv. Constant cold and hot leg temperatures.

v. Constant diffusion coefficient.

vi. Molar velocity ($\boldsymbol{w}$) may be substitute in the momentum equation, as done in Hishida and Takeda's experiment [3].

These assumptions are applied to the relevant conservation equations. While Zuber provides a helpful generality, the conservation of mass and integrated momentum are presented as follows in Equation 2.4. The vertical direction occupies the z-direction in this analysis.

$$\frac{\partial \chi_{H,C}}{\partial t} + w\frac{\partial \chi_{H,C}}{\partial z} = D_{H,C}\frac{\partial^2 \chi_{H,C}}{\partial z^2} \qquad 2.4$$

$$\frac{d\dot{m}}{dt}\sum_i \frac{l_i}{a_i} = (\rho_H - \rho_C)gH - \frac{\dot{m}^2}{\rho a_B^2}\sum_i \frac{1}{2}\left(\frac{fl}{d_h} + K\right)_i \left(\frac{a_B}{a_i}\right)^2 \qquad 2.5$$

Non-dimensional parameters are selected at initial conditions, and the appropriate scaling groups are collected. There are several, and they describe a wide variety of parameters. However, in lieu of examining each, this work would like to draw focus to one particular initial condition selected by this work, shown in Equation 2.6. The convective term from Equation 2.4 is neglected, citing the low diffusive velocities.

$$\frac{\partial \chi_A}{\partial t} = D_A\frac{\partial^2 \chi_A}{\partial z^2} \qquad 2.6$$

$$\chi_A(0 \le z \le L, t = 0) = 0 \qquad \chi_A(z = 0, t > 0) = \chi_S \qquad \chi_A(z \to \infty, t > 0) = 0$$

Given the conditions of isothermal diffusion between two semi-infinite reservoirs, the analysis presents the following equation of the time rate of change of mole fraction as the primary means of air transport through the test section.

$$\chi_A(z,t) = \chi_s\left[1 - \mathrm{erf}\left(\frac{z}{2\sqrt{D_{AB}t}}\right)\right] \qquad 2.7$$

The diffusion coefficients may be calculated using the appropriate kinetic theory [21]. Using this equation the conclusion finds that air ingress via molecular diffusion may be represented as the following dimensionless equation and scaling group, shown in Equation 2.8.

$$\chi_A^* = 1 - \mathrm{erf}\left(\frac{\Pi_D}{2}\right) \qquad 2.8$$

$$\Pi_D = \frac{z}{\sqrt{D_{AB}t}} \qquad 2.9$$

This may be substituted into the initial conditions, as done in the Zuber example, to yield the expressions shown Equation 2.10.

$$\frac{\chi_{A,0}}{\tau}\frac{\partial \chi_A^*}{\partial t^*} = \frac{D_A \chi_{A,0}}{L^2}\frac{\partial^2 \chi_A^*}{\partial z^{*2}} \qquad 2.10$$

$$\tau = \frac{L^2}{D_{AB}} \qquad 2.11$$

Therefore a 1:4 scale facility expects an accelerated molecular diffusion by a factor of $16=4^2$, provided similarity of the diffusion coefficient is maintained. The current work, again, would like to point out that the initiating boundary conditions between the facilities are fundamentally different, and that may preclude application of the GRTS's analytical assumptions.

2.3.5 Definition and Role of Separate Effects Test Facilities

The NACOK and HTTF represent milestone integral effects test facilities; however, more focused experimental efforts have implemented separate effects test facilities in order to examine thermal hydraulic phenomena without the additional complexities that such integral effects test facilities introduce. Consider, for a brief moment, the length scale of the previous facilities – several meters each. The following section will examine previous efforts that have implemented a separate effects test facility format, as the similarities and differences between this effort and smaller facilities may be more illustrative of the context for this particular effort. Without further delay, please consider the definition of a separate effects test facility, as defined in this work.

Separate effects test facilities are defined as an experimental facility for which the primary interrogative focus is on the interactions on a limited number of parameters and processes, usually only one or two.

2.3.6 Inverted U-Bend Coolant Channels

The inverted u-bend channel is the prototypical experimental configuration found to interrogate a unit HTGR coolant channel, and the onset of free convection therein. The work of Hishida and Takeda is particularly prominent in this area; it may arguably be said to be the pioneering effort. The experimental apparatus used is shown schematically in Figure 8, and the reference facility, the JAERI High Temperature Test Reactor (HTTR) [22], is shown in Figure 9.

Therefore, this section will provide a comprehensive summary of their initial effort on the study of air ingress, as well as other successive efforts. This summary will call into greater focus and clarity certain experimental and analytical choices that still influence the HTGR experimental community at the time of writing

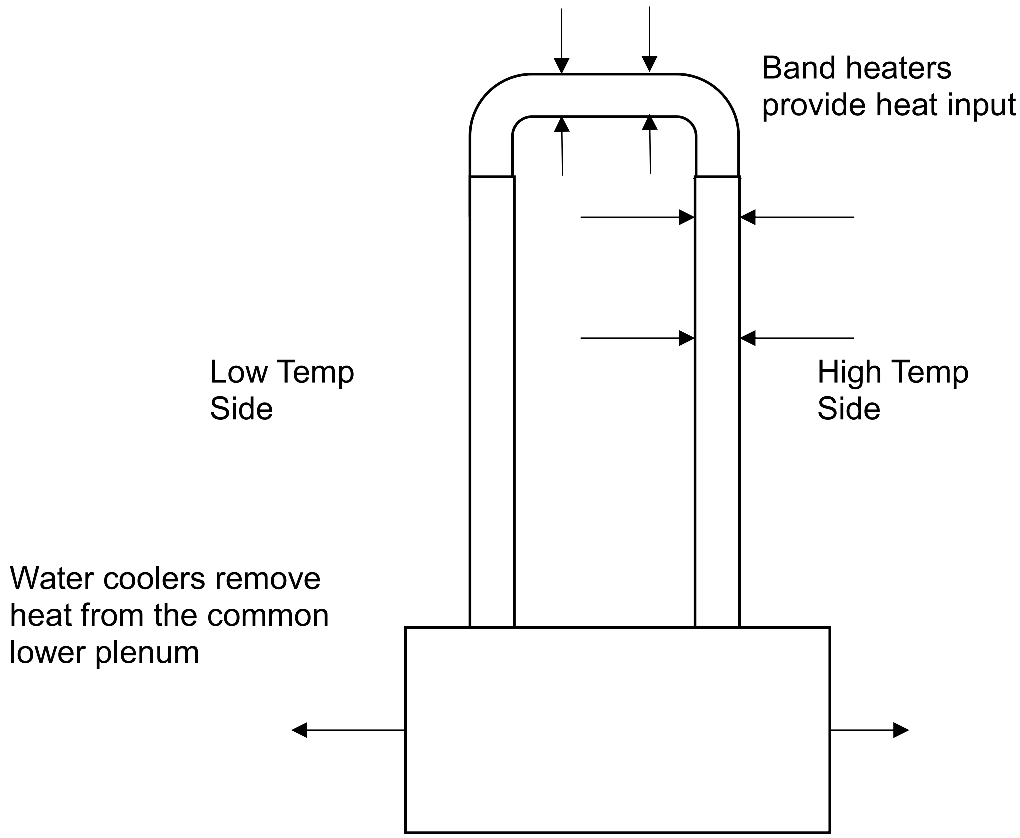

Figure 8. Experimental apparatus used by Hishida and Takeda.

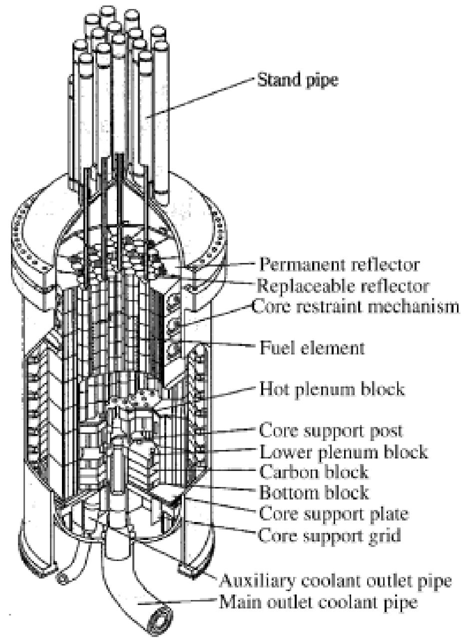

Figure 9. Cut away view of the reactor core structure of the JAERI HTTR.

The experimental apparatus is constructed of stainless steel, both the inverted bend and the tank. One vertical pipe is heated via electrical power, and the other pipe is water-cooled – simulating the function of the RCCS. The inner diameter of the tube is 52.7 mm (2.07 in.).The horizontal bend connecting the two sides is also heated. In addition, it features the following instrumentation locations:

i. Mole fraction is measured via 13 suction taps leading to sound velocity measuring chamber. Inventory return is in the vicinity of suction in order to minimize flow distortion.

ii. Temperature is measured via 17 K-type thermocouples.

As a pioneering effort, this experimental configuration set the stage for later efforts, such as those of Gould et al. It was also from this effort that the emphasis on molecular diffusion becomes established. Early in their analysis, Hishida and Takeda noted that the combination of molecular diffusion, driven by chemical gradients, as well as one-dimensional free convection, driven by thermal gradients, will determine transient behavior. This is reflected in the experimental results, which compare the mole fractions at various heights under varying experimental conditions.

For the sake of clarity, the researchers used the sudden increase in nitrogen mole fraction as the onset time for global free convection. This work would also like to examine the fundamental assumptions posed in Hishida and Takeda's work, as those assumptions have and do influence the physical understanding of the dominant phenomena.

Numerical analysis of gas transport in a reverse U-shaped tube

In order to establish initial estimates, and quantify deviations from the idealized behavior, a numerical analysis was performed, initiating with the following, and other, assumptions:

i. One dimensional piston flow in the tube (sharp diffusion boundary);

ii. Diffusion coefficient is independent of gas concentration;

iii. The molar average velocity, $\boldsymbol{w}^*$, can be used in the momentum conservation equation;

iv. Gas temperature, molar density, diffusion coefficient, and friction factor are uniform at each region, and constant with respect to time.

These assumptions, paired with the instrumentation model shown in Figure 10, permit the researchers to "step through" the facility and solve the relevant transport equations over the interrogated region.

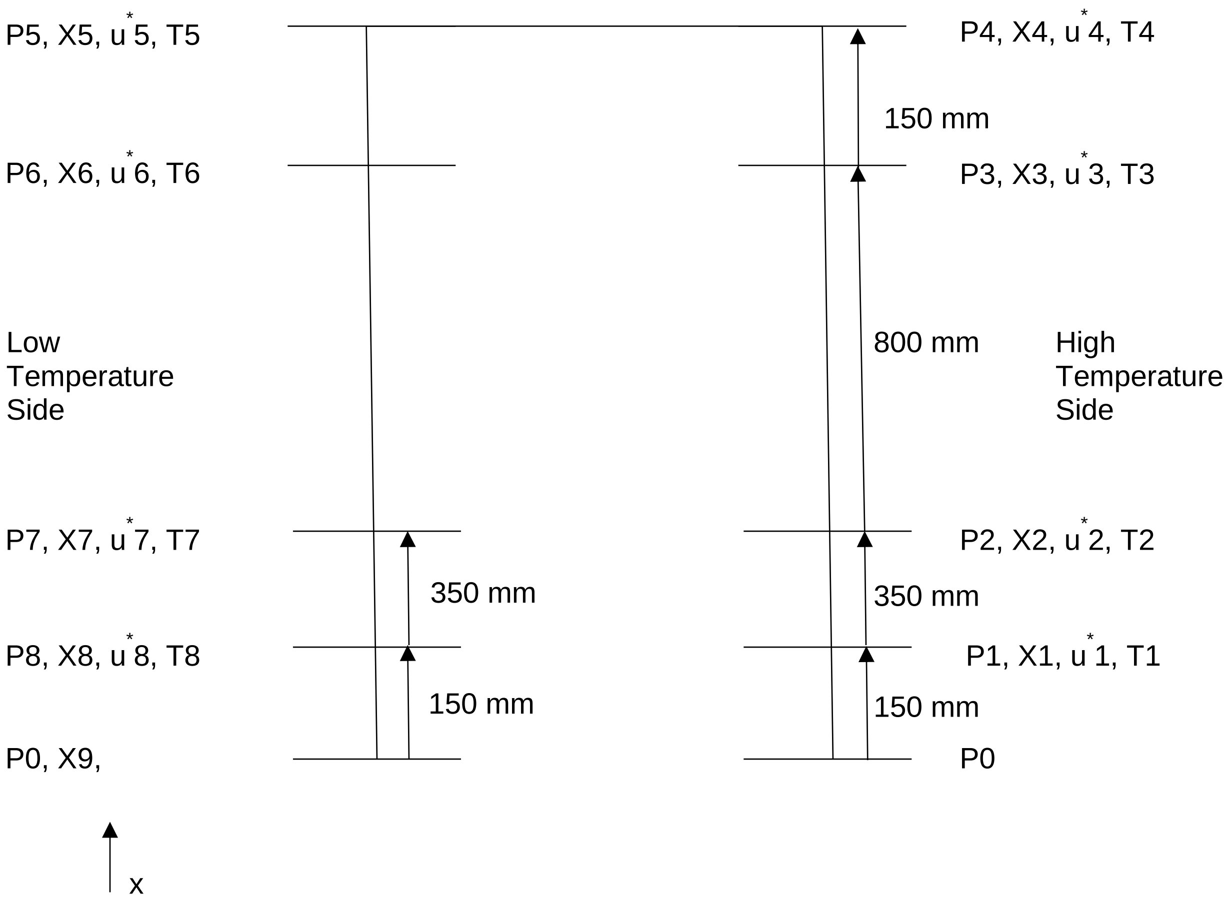

Figure 10. Instrumentation model of experimental facility used by Hishida and Takeda.

Paired with an implicit temporal method, the following discretization of the momentum conservation equations was implemented, as shown in Equations 2.12-15.

$$\rho\frac{\partial U^*}{\partial t} = -\frac{\partial P}{\partial x} \pm \rho g + \frac{1}{2}\rho U^*|U^*|\left(\frac{f}{D_e} + K\right) \qquad 2.12$$

$$\frac{\partial U^*}{\partial t}\int \rho dx = -\int dP \pm g\int \rho dx + \frac{1}{2}\rho U^*|U^*|\left(\frac{f}{D_e}\int \rho dx + \sum_i \rho_i K_i\right) \qquad 2.13$$

$$\rho = C[\chi_A M_A + (1-\chi_A)M_B] \qquad 2.14$$

$$C = \frac{P}{RT} \qquad 2.15$$

The following initial conditions are provided:

$$0 \le x \le x_1 \qquad P = P_0 - g\int_0^x \rho\, dx \;;\chi_a = 1 \qquad T = T_1 \qquad U^* = 0$$

$$x_1 \le x \le x_4 \qquad P = P_0 - g\int_0^x \rho\, dx \;;\chi_a = 0 \qquad T = T_2 \sim T_4 \qquad U^* = 0$$

$$x_4 \le x \le x_5 \qquad P = P_0 - g\int_0^{x_4} \rho\, dx \;;\chi_a = 0 \qquad T = T_5 \qquad U^* = 0$$

$$x_5 \le x \le x_8 \qquad P = P_0 - g\int_0^{x_4} \rho\, dx + g\int_{x_5}^{x} \rho\, dx \;;\chi_a = 0 \qquad T = T_6 \sim T_8 \qquad U^* = 0$$

$$x_8 \le x \le x_9 \qquad P = P_0 + g\int_{x_9}^x \rho\, dx \;;\chi_a = 1 \qquad T = T_9 \qquad U^* = 0$$

Constant value and constant slope conditions are provided where appropriate at the region boundaries. However, the net result of this scheme is reducing the differential conservation of linear momentum equation into the following ordinary differential equation.

$$A_i \frac{dU_i^*}{dt} = -\delta P_i \mp g\bar{\rho}_i - \xi U_i^* \,|U_I^*| \qquad 2.16$$

$$\delta P_i = \int_i dP \qquad \bar{\rho}_i = \int_i \rho\, dx \qquad \xi_i = \frac{1}{2}\left(\frac{f}{D_e}\int_i \rho\, dx + \sum_l \rho_l k_l\right)$$

Substitution of these, and assumptions regarding fluidic profiles in a section, and this is exactly the integrated loop momentum balance equation implemented by Reyes et al. in the scaling analysis of the Gas Reactor Test Section (GRTS) [13].

Small molar velocities, along with constant fluid temperatures and properties over a region, made this numerical scheme possible when the difference equation is solved via the Gauss-Jordan method. However, the configuration and layout of this facility is critically important to note from the perspective of fluidic communication paths of heat and mass transfer:

i. Heat transfer will be dominated by conduction from the band heaters.

ii. Mass transfer will be dominated by mass flux through the cold temperature side inlet (nominally). While the authors note the importance of convective forces, in addition to molecular diffusion, this facility a priori forces an initial molar velocity that may or may not be characteristic of prototypical facility conditions.

Comparing the facility and schematic, one may see the similarity with respect to fluid ingress: Air must enter the core structure vertically through a penetration - the core support grid in the HTTR, the common plenum in the test apparatus. This provides a physically-defensible basis for the assumptions noted previously: ingressing velocities must necessarily be low as Brownian motion is responsible for fluid ingress.

Moreover, one may impose a zero net mass flux across the boundary at the initiation of the experiment – requiring the same mass transfer out as in. While that may be significant for the helium inventory (recall the lower density afforded it due to its elevated temperature), for the significantly more dense air, that velocity is significantly smaller. All that to say that this: assumption of diffusive ingress should be carefully applied, as its physical basis is directly coupled to the facility geometry.

However, one should also consider the results reported. The degree of temporal agreement between the analytical and experimental results is quite remarkable. Figure 11 presents the mole fraction of nitrogen at various locations for the isothermal test case. Note the deviation in Figure 12 in particular. Of considerable interest is the imposition of a seemingly arbitrarily chosen molar velocity, which then forces agreement at sampling locations 3 and 11 (the same height), but in opposing directions. Note that initial calculations under-predicted molar fraction at position 3, while over-predicting at position 11 when initial velocities are null values. However, a forcing function forces agreement in both directions.

This supports the idea that convective activity within HTGR facilities is constant, even under idealized conditions, and play a significant role in facility behavior under all but isothermal conditions.

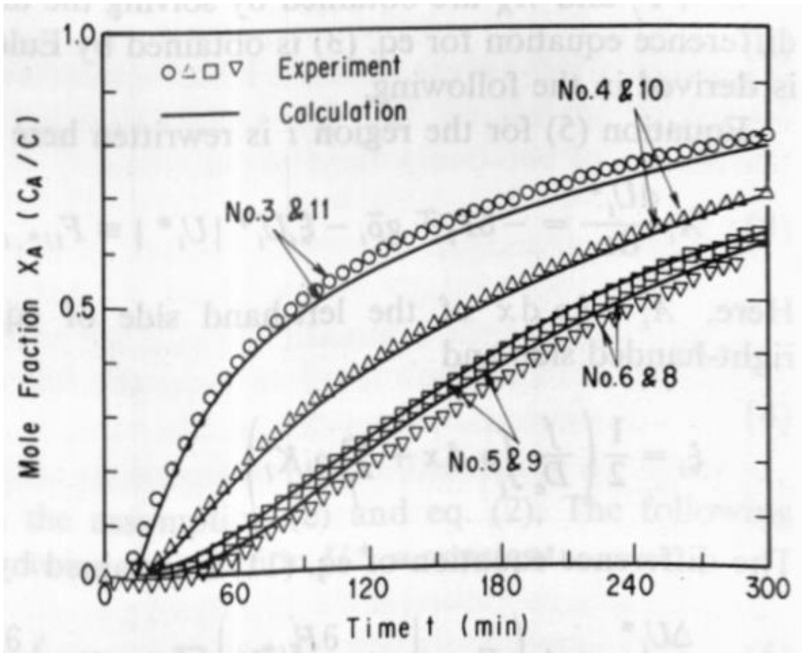

Figure 11. Mole fraction of nitrogen in the u-bend test loop during isothermal experimental conditions. Test number pairs occur at the same height, but opposite legs.

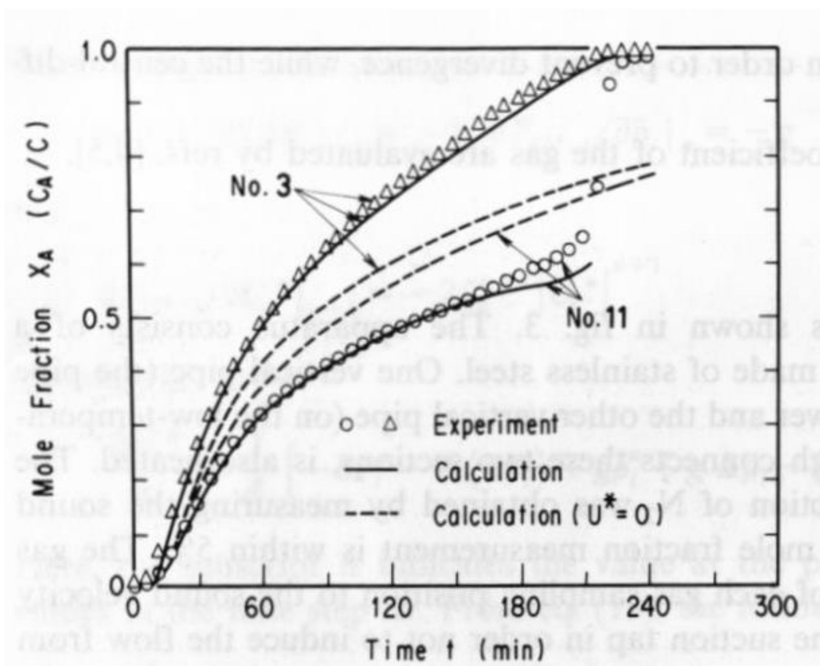

Figure 12. Mole fraction of nitrogen gas under non-isothermal conditions. Note the difference in 3 and 11 position molar concentrations.

As an early adoption of the scaling methodology, a larger test section was constructed as a more representative facsimile of the HTTR facility, as shown in Figure 13. Again, note the inlet/outlet orientation along the vertical.

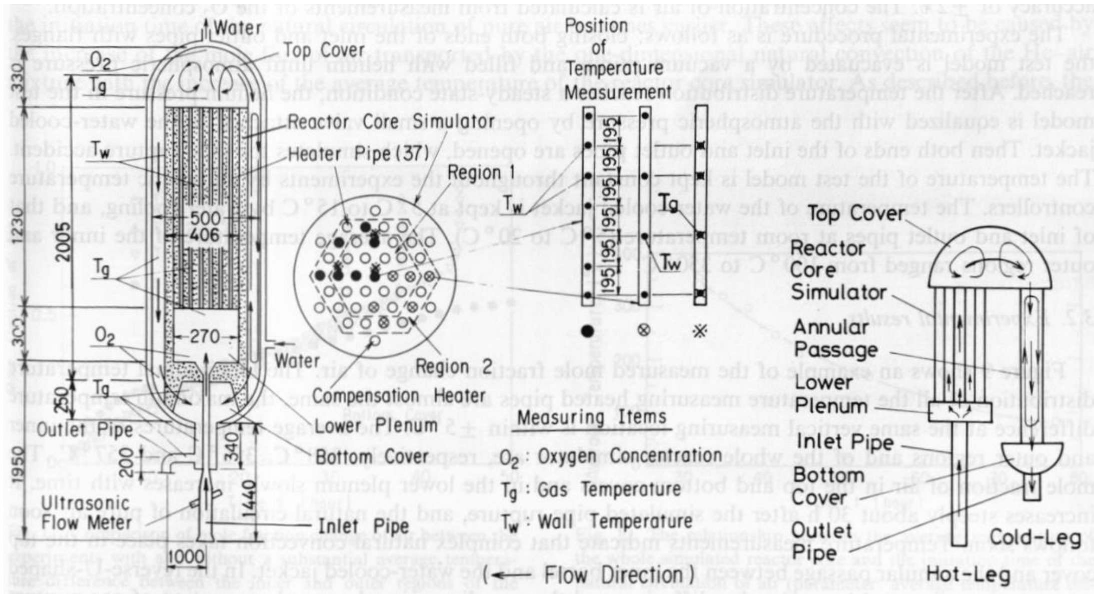

Figure 13. Experimental apparatus of the HTTR vessel, and schematic drawings demonstrating flow paths.

The following paragraph describes the experimental procedure implemented to produce. Closing both ends of the apparatus, a vacuum is applied (pressure limits not reported) and helium backfilled to atmospheric pressure. Heat is applied until temperature distribution has achieved a steady state distribution, and heat rejection capacity is provided via water-cooled jackets. Then both inlet and outlet pipes are opened simultaneously, and profiles are maintained via active heat rejection.

Figure 14 shows the mole fraction of air at an unnamed location. Note the sharp rise at approximately 30 hours, which is used a diagnosis of the onset of natural convection. The authors note a correlation to inner and outer region temperature difference and ONC time, and present the curve shown in Figure 15.

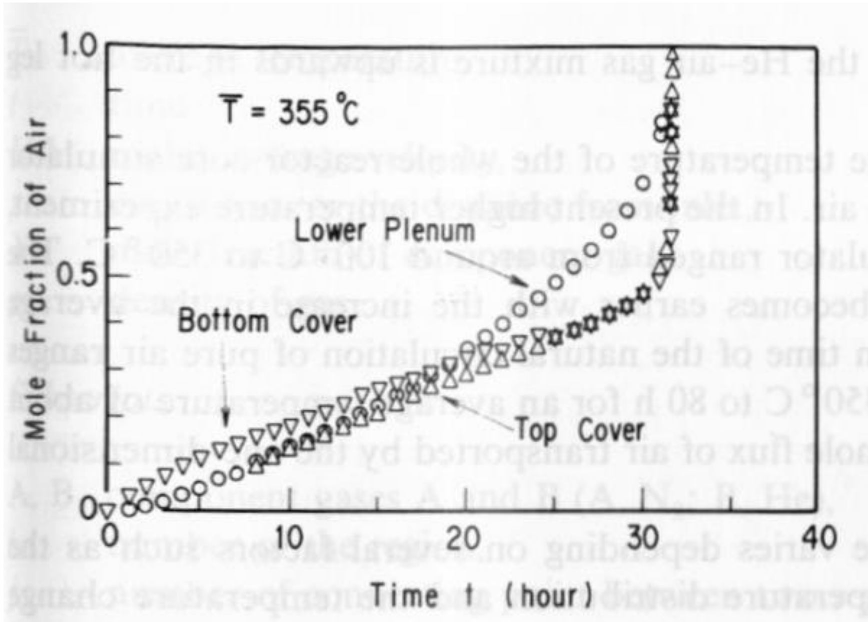

Figure 14. Mole fraction of air as a function of time at various locations.

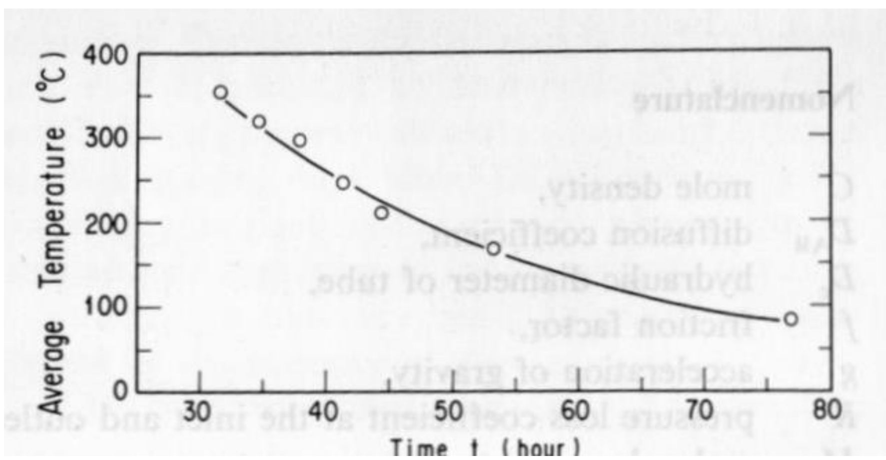

Figure 15. Correlation of ONC time to average temperature difference between the core and the onset time of natural convection.

As a concluding remark, the discussion accounts for this temperature dependence on the increased mole flux of nitrogen transported by one-dimensional natural convection of the mixture. This is a particularly curious note, as it indicates the onset time is strongly dependent on convective currents within the core region. But it is on the basis of these results that ONC times of 30 – 80 hours are reported, and the basic phenomenological progression becomes established as:

i. Initiation by molecular diffusion,

ii. Stratified vertical flow,

iii. Onset of global natural convection, as indicated by influx of air (or simulant fluid).

At the risk of belaboring the point, this work would like to append the following considerations, as they influence work that follows this particular experiment:

iv. The onset time phenomenology is directly coupled to the geometry of the initial conditions: Vertical orientation of the mass flux boundaries forces a diffusive bias under steady conditions.

v. Diffusion may limit initial ingress, but convective currents quickly dominate the transient. Access to those convective currents is the dominant barrier to oxygen transport throughout the core region.

2.3.7 Chang Oh et al.

Chang Oh, among several others, have made significant contributions to this area. Several works will be highlighted as they pertain to this experimental effort; however, begin with a theoretical treatment of the accident progression [5], which is the first of a two-part series. The second part is a computational treatment using FLUENT [23].

Oh presents several stages of air ingress, as shown in Figure 16. In particular, Oh et al. assert that, following depressurization and blow down, counter current stratified flow (lock exchange flow) initiates to drive air into the reactor vessel, but that this particular phenomenon is driven thermal gradients across the core region. This is labeled as density driven air ingress (DDAI).

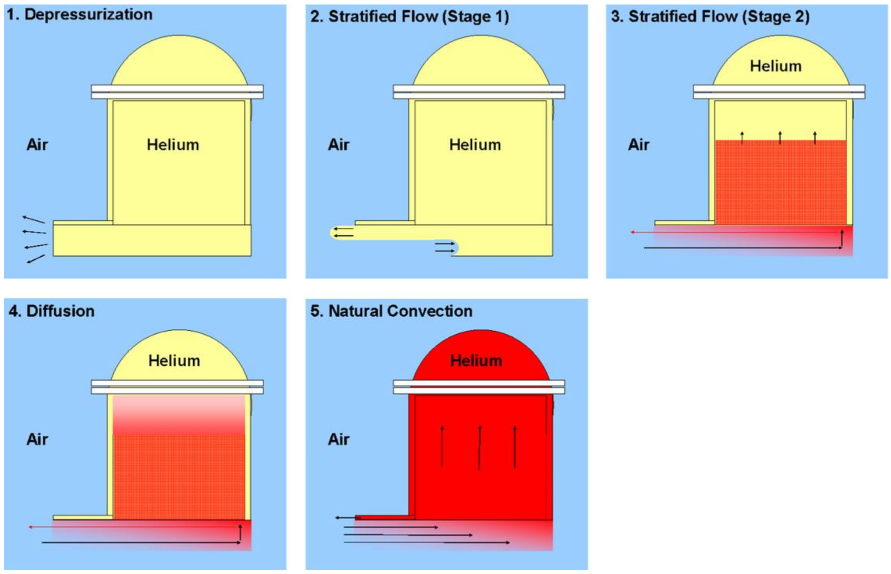

Figure 16. Phenomenological overview of the air ingress accident.

Additionally, it is asserted that an energetic resistance may lay on the system prior to free convection onset. In particular, Oh goes on to claim that the helium acts as a momentum sink, a resistance to be overcome. Oh provides the consideration that the ingressing fluid may carry sufficient kinetic energy to overcome that resistance. Consider the kinetic energy of the fluid, represented in Equation 2.17.

$$\boldsymbol{KE_{Working\ fluid}} = \frac{\boldsymbol{\rho g H}}{\boldsymbol{8}}\left(\frac{\boldsymbol{1-\gamma}}{\boldsymbol{\gamma^3}}\right) \qquad 2.17$$

$\boldsymbol{\gamma}$ is defined as the fluidic density ratio, assumed evaluated at initial conditions. Equating it to the hydrostatic head of the fluid column yields the stratification resistance shown in Equation 2.18.

$$\boldsymbol{R_{strat}} = \boldsymbol{\rho_{PPV} g H_{PPV}} \qquad 2.18$$

This concludes with a comparison of vessel to duct heights in order to establish a critical height ratio $\left(\frac{\boldsymbol{H}}{\boldsymbol{H_V}}\right)_{\boldsymbol{min}}$, such that, according to the 600 MW_{th} GT-MHR design criteria,

$$\left(\frac{\boldsymbol{H}}{\boldsymbol{H_v}}\right)_{\boldsymbol{min}} = \frac{\boldsymbol{8\rho_{PPV}}}{\boldsymbol{\rho}}\left(\frac{\boldsymbol{\gamma^3}}{\boldsymbol{1-\gamma}}\right) = \boldsymbol{0.02494} \qquad 2.19$$

While this a particularly interesting analysis, it does require the assumption that thermal energy will play no role in the dissipation of the stratification layers – a concerning assertion given that the thermal energy resident in the system (at >800C, mind) should be several orders of magnitude greater than the kinetic energy of the ingressing fluid. However, it is the implicit assertion that helium will provide an amount of flow resistance to the onset of global free convection that is of prime interest to this work, as it speaks to a greater bias within the community to assume diffusion as the active mode of air transport.

The motivation for this analysis is the comparison of convective and diffusive time constants, Oh asserting that convection has a much larger contribution, by a factor of approximately 660 [5].

Explicitly, it was shown that, for diffusion, the governing time scale is given by $\boldsymbol{t_d = 1.29 \times 10^4 s}$, calculated using the analysis perform by Reyes et al [13] regarding diffusive transport. This should be compared to the convective time scale for density driven lock exchange flow, $\boldsymbol{t_{le} = 19.5\ s}$.

A brief note on this convective scale: It was calculated as shown in Equation 2.20. The salient fact to note is that the reference velocity selected is the superficial velocity of the ingressing air. That is, the convective time scale for air ingress horizontally into the core is compared to the diffusive time scale upwards through the core region. And it is on this basis that the kinetic argument mentioned above is made. Also, the length selected is the assumed duct length remaining to access the lower plenum after the assumed coaxial duct rupture.

To compare, an integration of the lower plenum concentration over its height is proposed as the method of determination regarding the diffusive time scale. The point of 50% molar fraction of air is the appropriate termination point for this stage of the transient.

$$\boldsymbol{U_s = \frac{U_h}{H} = 0.21\ m/s} \tag{2.20}$$

$$\boldsymbol{\tau_{con} = \frac{L_1}{U_s} = \frac{3.4\ m}{0.21 \frac{m}{s}} = 19.5\ s} \tag{2.21}$$

$$\tau_{diff} \rightarrow \chi^*(z,t) = \frac{C_{air}(z,t) - C_{air,0}}{C_{air,s} - C_{air,0}} \tag{2.22}$$

$$= \frac{1}{D_{LP}} \int_{lower\ plenum} 1 - \mathrm{erf}\left(\frac{z}{s\sqrt{D_{AB}t}}\right) dz = 0.5$$

$$\tau_{diff} = t = 1.29 \times 10^4 s \tag{2.23}$$

Comparing the magnitude of these time scales, Oh asserts that the first stage of the transient is dominated by convective (stratified flow). It is sufficient to say the assertion that convective motion may dominate is a credible one; however, it is highly suspicious that this calculation provides direct support of that claim. Regardless, this assertion is captured and presented here for the following reason:

It points to a lack of consensus within the community regarding onset mechanisms.

While the theoretical treatment does little to alter the phenomenological understanding of the transient, it does assert the potential role of mixed physics, and seeks to quantify them in order to demonstrate advective forces may be of an order approximately of or much greater than diffusive forces.

This is presented as the motivation for the computational fluid dynamics study presented in the second publication [23]. Following Liuo [4], the work asserts a stratified lock exchange flow, while noting the complex geometry present within the lower plenum of the prototype facility, as shown in Figure 17.

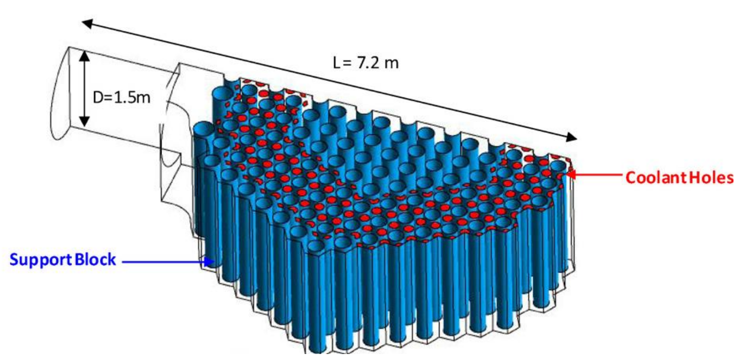

Figure 17. Three dimensional facility render of the lower plenum used in the CFD study.

However, Oh notes the difficulty in determining the initiation point for the study, especially given the computational effort required for converged solutions as the facility depressurizes from 7

MPa. Other computational efforts have noted similar challenges [24], and in similar cases, the initial blowdown is neglected on the basis that the duration is insufficiently long to warrant the, rightfully estimated, tremendous computational resources such simulation would require. While neatly averting that particular problem, this design choice also neatly circumvents the consideration of helium inventory retention within containment.

This work will neglect the mesh studies performed in this work, as they are not germane to this particular work. Rather, consider the initial conditions imposed on this simulation effort, as presented in Figure 18. Note the magnitude and gradation within the core region, taken from previous computational effort done by Oh et al. [25] with the GAMMA software package.

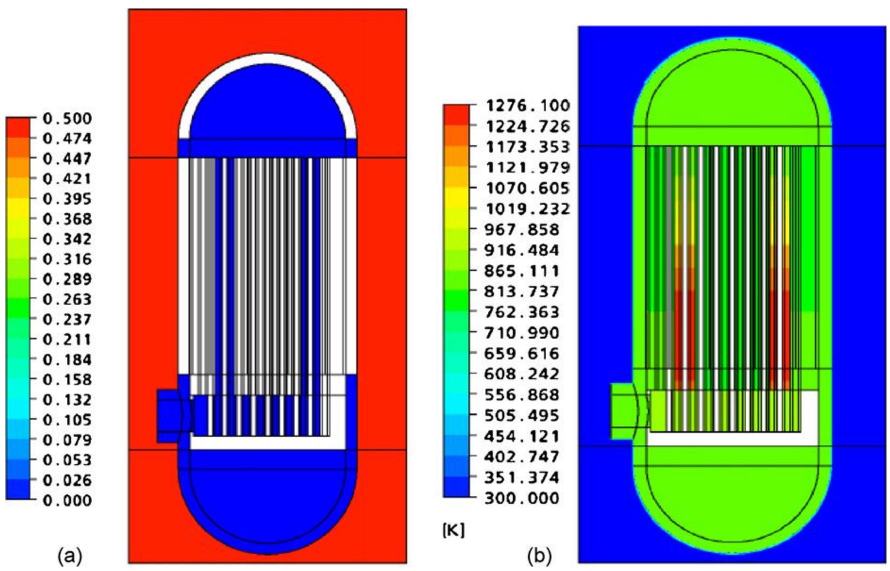

Figure 18. Contour plots showing the initial mole fraction and temperature contours of the 600 MW(th) GT-MHR.

The importance of this set of initial conditions is significant, as it represents realistic facility conditions, at least with respect to temperature gradients. Figure 19 presents an isometric view, and provides average vessel temperatures to illustrate radiative heat transport from the reactor vessel.

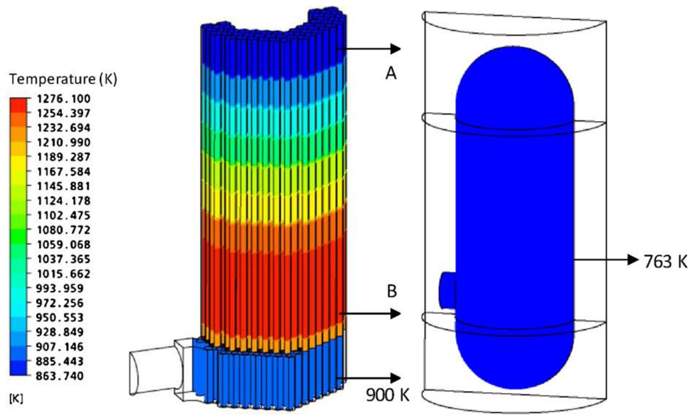

Figure 19. Wall temperature contour plot, and reactor vessel temperature contour plot.

Imposing a constant wall temperature boundary condition, along with a porous flow model, the following mole fraction contour plots were generated as the simulation progressed. Note the time stamp, as well as initial ingress mechanics.

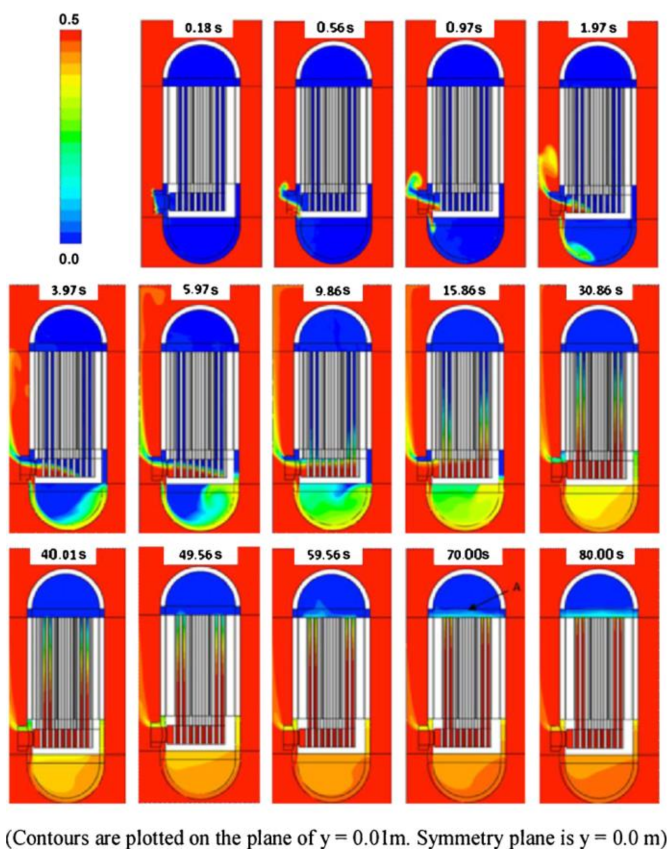

Figure 20. Mole fraction contour plots generated with ANSYS FLUENT based on GT-MHR reference design.

These results are intensely interesting, as they seem to suggest that ingress mechanics may significantly accelerate onset of free convection in a matter of seconds, rather than on the order of several hours as predicted by the NACOK experiment. The study goes on to suggest certain mitigation strategies, but the conclusion is most telling. The following sentence, quoting Oh et al, elaborates on the evidence presented that air may actively ingress into the lower plenum due to momentum generated during lock exchange flow.

This is because heat transfer from the solid structures inside the reactor vessel sufficiently overcome the hydraulic resistance when air passes the lower plenum and core blocks.

Heat transfer may provide sufficient momentum to overcome the hydraulic resistance presented by the core structures, but apparently does not contribute to overcoming the hydraulic head of the helium [5]. This work will comment no further on the models utilized by Oh, other than to provide the settings used in the FLUENT model in Table 6.

Rather, consider first a brief qualitative treatment of the ingress mechanics presented in Figure 20 above. An air front propagates immediately into the lower plenum, as well as the vessel bottom. While densimetric gradients is one way of describing this ingress, this work would like to suggest the following root cause: Fluid displacement driven by a gravitational potential energy difference. At the risk of being pedantic, the increased clarity is of value to later sections of this work. Moreover, it emphasizes the displacement is not driven by external gradients, but rather by fluidic access to displaceable fluids – that is, there is helium gas at a grade below the ingressing plume. Therefore, this fluid will be displaced prior to the establishment of quiescence.

That is apparently of primary importance, as fluid immediately ascends via the coolant channels. Assuming that there is limited transfer of linear momentum to the vertical, and that vertical velocity becomes non-zero at approximately 9 seconds, then the effective fluid velocity is presented in Equation 2.24,

$$\boldsymbol{v_{eff}} = \frac{\mathbf{10.82}\boldsymbol{m}}{\mathbf{71}\ \boldsymbol{s}} = \mathbf{0.15}\ \boldsymbol{m/s} \qquad 2.24$$

This is on the order of the imposed $\boldsymbol{U^{*}} = \mathbf{0.2}\ \boldsymbol{m/s}$, utilized by Hishida and Takeda to force the agreement shown in Figure 12 above.

Table 6. FLUENT model settings used in CFD simulation of the GT-MHR by Oh et al.

Parameters	*Settings*
Code version	FLUENT 6.3.26
Solver type	Pressure based solver
Time scheme	Implicit
Dimensionality	3D
Steady/Unsteady	Steady
No. of CPUs	20
Velocity formulation	Absolute
Gradient option	Node based
Porous formulation	Physical velocity
Viscous model	k-ϵ Realizable
Air mass fraction	0.5
Energy + species equation solve	Yes
Density	Incompressible, ideal gas
Diffusion	Multicomponent

2.3.8 1/8th Scale Ohio State Facility

Chang Oh, in conjunction with a team at Ohio State University [26], initiated design activities to construct a two vessel test facility, as shown in Figure 21. It is a 1/8th scaled facility, in comparison to the 1/4th length scale implemented in the HTTF. Initiated approximately at the same time as this effort, initial publications were both timely and exciting, as initial phenomenological discussion and motivation cast doubt on the dominance of molecular diffusion regarding air ingress mechanics, supported by citing computational efforts that show wide variability in ONC time, ranging from 80 seconds [23] to 500 hours [27].

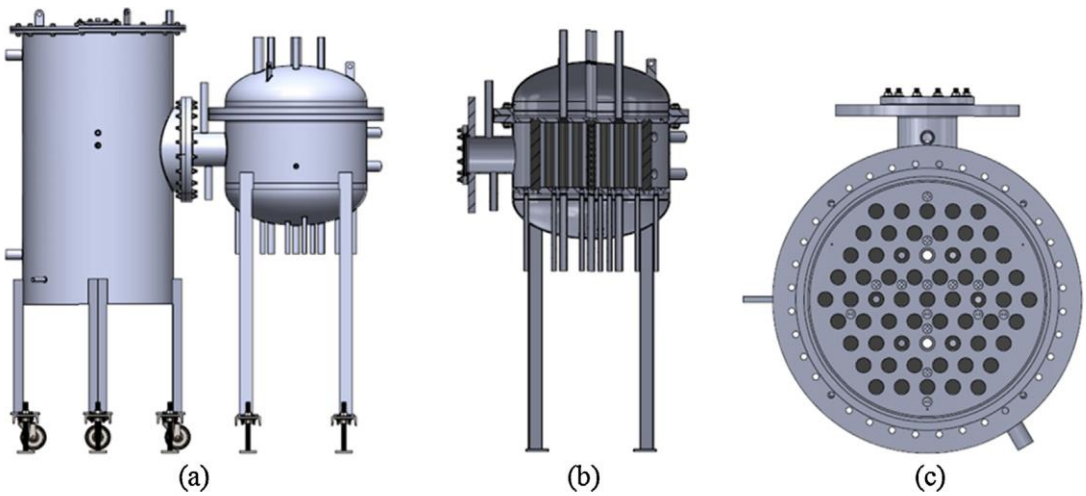

Figure 21. Experimental facility utilized by Arcilesi et al.

The key dimensions are presented in Table 7 alongside the prototypical values for comparison. Note the flanged connection joining the vessels, as well as the prismatic core configuration. No piping and instrument diagrams (P&IDs) were presented, so no information regarding pressure relief and equilibration is provided.

Table 7. Key design parameters of the 1/8th scaled facility used by Arcilesi et al.

Parameter	*Prototype (m)*	*1/8th Scale Facility (m)*
Vessel height	23.7	2.963
Vessel inner diameter	7.8	0.975
Vessel outer diameter	8.4	1.050
Core height	11	1.375
Active core height	7.8	0.975
Support column height	2.84	0.355
Cold duct outer diameter	2.29	0.286

Hot duct diameter	1.5	0.1875
Hot duct length	2.86	0.2032

To achieve these particular quantities, a similar scaling analysis to that presented by Reyes was implemented; however, there are some notable differences. Consider first the differential continuity equation presented in Equation 2.26, notably absent the diffusive term. The integrated loop momentum balance equation is also implemented.

$$\frac{\partial \rho_{H,C}}{\partial t} + w_{H,C}\frac{\partial \rho_{H,C}}{\partial z} + \rho_{H,C}\frac{\partial w_{H,C}}{\partial z} = 0 \qquad 2.25$$

$$\frac{d\dot{m}}{dt}\sum_i \frac{l_i}{a_i} = (\rho_H - \rho_C)gH - \frac{\dot{m}^2}{\rho a_B^2}\sum_i \frac{1}{2}\left(\frac{fl}{d_h} + K\right)_i \left(\frac{a_B}{a_i}\right)^2 \qquad 2.26$$

From these, the following scaling ratios are determined, as they appear in the dimensionless momentum equation, shown in Equation 2.27.

$$\frac{d\dot{m}}{dt}\sum_i \frac{l_i}{a_i} = \Pi_L\left[\frac{(\rho_C^* - \rho_H^*)H^*}{\Pi_{Fr}} - \dot{m}^{*2}\Pi_F\left(\sum_i \frac{1}{2}\left(\frac{fl}{d_h} + K\right)_i \left(\frac{a_B}{a_i}\right)^2\right)^*\right] \qquad 2.27$$

$$\Pi_L = \frac{H_0}{a_r \sum_I \frac{l_i}{a_i}} \qquad \Pi_{Fr} = \frac{\rho_r w_0^2}{(\rho_C - \rho_H)gH_0} \qquad \Pi_F = \left(\sum_i \frac{1}{2}\left(\frac{fl}{d_h} + K\right)_i \left(\frac{a_B}{a_i}\right)^2\right)_0$$

The scaling analysis terminates with a calculation of the diffusion time scale,τ_{diff}. The appropriate kinetic theory is referenced [21], and the governing equation is presented as

$$\frac{\partial \rho_a}{\partial t} = D_{air-helium}\frac{\partial^2 \rho_a}{\partial z^2}\ ; 0 < z < \infty, t > 0 \qquad 2.28$$

$$\rho_a(z, t = 0) = 0 \qquad \rho_a(z = 0, t) = \rho_{a,s} \qquad \rho_{a(z\to\infty,t)} = 0$$

That is, the comparison point is isothermal diffusion between semi-infinite reservoirs. As an evaluation method, the equation presented in Equation 2.29 is meant to represent the mass flow rate of air assuming only the influence of diffusion.

$$\dot{m} = \rho v A = 2\rho_{a,s} A_C \sqrt{\frac{D_{air-helium} t}{\pi}} \quad 2.29$$

The work presents an estimated 14,160 seconds necessary for 7.11 kg of air to diffuse into the channel, and 258 seconds for 0.014 kg of air to diffuse into the sub-scale facility. The equivalence of these times and masses is not elaborated upon further.

The analysis goes on to describe thermal profiles within the coolant channels of the facility in order to assert heat transfer similarity, going further to consider the lower plenum structure and its contributions to both flow resistance and heat transfer, although the details of that analysis are not germane to the current work.

One last note should be given to the overall time constant calculated by Arcelesi et al. [26] which is presented in Equation 2.30. The assertion is that the overall time scale of the event is a function of the time scales of each constituent stage, which density driven air ingress (DD, or DDAI) would dominate the total time scale.

$$\frac{1}{\tau_{total}} = \frac{1}{\tau_{DD}} + \frac{1}{\tau_{HPNC}} + \frac{1}{\tau_{Diff}} \quad 2.30$$

Table 8 presents the minimum time scales in the 1/8th scale facility, as well as the prototypical facility. These time scales include density driven air ingress (DDAI), hot plenum natural convection (HPNC), and molecular diffusion.

Table 8. Comparison of air-ingress phenomenon time scales.

Geometry	*DDAI (s)*	*HPNC(s)*	*Diffusion (s)*	*Total (s)*
Prototype	16.08	14,008	14,160	16.04
1/8th Scale	5.97	3299	258	5.82

Setting aside the theoretical treatment of the phenomena, this facility represents one of the primary sources of inspiration for this work, especially with regards to the selection of instrumentation. While it is clarified further in the *OSU SFSETF Instrumentation Plan* [28] it was early remarked that the operational requirements for both facilities are remarkably similar. In fact, the OSU facility provided an excellent template, as its operational environment is significantly more challenging than those of the SFSETF. Table 9 presents the number and type of instrument deployed in the 1/8th scale facility.

Table 9. Key instrumentation deployed in the 1/8th scaled facility.

Interrogated Parameter	*Instrument Typ*	*Number of measurement locations*
O_2 concentration	Oxygen Analyzer Probe	7
Pressure	Gauge Pressure Transmitter	10
Temperature	K-type TC Probe	40

Of particular interest is the oxygen analyzer probe called out in this work: Teledyne Model 9060H Oxygen Analyzer. It was assumed at the initial reading that this instrument would be used to determine the onset of natural convection, although no expected instrument response was reported.

2.3.9 Optical Methods and the Inverted H-Bend

The work of Franken et al. is also extremely timely to this research, and presents a different, and valuable, experimental approach. The influence of Hishida and Takeda on this work is clearly on display in Figure 22, which presents a schematic of the experimental setup. Note the inverted u-tube, or h-tube, according to the authors. The additional 0.5m extension above the cross over length is provided in order to simulate additional coolant volume available in the upper plenum of a prototypical facility.

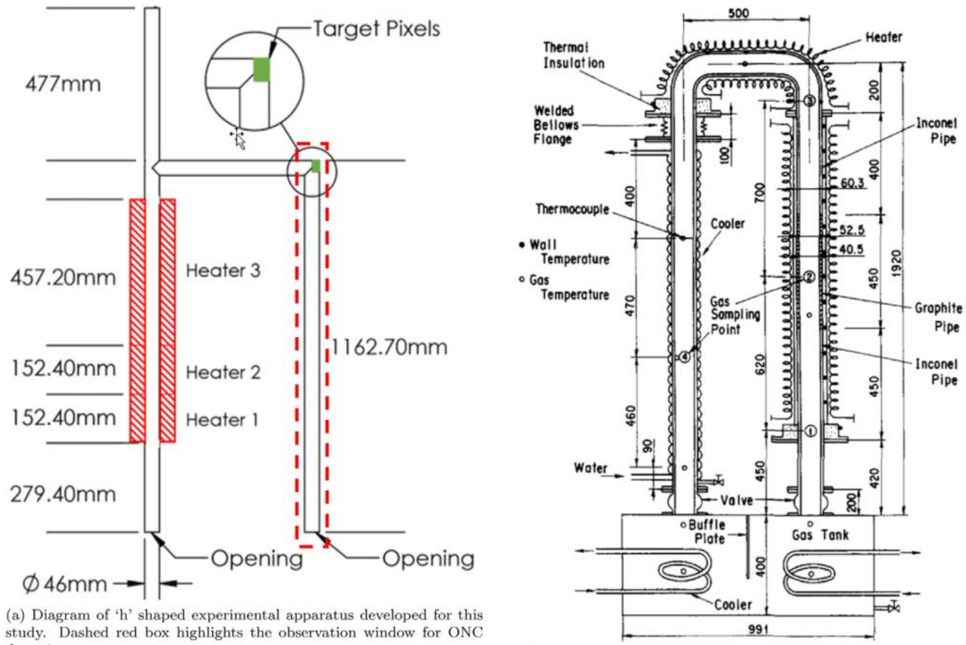

(a) Diagram of 'h' shaped experimental apparatus developed for this study. Dashed red box highlights the observation window for ONC detection.

(b) Diagram of 'inverse U' shaped experimental apparatus from JAERI. shown dimensions in mm. [23]

Figure 22. Schematic of the inverted h-tube experimental configuration used by Gould et al. along with a comparison of the Hishida and Takeda apparatus.

However, Gould et al. have implemented a novel, visual method of free convection determination. Specifically, a forward-looking infrared (FLIR) camera was focused on a selected area, highlighted in Figure 23 as the target pixels. Because air is progressing vertically through the heated region during the experiment, a sharp inflection at the expected area is used to diagnose the onset of free convection. This diagnosis is paired with velocity measurements, which provide verification that bulk motion is in fact occurring. However, one should note the calculated and experimental velocities at ONC – approximately 0.2 m/s, which is a very low velocity at which to achieve precise results. Experimental uncertainties on the order of 25% of reading are reported.

Figure 23 presents a series of images taken by the setup immediately prior to, during, and after ONC. While it was unappreciated at the initial reading, the relative simplicity of implementation and diagnostic fidelity are to be appreciated. That is, relatively little uncertainty regarding onset time is available graphically. As mentioned previously, velocimetric data provided little actionable information, as shown in Figure 24; though, as confirmatory data its value is well understood [29].

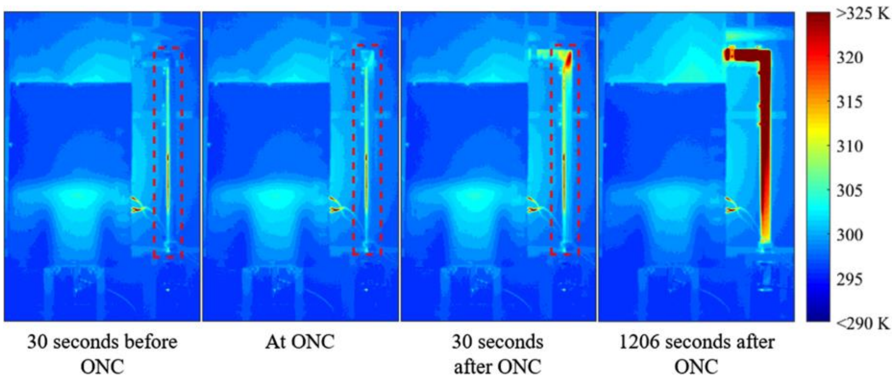

Figure 23 FLIR images immediately before, during, and after the onset of natural convection (ONC).

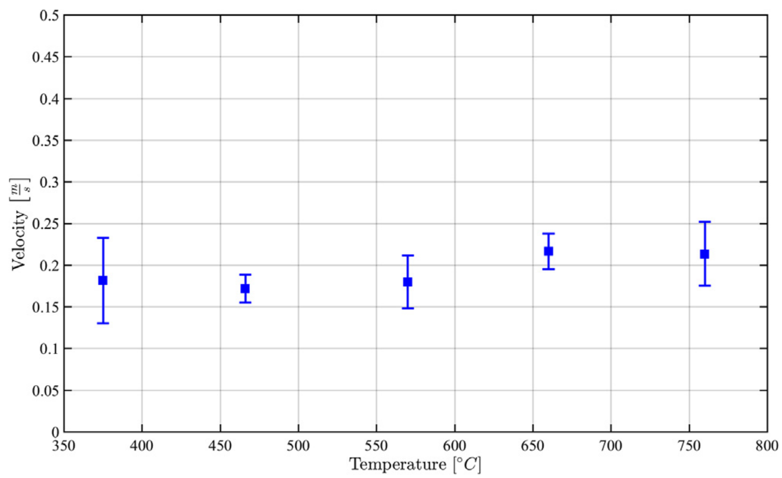

Figure 24. Flow velocity from h-bend apparatus at ONC, presented as a function of leg temperature.

The experimental procedure largely follows the format expected from Hishida and Takeda's precedent.

i. Air is evacuated from the chamber using a vacuum pump to achieve a rough vacuum[1].

ii. Helium backfill is applied until an equilibrium pressure is achieved (atmospheric).

iii. Heat is applied until the desired temperature in the hot leg is achieved.

iv. Excess helium is released to achieve equilibrium.

[1] Rough vacuum includes the range of 101 kPa - 3.33 kPa

v. Both of the lower ends are opened simultaneously.

vi. Flow transducer is moved into place under the left hand side (heated side) of the apparatus.

vii. Chamber wall temperature and flow rate are monitored for onset determination.

To give an indication of ONC diagnosis, the analyses presents the thermal response of the target pixels, as shown in Figure 25.

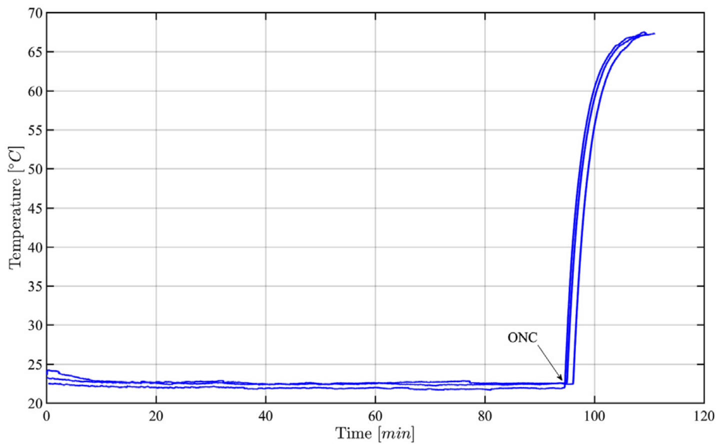

Figure 25. Average temperature of target pixels at ONC.

Interestingly, this work noted a similar correlation to hot leg temperature and ONC time, though contemporary estimates place ONC time as initiating over an hour ahead of previous estimates. Table 10 provides the relevant setup dimensions for comparison.

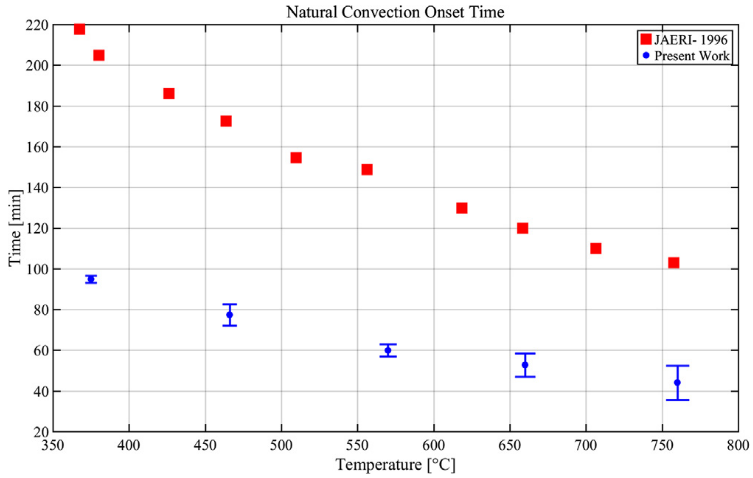

Figure 26. Onset of natural convection time of Gould and JAERI apparatus, presented as a function of hot leg temperature.

Table 10. Experimental parameters for comparison to the JAERI experiment.

Parameter	*Gould et al.*	*JAERI* [30]
Leg length (m)	1.216	1.92
Heated length (m)	0.82	1.50
Interior diameter (mm)	46	40.5
Ingressing fluid	Air	N_2

The discussion attributes the ONC hot leg temperature dependence to increased molecular diffusion, and increased density driven convection currents within the hot leg. That is, this study asserts that intra-leg currents are more prevalent at higher temperatures and may play an accelerating role towards ONC. However, the effect of an upper plenum reservoir of helium may also play an accelerating role as well.

However, this assertion towards intra-leg currents is particularly germane, as it seems to directly contradict the quiescent assumption placed on previous works. Rather, it ties the nonlinear dependence of ONC hot leg temperature to internal convective phenomena rather than diffusion, though the convective heat and mass transport path is not specified in this work.

2.3.10 Simulation of the Depressurized Conduction Cooldown Event in the HTTF

As part of the HTTF's air ingress event experimental effort, initial computational efforts were performed by Robert Aldridge using the RELAP 5 software tool [16]. This computational effort is of particular interest to this work, as it provides insights into phenomenological progression within a two vessel facility. In particular, the following research objectives are provided that are particularly relevant to the current experimental effort

Complete numerical simulations and compare the following figures of merit within the GT-MHR and the HTTF:

i. Radial temperature profile,

ii. Air front speed moving through the vessel during the molecular diffusion phase,

iii. Time to onset of natural convection,

iv. Natural convection flow rate.

This is a necessarily large effort, and it is not at all necessary to review in its totality. Rather, it is the consideration of the air ingress event as two distinct scenarios that, again, is of interest to this work. Namely, it is assumed a diffusive phase will eventually transition a natural convection phase, and H2TS analysis is applied to the conservation equations of each scenario. That differential application is the focus of this next sections.

Air Ingress Scaling Analysis

Before proceeding further, a note: As may or may not have become obvious, scaling analysis has a wide range of variability with respect to application. Therefore, it is most useful when applied carefully, and deliberately. Aldridge provides the following diagram in order to motivate this scaling analysis, helpfully identifying the distinction between bulk phenomena considered by the top-down analysis, and the component transfer processes considered by the bottom-up analysis. It should be noted that such multi-level consideration has been notably absent from other analyses.

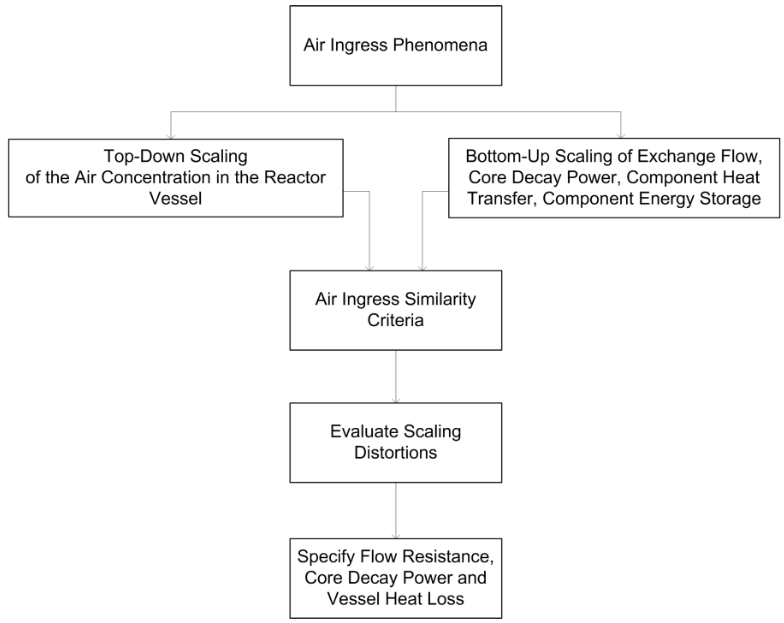

Figure 27. Flow diagram motivating the scaling analysis of the air ingress event within the HTTF.

In this section, initial assumptions are applied as follows. One may note the similarity to previous analyses [3] [13].

i. Uniform fluid properties for a given cross section,

ii. Incompressible flow (Ma<0.2),

iii. Diffusion coefficient is independent of gas concentration.

iv. Molar average velocity may be used in the momentum equation.

From this, the following differential conservation equations are presented: mass mixture, continuity, integrated loop momentum, and energy, as shown in Equations 2.31-35.

$$\dot{m}_{loop} = \dot{m}_i \qquad 2.31$$

$$\frac{\partial \chi_{H,C}}{\partial t} + w\frac{\partial \chi_{H,C}}{\partial z} = D_{H,C}\frac{\partial^2 \chi_{H,C}}{\partial z^2} \qquad 2.32$$

$$\frac{d\dot{m}}{dt}\sum_i \frac{l_i}{a_i} = (\rho_H - \rho_C)gH - \frac{\dot{m}^2}{\rho a_B^2}\sum_i \frac{1}{2}\left(\frac{fl}{d_h} + K\right)_i \left(\frac{a_B}{a_i}\right)^2 \qquad 2.33$$

$$\rho c_v \frac{\partial T}{\partial t} + \rho c_p w \frac{\partial T}{\partial z} = k \frac{\partial^2 T}{\partial z^2} + q'''_{loss} + q'''_{str} + q'''_{core} \qquad 2.34$$

The work necessarily assumes ideal gas conditions, and with it the following equation of state shown in Equation 2.35.

$$\rho = \frac{P_{vessel}}{RT} \left[\chi_{air} M_{air} + \chi_{He} M_{He}\right] \qquad 2.35$$

Normalizing parameters are selected in the following way:

$$\dot{m}^*{}_{loop} = \frac{\dot{m}_{loop}}{\dot{m}_{loop,0}} = \frac{\dot{m}_{loop} L}{\rho_{avg,loop,0} a_B D_0} \qquad w^* = \frac{w}{w_0} = \frac{wL}{D_0} \qquad \chi^*_{air} = \frac{\chi_{air}}{(\chi_{He})_{avg,core,0}}$$

$$\chi^*_{He} = \frac{\chi_{He}}{(\chi_{He})_{avg,core,0}} \qquad \sum_i \left[\frac{1}{2}\left(\frac{fl}{D_h} + k\right)_i \left(\frac{a_{core}}{a_i}\right)^2\right]^* = \frac{\sum_i \left[\frac{1}{2}\left(\frac{fl}{D_h} + k\right)_i \left(\frac{a_{core}}{a_i}\right)^2\right]^*}{\sum_i \left[\frac{1}{2}\left(\frac{fl}{D_h} + k\right)_i \left(\frac{a_{core}}{a_i}\right)^2\right]_0}$$

$$z^* = \frac{z}{L} \qquad \rho^* = \frac{\rho}{\rho_0} \qquad \left(\rho_{avg,UP} - \rho_{avg,core}\right)^* = \frac{\left(\rho_{avg,UP} - \rho_{avg,core}\right)}{\left(\rho_{avg,UP} - \rho_{avg,core}\right)_0}$$

$$c^*_p = \frac{c_p}{\left(c_{p,avg,loop}\right)_0} \qquad c^*_v = \frac{c_v}{\left(c_{v,avg,loop}\right)_0} \qquad k^* = \frac{k}{\left(k_{avg,loop}\right)_0}$$

$$D^* = \frac{D}{D_0} \qquad q'''_i = \frac{q'''_i}{q'''_{i,0}}$$

The convective-diffusive continuity equation and energy transfer equation are identified as governing local phenomena, while the loop continuity equation and integrated loop momentum balance equation are identified as responsible for top-down scaling behavior description. Interestingly, the author goes on to assert the minimal contributions of the convective-diffusive continuity equation to the overall transient – an odd choice given the molecular diffusion phenomena under description.

Regardless, substitution of the normalizing parameters into the appropriate equations yields the following dimensionless expressions shown in Equations 2.36-38.

$$\frac{\partial \chi^*_{H,C}}{\partial t^*} + w^* \frac{\partial \chi^*_{H,C}}{\partial z} = D^*_{H,C} \frac{\partial^2 \chi^*_{H,C}}{\partial z^{*2}} \qquad 2.36$$

$$\Pi_G \frac{d\dot{m}^*}{dt^*} = \Pi_{Ri}(\rho_H - \rho_C)^* - \Pi_F \frac{\dot{m}^{*2}}{\rho^*_{avg,loop}} \left[\sum_i \frac{1}{2} \left(\frac{fl}{d_h} + K \right)_i \left(\frac{a_B}{a_i} \right)^2 \right]^* \qquad 2.37$$

$$\frac{\rho^* c_v^*}{\gamma_{diff}} \frac{\partial T^*}{\partial t^*} + \rho^* c_p^* w^* \frac{\partial T^*}{\partial z^*} = \frac{k^*}{\Pi_{Le}} \frac{\partial^2 T^*}{\partial z^{*2}} + \sum_i \Pi_i q^{*'''}_i \qquad 2.38$$

The scaling groups represent the contributions of problem geometry, Richardson number, Lewis number, along with parasitic energy loss, stored energy, and core generation as the volumetric source terms. They are presented mathematically in Equations 2.39-2.44.

$$\Pi_G = \sum_i \frac{a_{core} l_i}{l_0 a_i} \qquad 2.39$$

$$\Pi_{Ri} = \frac{g(\rho_H - \rho_{avg})_0 L}{\rho_{C,0} w^2_{C,0}} \qquad 2.40$$

$$\Pi_F = \frac{\rho_C}{\rho_{avg,0}} \sum_i \left[\sum_i \frac{1}{2} \left(\frac{fl}{d_h} + k \right)_i \left(\frac{a_{core}}{a_i} \right)^2 \right]_0 \qquad 2.41$$

$$\Pi_{Le} = \frac{\rho_{avg,loop,0} c_{p,avg,loop,0} D_0}{k_{avg,loop,0}} \qquad 2.42$$

$$\Pi_i = \frac{q^{*'''}_i}{\rho_{avg,loop,0} c_{p,avg,loop,0} \Delta T_{core,0} D_0} \qquad 2.43$$

$$\gamma_{diff} = \frac{c_{p,avg,loop,0}}{c_{v,avg,loop,0}} \qquad 2.44$$

Through this, a common time scale is identified, and presented in Equation 2.45.

$$t^* = \frac{t}{\tau_{diff}} = \frac{tD_0}{L^2} \qquad 2.45$$

Therefore, the assertion for this work is that by application of the conservation equations, and consideration of the convective-diffusive equation is not prioritized, mind, is through preserving the ratio of the diffusion coefficient to the square of the length scale, temporal similarity of the transient is achieved. This is expressed mathematically with the reference parameter, $\boldsymbol{\tau_R}$, defined in Equation 2.46.

$$\tau_R^* = \left(\frac{L^2}{D_0}\right)_R = \frac{\left(\frac{L^2}{D_0}\right)_M}{\left(\frac{L^2}{D_0}\right)_P} \qquad 2.46$$

The work goes on to utilize the same process to describe the internal heat transfer of the reactor vessel. The analysis is comprehensive, and well worth consideration for the motivated reader. It concludes with the relation of the volumetric loss parameter to the heat gain of the RCCS, as transported via radiative transfer.

The point is the highlight singular treatment of the air ingress as molecular diffusion, similar to the analysis presented initially by Hishida and Takeda, and then propagated by Reyes et al., despite the tacit assertion that remote phenomena will influence momentum driven phenomena. However, the reference parameter in all analytical treatments is still clearly dominated by the diffusion coefficient, even after both top-down and bottom-up treatment.

Natural Circulation Scaling Analysis

The introduction of the natural circulation is blessedly succinct and quoted directly [16]:

Once buoyancy forces are sufficient to induce buoyant driven flow, the natural circulation phase of the DCC event will begin.

Here again, the tacit assumption that some period of molecular diffusion must necessarily precede the onset of natural convection is very clearly at work. However, this section of the analysis provides greater emphasis on kinetic phenomena, such as gaseous expansion. Figure 28 presents the flow chart motivating the natural convection scaling analysis.

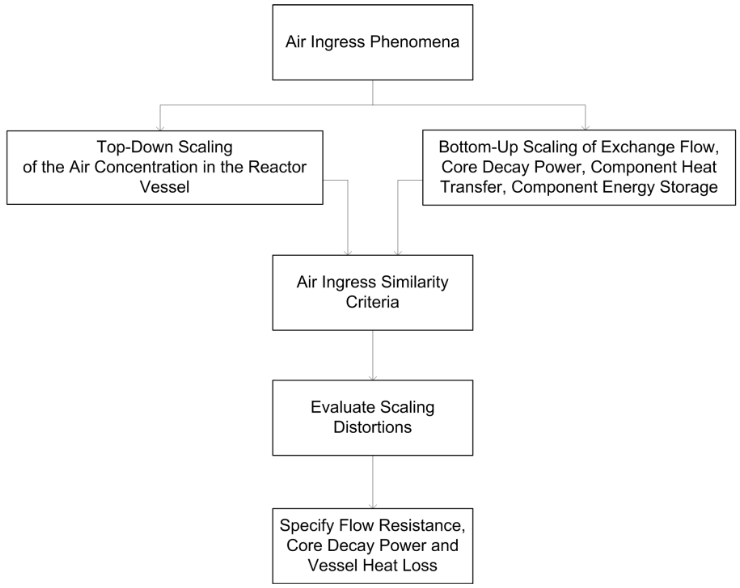

Figure 28. Flow chart motivating the scaling analysis for natural convection within the HTTF.

This scaling analysis declared the following assumptions:

i. Flow is one-dimensional along the loop axis,

ii. Uniform properties at a cross section,

iii. Incompressible flow (Ma<0.2),

iv. Pressure losses in the core dominate flow resistance,

v. Viscous dissipation is negligible.

There are some distinct differences between this particular set of assumptions and those of the air ingress. However, it is the omission of the molar velocity that is of note, as it is a tacit recognition that velocities are expected to be of one or more orders of magnitude greater for this stage of the transient.

The momentum balance for the loop is described by Equation 2.48, which presents very similarly to other analyses, but with an additional resistive term to account for momentum losses from volumetric expansion of the working fluid. Again combining the top-down and bottom-up steps into consideration of the conservation of mass, linear momentum, and energy, Aldridge presents Equations 2.47-49 to describe the transport phenomena.

$$\frac{\partial \chi_{H,C}}{\partial t} + w\frac{\partial \chi_{H,C}}{\partial z} = D_{H,C}\frac{\partial^2 \chi_{H,C}}{\partial z^2} \tag{2.47}$$

$$\frac{d\dot{m}}{dt}\sum_i \frac{l_i}{a_i} = (\rho_H - \rho_C)gH - \frac{\dot{m}^2}{\rho a_B^2}\sum_i \frac{1}{2}\left(\frac{fl}{d_h} + K\right)_i \left(\frac{a_B}{a_i}\right)^2 - \frac{\dot{m}^2}{\rho_C a_B^2}\frac{\beta(T_H - T_C)}{1 - \beta(T_H - T_C)} \tag{2.48}$$

$$\rho c_v \frac{\partial T}{\partial t} + \rho c_p w \frac{\partial T}{\partial z} = k\frac{\partial^2 T}{\partial z^2} + q'''_{loss} + q'''_{str} + q'''_{core} \tag{2.49}$$

Upon dimensional analysis, this term becomes the natural convection expansion shown in Equation 2.50. The additional scaling groups are presented as well,

$$\Pi_G \frac{d\dot{m}^*}{dt^*} = \Pi_{Ri}(\Delta\rho^*) - \Pi_F \frac{\dot{m}^{*2}}{\rho^*}\left[\sum_i \frac{1}{2}\left(\frac{fl}{d_h} + k\right)_i \left(\frac{a_{core}}{a_i}\right)^2\right]^* - \Pi_E \frac{\dot{m}^{*2}}{\rho^*}\left[\frac{\beta(T_H - T_C)}{1 - \beta(T_H - T_C)}\right]^* \tag{2.50}$$

$$\Pi_{E,NC} = \frac{\rho_c}{\rho_{avg,loop}}\left[\frac{\beta(T_H - T_C)}{1 - \beta(T_H - T_C)}\right]_0 \qquad \Pi_G = \sum_i \frac{a_{core} l_i}{l_0 a_i} \qquad \Pi_{Ri} = \frac{g\left(\rho_H - \rho_{avg}\right)_0 L}{\rho_{C,0} w_{C,0}^2}$$

$$\Pi_F = \frac{\rho_C}{\rho_{avg,0}}\sum_i \left[\sum_i \frac{1}{2}\left(\frac{fl}{d_h} + k\right)_i \left(\frac{a_{core}}{a_i}\right)^2\right]_0$$

$$\frac{\rho^* c_v^*}{\gamma_{diff}}\frac{\partial T^*}{\partial t^*} + \rho^* c_p^* w^* \frac{\partial T^*}{\partial z^*} = \frac{k^*}{\Pi_{Le,diff}}\frac{\partial^2 T^*}{\partial z^{*2}} + \sum_i \left(\Pi_i q'''^*_i\right) \tag{2.51}$$

$$\Pi_{Le,diff} = \frac{\rho_{avg,loop,0} c_{p,avg,0} D_0}{k_{avg,loop,0}} \qquad \Pi_i = \frac{q'''_i L^2}{\left(\rho c_p\right)_{avg,loop,0} \Delta T D_0} \qquad \gamma_{diff} = \frac{c_{p,0}}{c_{v,0}}$$

A dominant time constant is declared by equation the fluid mass to the internal mass flow rate, as shown in Equation 2.52. Similarly, the reference length definition is presented in Equation 2.53.

$$\tau = \frac{M_{g,vessel,0}}{\dot{m}_{loop}} = \frac{M_{g,vessel,0}}{\rho_{C,0} w_0 a_B} \tag{2.52}$$

$$\boldsymbol{l_0 = \frac{M_{g,vessel,0}}{\rho_{C,0} a_B}} \qquad 2.53$$

The focus of this analysis is determination of a characteristic natural convection velocity, achieved by application of steady conditions, and neglect of the gaseous expansion term, presented below. Combined with a core energy balance, the Richardson may be presented as shown in Equation 2.54, provided one lastly assumes a unity value for the Richardson number to achieve the core velocity presented in Equation 2.55.

$$\boldsymbol{\Pi_{Ri} = \Pi_F} \qquad 2.54$$

$$\boldsymbol{\Pi_{Ri} = \frac{\beta_{g,ves} g \dot{q} L}{\left(\rho_{avg} w_{avg,core}^3 a_B c_{p,avg}\right)}} \qquad 2.55$$

$$\boldsymbol{w_{avg,core} = \left(\frac{\beta_{g,ves} g \dot{q} L}{\rho_{avg,core} a_B c_{p,avg} \Pi_F}\right)^{\frac{1}{3}}} \qquad 2.56$$

Lastly, the heat transfer through the solid structure is noted, but now confidently asserting a convective force within the core region. Therefore, the Curchill-Chu correlation is provided as the heat transfer boundary condition. The correlation is presented in Equation 2.57, as tradition requires for a thermal hydraulics dissertation; however, this section again tacitly reasserts the following assumption:

Heat and mass transfer is dominated by radiation during the air ingress phase, and via convection only after the onset of natural convection within the core.

$$\boldsymbol{Nu_L = \left[0.825 + \frac{0.387 (Ra_L)^{\frac{1}{6}}}{\left[1 + \left(\frac{0.492}{Pr_g}\right)^{\frac{9}{16}}\right]^{\frac{8}{27}}}\right]^2} \qquad 2.57$$

For clarity, $\boldsymbol{Ra_L}$ refers to the average Rayleigh number, and $\boldsymbol{Pr_g}$ refers to the Prandtl number of the gas.

This assumption of dominance of radiative transport speaks again to a larger assumption that the helium volume within the core region will be quiescent, acting as a retardant momentum blanket prior to the onset of natural convection, as can be seen in this analytical treatment. With that stated, one is encouraged to turn one's attention to the computational model used to support the analysis, in order to inform expected experiment progression, duration, and parametric results.

Computational Model

The model built is based on the GT-MHR Preliminary Safety Information Document (PSID) [31], and the MHTGR Benchmark Definition [32].

Figure 29 presents the nodalization used to represent the prototype facility (GT-MHR, left) and the model facility (HTTF, right). They are presented so in order to highlight the heat transfer path simulated.

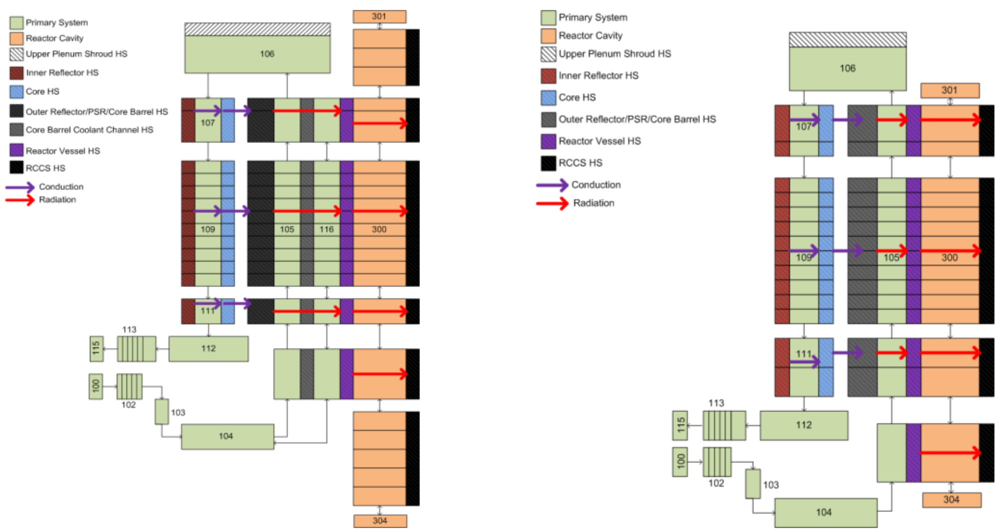

Figure 29. RELAP5-3D nodalization for the model (left) and prototype (right) facilities.

The heat transfer path is of critical importance. The heater rods transfer heat via conduction to the solid moderator structure – graphite in the GT-MHR, Greencast-94F in the HTTF. That heat is transferred to the coolant via coolant channels. Upper and lower plena are joined via the coolant channels and by the upcomer. The inner and outer reflectors conduct core heat to the core barrel, which communicates to the RCCS via radiation. The RCCS is treated as having a constant temperature of 40C on the non-radiating side.

Table 11 provides the initial conditions implemented in the GT-MHR model; Tables 12 and 13 provide the initial conditions used for the HTTF under the SET and IET configurations. Note the constant temperature profile condition in the core volumes. Additionally, the analysis notes the initial mass flow rate was forced to zero (0).

The separate effects test configuration and integral effects test configuration differ in that the separate effects configuration pressure similarity is assumed, whereas a 1:8 ratio is assumed for the integral configuration.

Table 11. Initial conditions applied to the GT-MHR model for the molecular diffusion phase of the air ingress event.

Volume Number	*Air Mass Fraction*	*Temperature (K)*	*Pressure (MPa)*
102 to 105-01; 116-01	1.0	340	0.101
105-02 to 111	0.0	634	0.101
112 to 113	1.0	340	0.101
150	1.0	340	0.101

Table 12. Initial conditions applied to the HTTF model SET for the molecular diffusion phase of the air ingress event.

Volume Number	*Air Mass Fraction*	*Temperature (K)*	*Pressure (MPa)*
102 to 105-01	1.0	340	0.101
105-02 to 111	0.0	634	0.101
112 - 113	1.0	340	0.101

Table 13. Initial conditions applied to the HTTF model IET for the molecular diffusion phase of the air ingress event

Volume Number	*Air Mass Fraction*	*Temperature (K)*	*Pressure (kPa)*
102 to 105-01	1.0	340	12.625
105-02 to 111	0.0	634	12.625
112 to 113	1.0	340	12.625

Decay heat was applied using a decay heat curve, which was also applied to the HTTF, but scaled according to its 1:4 power scaling ratio – at least when the 2.2MW operational power limits permit. Initial values of 5.6MW are noted, and slight distortions provided by this lack similarity are assumed negligible. Table 14 presents a summary of the GT-MHR results.

Table 14. Key computational results for GT-MHR RELAP5 simulation.

Parameter	Ingressing air front velocity (m/s)	Natural convection trigger time (hr)	Natural convection flow rate (kg/s)	$\chi_{air}(t_{ONC})$
Value	0.03	13.2	0.18	0.96

Table 15 presents similar computational results for the SET configuration, and Table 16 the IET. The author notes that RELAP under-predicts the nitrogen mass fraction in the HTTF at ONC as compared to the GT-MHR – 90% compared to the previous 96%. The author also notes initial deviation in ingress velocities.

Table 15. Key computational results for HTTF SET model simulation.

Parameter	Ingressing air front velocity (m/s)	Natural convection trigger time (hr)	Natural convection flow rate (kg/s)	$\chi_{air}(t_{ONC})$
Value	0.1	1.07	NA	0.90

Table 16. Key computational results from the HTTF IET model simulation.

Parameter	Ingressing air front velocity (m/s)	Natural convection trigger time (hr)	Natural convection flow rate (kg/s)	$\chi_{air}(t_{ONC})$
Value	0.04	1.59	6.8E-4	NA

The analysis notes significant distortion in the IET configuration, citing the Colburn-Hougen method of diffusion coefficient calculation, which violates the pressure-independent assumption applied previously. Additional distortion is noted in the Richardson number, which further contributes to the perceived distortion. Additionally, temperature profile comparisons indicates the contribution of heat transfer to distorted ONC times, as shown in Figure 30.

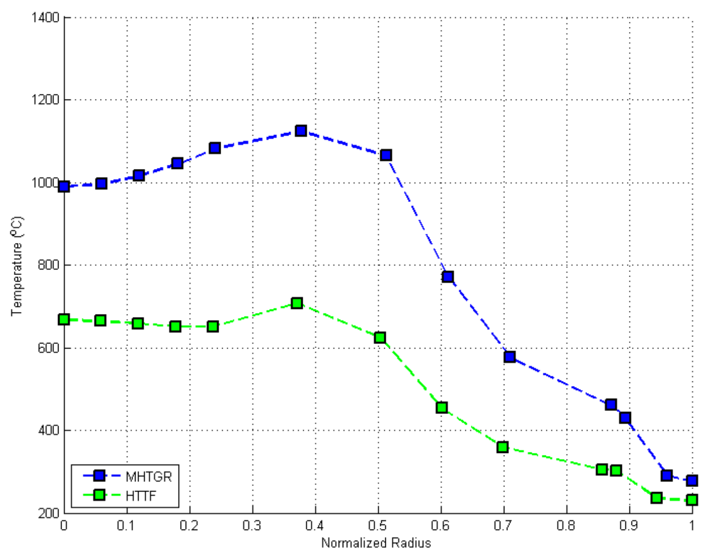

Figure 30. Radial temperature profile of the GT-MHR and the HTTF IET at ONC.

Finally, the experimental effort goes on to conclude that the following will be well predicted within the HTTF as a SET:

i. Diffusion of air into the reactor vessel,

ii. Transition to natural circulation,

iii. Normalized peak fuel temperature heat up rate during the middle of the molecular diffusion phase.

However, heat up rate during the beginning and end of the diffusive phase, and heat transfer to the in-vessel solids are not well preserved. And a call to reassess pressure-independence of the diffusion coefficient is tendered.

This work is of interest, as it clearly identifies heat transfer paths that are the design basis for the SFSETF, informs initial conditions, and provides experimental duration estimate, but it also provides evidence, along with others in the field, that consensus regarding the air ingress event is not established. Deviations in results are attributed, frequently, to the diffusion coefficient. However, it may just as well be likely that the phenomenological understanding needs to be challenged.

3 Thesis Statement

Therefore, this section shall conclude with the following thesis statement, and experimental hypothesis.

Previous and foundational works may have been subject to implicit errors which have biased ONC estimations based on diffusive ingress mechanisms. Furthermore, implicit treatment of the interior helium inventory as a quiescent volume is inappropriate.

Clarifying statement: Inverted tube experiments bias initial ingress mechanisms towards diffusion by forcing initial diffusive ingress boundary conditions that are not in place in other geometries. Rather, the air ingress will be dominated by precluding air access to pre-existing convective currents that will naturally arise through thermal gradients imposed by the geometry of the facility, as well as the functionality of the RCCS. It is therefore the goal of this work to demonstrate and quantify the role of ingress geometry in air accessing the lower plenum.

3.1 Hypothesis

Diffusive ingress biases experimental results. Therefore, recreation of diffusive ingress mechanics will have demonstrable effect on ONC time in a similar facility. This may be stated as a null hypothesis in the following way

$$\boldsymbol{H_0}: \boldsymbol{\tau_{ONC}}(\boldsymbol{diff}) = \boldsymbol{\tau_{ONC}}(\boldsymbol{con})$$

Rejection of that hypothesis directly confirms the importance of ingress mechanics on event progression.

4 Model and Methodology

4.0.1 Problem Statement

This section will clearly outline the problem statement for this experimental effort, as it informs the remainder of the experimental effort. It also provides analytical justification for deviation of this scaling analysis from previous efforts, as well as motivating later design and instrumentation choices.

From the hypothesis statement, one may determine that convective contributions to heat and mass transport are of primary concern. Therefore, consider the following analysis in order to quantify convective initial conditions in an experimental setting.

Consider a flow channel with a constant heat flux input, presented schematically in Figure 31. Whereas a sealed flow channel may well represent the inverted tube experimental configuration, this work asserts that an open channel may be more useful, and descriptive as it maintains the potential for fluidic communication between upper and lower plena.

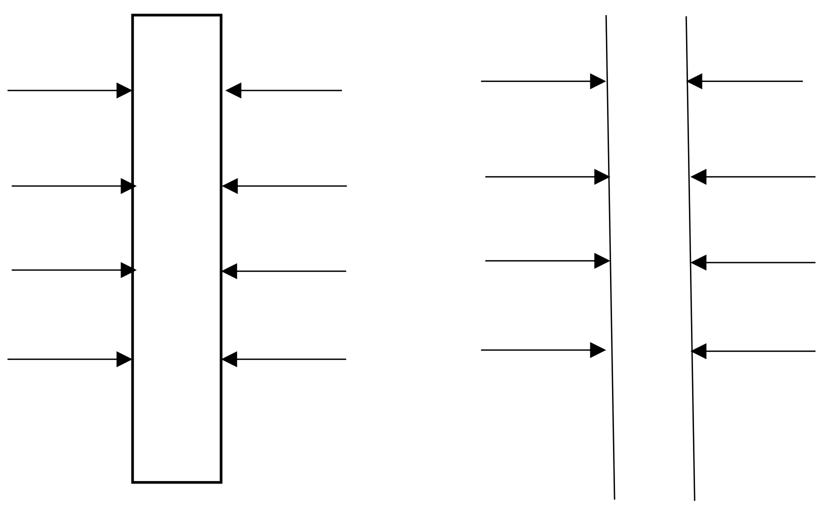

Figure 31. Coolant channel configurations; sealed shown left and, open channel shown right.

Construct a control volume that approaches the interior of the channel walls. Steady, quiescent conditions do not apply yet, but viscous forces are to be neglected. Assuming an initial volume of exclusively air and incompressibility leads to Equation 4.2. For the sake of clarity, $\boldsymbol{v}$ corresponds to the vertical velocity.

$$\frac{\partial(\rho v)}{\partial t} + u\frac{\partial v}{\partial x} + v\frac{\partial v}{\partial y} = -\frac{\partial P}{\partial y} + \mu\left(\frac{\partial^2 v}{\partial x^2} + \frac{\partial^2 v}{\partial y^2}\right) - \rho g \quad 4.1$$

$$\frac{\partial v}{\partial t} + v\frac{\partial v}{\partial y} = g\beta(T - T_\infty) \quad 4.2$$

In order to accurately depict initial convective force, it is necessary to integrate the buoyancy force over the channel length, as done in Equation 4.3, in order to determine initial velocities.

$$\int_0^L \left(\frac{\partial v}{\partial t} + v\frac{\partial v}{\partial y} = g\beta(T - T_\infty)\right) dy \quad 4.3$$

This presents a sizable challenge, as it requires spatial and temporal integration to achieve an expression for velocity. However, if one assumes steady conditions prior to experimental initiation, this may be simplified into an ordinary differential equation that may be solved using separation of variables yielding the results presented in Equation 4.4.

$$v\, v' = g\beta\big(T(y) - T_\infty(y)\big) \quad 4.4$$

If one assumes a constant difference between the wall and fluid temperature along the length of channel, as some works have [33], this nonlinear differential equation is separable with respect to y, and has a solution of the form

$$v(y) = \sqrt{2 \times (c_1 + g\beta y \Delta T)} \quad 4.5$$

Solve for the constant of integration by assuming a sufficiently small boundary velocity at the datum commensurate with previous experimental efforts such that it may be easily ignored, leaving

$$v(y) = \sqrt{(2g\beta y \Delta T)} \quad 4.6$$

$$v(y = 1.75m) = \sqrt{(2g\beta y \Delta T)} \approx 2.11\ m/s \quad 4.7$$

Of course, this is to be expected given a heated, vertical channel. However, it also means that initial velocities may be significantly higher than the diffusive values reported elsewhere.

However, this provides an initial estimate towards steady convective mass transport within the core region prior to any ingress, for N number of coolant channels, as shown in Equation 2.65. Equation 2.67 provides an estimate for the reference mass transport number, which may be used to determine similarity of mass flow between facilities under steady conditions, assuming similarity of temperature profiles.

$$\dot{\boldsymbol{m}}_{\boldsymbol{0}} = \boldsymbol{N} \times \boldsymbol{a}_{\boldsymbol{xs}} \sum_{\boldsymbol{i}} \boldsymbol{\rho}_{\boldsymbol{i}} \boldsymbol{v}_{\boldsymbol{i}} \tag{4.8}$$

$$\dot{\boldsymbol{m}}^{*}{}_{\boldsymbol{R}} = \sqrt{\boldsymbol{L}\boldsymbol{\Delta}\boldsymbol{T}}_{\boldsymbol{R}} \tag{4.9}$$

This however presents a challenge when describing the role of diffusion, as it is seemingly absent from consideration. Consider the integrated momentum balance, shown in Equation 4.10, and implemented in Hishida and Takeda's differencing scheme [3]. Boundary conditions are applied, as in the Survey of Literature section of this document, and the following initial conditions are reported at the entrance to the hot side section of the apparatus.

$$\frac{\boldsymbol{\partial U^{*}}}{\boldsymbol{\partial t}} \int \boldsymbol{\rho dx} = -\int \boldsymbol{dP} \pm \boldsymbol{g} \int \boldsymbol{\rho dx} + \frac{\boldsymbol{1}}{\boldsymbol{2}} \boldsymbol{\rho U^{*}} |\boldsymbol{U^{*}}| \left(\frac{\boldsymbol{f}}{\boldsymbol{D_e}} \int \boldsymbol{\rho dx} + \sum_{\boldsymbol{i}} \boldsymbol{\rho_i K_i} \right) \tag{4.10}$$

$$\boldsymbol{P} = \boldsymbol{P_0} - \boldsymbol{g} \int_{\boldsymbol{0}}^{\boldsymbol{x}} \boldsymbol{\rho}\, \boldsymbol{dx} \,; \boldsymbol{U^{*}} = \boldsymbol{0} \tag{4.11}$$

This is certainly true for their experimental apparatus, and contributes to the excellent agreement between the analytical and experimental results. However, this work posits that they do not represent realistic boundary conditions, as $\frac{\boldsymbol{\partial U^{*}}}{\boldsymbol{\partial t}} \gg \boldsymbol{1e-5}; \boldsymbol{U^{*}} \gg \boldsymbol{1e-3}$. Moreover, given the bias towards diffusive ingress boundary conditions, the one-dimensionality of the fluid velocity is reasonable, even if it is amended in later iterations. However, if convection is expected to play a significant role, and all previous analyses agree in some way that it will, then it stands to reason that a multi-dimensional approach is necessary, and the previous scaling analysis, preserved in the following section, is no longer applicable. However, as it directly informed design efforts, the next sections will present the implemented scaling analysis, as well as a comprehensive description of the SFSETF, and its ability to interrogate the experimental hypothesis stated above.

4.0.2 Similarity of Fluidic Communication

If one assumes that maintenance of fluidic communication is necessary as part of proper scaling, then a two vessel design is necessary, as the second volume simulates the containment volume. Also, inclusion as a separate tank allows for the independent permutation of ingressing plume conditions, if desired. Particularly germane to this effort is the elbow bend located on the primary pressure vessel inferior cover plate, is shown clearly in Figure 32.

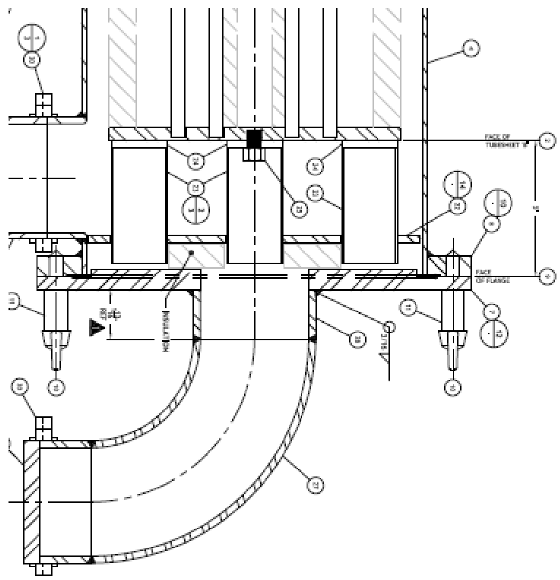

Figure 32. Elbow bend of the SFSETF lower plenum.

This deliberate design choice was made in order to actively interrogate the strength of ingress mechanics on transient progression.

Rather than considering air ingress as divided into phases, this analysis posits that gaseous kinetics will be constantly evolving throughout the transient, regardless of ingress mechanics, and initiating analysis there will provide more useful information. However, that introduces a significant challenge in determining initial conditions, as it essentially breaks established phenomenological progression.

Therefore, rather than reinventing this particular wheel, this work assumes the presence of convective currents, and that similarity will depend on local heat transfer and velocity gradients, as shown in Equation 4.12.

$$\int_0^L \left(\frac{\partial v}{\partial t} + v\frac{\partial v}{\partial y} = g\beta(T - T_\infty)\right) dy \qquad 4.12$$

Evaluation of this particular expression, in addition to the integrated loop energy equation is beyond the scope of this experimental effort, as it will necessarily require the interrogation of temperature profile in several locations throughout the core. Moreover, assumption of mass transport via diffusion alone is challenging, as increased velocities imply mixing may be affected via complex convection, thereby reducing the utility of the equation of state, even as a function of concentration and partial pressures, as shown in Equation 2.69.

$$\rho_{mix} = \frac{P_{mix}}{RT} = \frac{\left(\chi_i P_i + (1 - \chi_i)P_j\right)}{RT} \qquad 4.13$$

Diffusion across semi-infinite reservoirs, and represented by the time dependent Laplacian of Equation 2.70, presents a convenient method of evaluating the concentration parameter. However, complex convection makes it far more difficult to evaluate, at least by non-computational means, as mixing will be governed strongly by the local convective currents. Numerically, it is asserted here that mixing is more strongly related to the turbulent viscosity term, presented in Equation 2.71. This further emphasizes the need for a multidimensional analysis.

$$\frac{\partial \chi}{\partial t} = D\frac{\partial^2 \chi}{\partial y^2} \qquad 4.14$$

$$\tau \equiv shear\ stress = \mu_{turb}\frac{\partial \overline{v_x}}{\partial y} \qquad 4.15$$

However, it is insufficient to simply assume a convective element, as it does not in any way address the data presented by other efforts that seem to indicate a diffusive mechanic. This work will provide insight into the effect that ingress mechanics have had on the phenomenological assumptions placed on HTGRs. With that firmly in mind, consider the facility overview of the SFSETF presented in Figure 33.

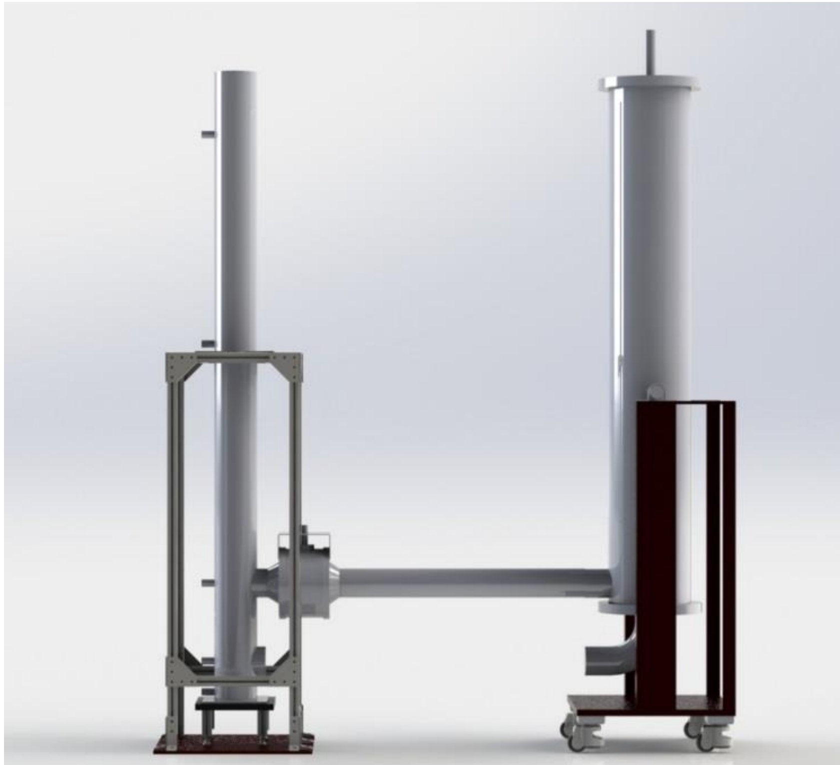

Figure 33. Render of the SFSETF facility, showing the vertical standpipe (left), connecting cross duct, and primary pressure vessel (right).

This configuration preserves the horizontal ingress mechanics presented in the GT-MHR configuration above in Figure 8, along with the HTTF configuration, but provides modularity for the HTTR vertical configuration of such interest, while minimally altering the scaling parameters derived for such phenomena.

A cross-sectional heat rejection path is provided in Figure 35. While reduced temperature precludes the needs for radiative rejection, conduction to the laboratory environment is sufficient to drive global heat transfer.

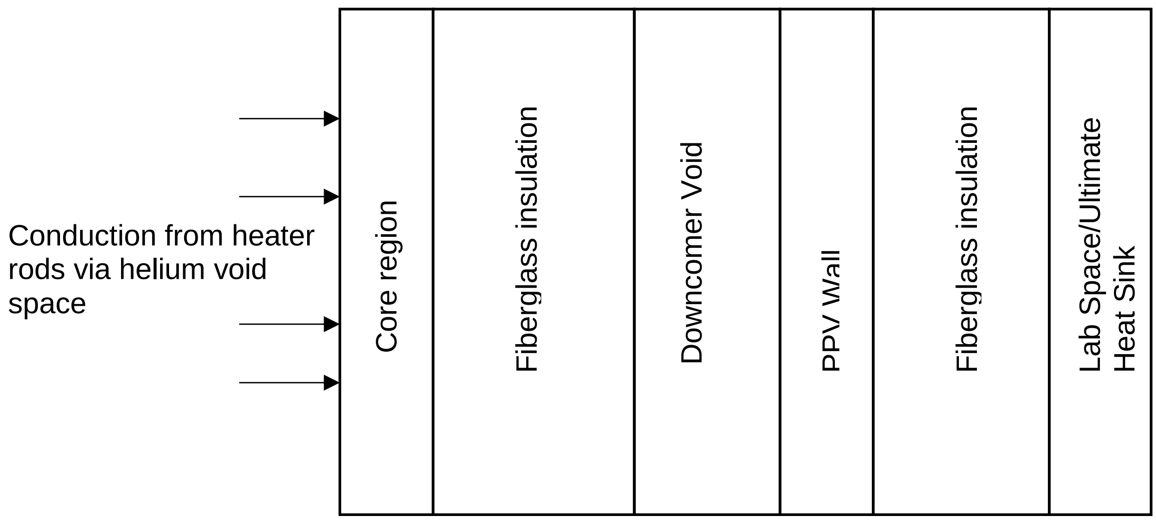

Figure 34. Heat transfer path implemented in the SFSETF.

4.1 Overview of the Stratified Flow Separate Effects Test Facility

4.1.0 Hierarchical Two-Tiered Scaling Analysis of the SFSETF

This section presents the scaling analysis that initiated this experimental effort. One may clearly see the inspiration from previous analyses. There are several considerations associated with the design of any thermal-hydraulics experiment. Scaling analysis was utilized to focus efforts towards identifying and preserving the dominant phenomena associated with this particular scenario. Of particular concern are the following events:

1. Air ingress via stratified flow within the cross duct,
2. Stratified air front propagation upward through the core, and
3. Onset of global natural circulation.

Fundamentally, a scaling analysis requires a full scale, or prototype, facility to utilize for reference. This study, following from analyses performed by Reyes and Oh (cite), selects the General Atomics gas turbine modular helium reactor (GT-MHR) as the prototypical facility.

To adequately describe all necessary phenomena, a two tiered methodology was implemented, beginning with a top-down approach with the continuity, integrated momentum balance and energy equations. To ensure relevance of the derived results, a bottom-up approach is implemented utilizing the differential conservation of mass, momentum and energy equations, in addition to heat transfer boundary conditions.

A list of key dimensions and associated scales, for this facility and others, is presented in Table 35.

Table 17. Key parameter values and scales for related experimental facilities

Parameter	Prototype (m)	HTTF (m)	HTTF Scale	1/8th Scale (m)	1/8th Scale	SFSETF (m)	SFSETF Scale
Vessel Height	23.700	5.925	0.250	2.963	0.125	2.045	0.086
Vessel ID	7.800	1.638	0.210	0.975	0.125	0.273	0.035
Vessel OD	8.400	1.663	0.198	1.050	0.125	0.311	0.037
Core Height	11.000	2.750	0.250	1.375	0.125	1.753	0.159
Active Core Height	7.800	1.950	0.250	0.975	0.125	1.740	0.223
Support Column Height	2.840	0.356	0.125	0.355	0.125	0.102	0.036
Hot Duct ID	1.500	0.298	0.199	0.179	0.119	0.102	0.068
Hot Duct Length	2.860	2.731	0.955	0.203	0.071	0.914	0.320

This provides a point of comparison between the proposed experimental facility and others, with respect to the vessel geometry.

The following assumptions were made:

1. One dimensional flow through a coolant channel.

2. The Boussinesq approximation is applicable.

3. Low fluid velocities (<10 m/s), and therefore incompressible flow is reasonable. Note: This does NOT mean that density is constant with respect to either time or position.

4. Ideal gas law is applicable

These assumptions are deliberately different from those presented in the seminal work performed by Hishida and Takeda (cite), and they are a significant departure from work that has built upon its foundation. The details of this departure, as they relate to the physical interpretation of facility behavior is thoroughly explored in this section.

This facility does not consider any retention volumes; therefore, mass flow rate at every cross section at the "*ith*" component is constant.

The hot/cold continuity equation is given as

$$\frac{\partial \rho_{H/C}}{\partial t} + w\frac{\partial \rho_{H/C}}{\partial x} = D_{H/C}\frac{\partial^2 \rho_{H/C}}{\partial x^2} \qquad 4.16$$

The hot/cold continuity equations state that the time rate of change of the mass of the hot or cold ($\rho_{H/C}$) gas is described by the convective-diffusive behavior of the flow. w is the molar velocity.

The integrated loop momentum balance equation is presented in Equation 4.17.

$$\frac{d\dot{m}}{dt}\sum_i \frac{l_i}{a_i} = (\rho_H - \rho_C)gH - \frac{\dot{m}^2}{\rho a_B^2}\sum_i \frac{1}{2}\left(\frac{fl}{d_h} + K\right)_i \left(\frac{a_B}{a_i}\right)^2 \qquad 4.17$$

The integrated loop momentum balance equation states that the time rate of change of momentum throughout a given flow loop is a balance between the sum of the aspect ratios for every "*ith*" segment, the buoyant forces represented by the densimetric difference and frictional/form loses.

Non-dimensionalization can be done by taking the ratio of each parameter to its boundary ($\boldsymbol{\Psi_B}$) or initial ($\boldsymbol{\Psi_0}$) condition. The normalizing parameter should be carefully selected so as to provide physical relevance to the ratio, and also achieve a value of approximately unity.

$$\dot{m}^* = \frac{\dot{m}}{\dot{m}_0} = \frac{\dot{m}}{\rho a_B w_0} \qquad \Delta\rho^* = \frac{\rho_H - \rho_C}{(\rho_H - \rho_C)_0} \qquad x^* = \frac{x}{L_0} \qquad F^* = \frac{\sum_i \frac{1}{2}\left(\frac{fl}{d_h} + K\right)_i \left(\frac{a_B}{a_i}\right)^2}{\left[\sum_i \frac{1}{2}\left(\frac{fl}{d_h} + K\right)_i \left(\frac{a_B}{a_i}\right)^2\right]_0} = \frac{F_i}{F_0}$$

$$w^* = \frac{w}{w_0} \qquad \rho^* = \frac{\rho}{\rho_0} \qquad H^* = \frac{H}{L_0}$$

Inserting the dimensionless parameters and collecting the resulting coefficients produces Equations 4.18 and 4.19. As a clarifying note, it is assumed that the active height ($\boldsymbol{H}$) and reference height ($\boldsymbol{L_0}$) are equivalent.

$$\frac{1}{\tau}\left[\frac{\partial\rho^*}{\partial t^*}\right] = \Pi_{cont}\frac{\partial\rho^*}{\partial t} = \left(\frac{D}{L_0^2}\right)\frac{\partial^2\rho^*}{\partial {x^2}^*} - \left(\frac{w_0}{L}\right)\frac{\partial\rho^*}{dx^*} = \Pi_{diff}\frac{\partial^2\rho^*}{\partial {x^2}^*} - \Pi_{con}\frac{\partial\rho^*}{dx^*} \tag{4.18}$$

$$\frac{\dot{m}_0}{\tau}\frac{L_0}{a_0}\frac{d\dot{m}^*}{dt^*}\sum_i \frac{l_i^*}{a_i^*} = \Delta\rho_0 g H(\rho_H - \rho_C)^* - \frac{\dot{m}_0^2}{\rho_{avg}a_0^2}\frac{{\dot{m}^*}^2}{\rho^* {a^*}_B^2}F_0\, F^* \tag{4.19a}$$

$$\frac{1}{\tau}\frac{d\dot{m}^*}{dt^*}\sum_i \frac{l_i^*}{a_i^*} = \Pi_{\mathrm{Ri}}(\rho_H - \rho_C)^* - \frac{\Pi_F}{\Pi_{Geom}}\frac{{\dot{m}^*}^2}{\rho^* {a^*}_B^2}F^* \tag{4.19b}$$

$$\Pi_{Geom} = \frac{L_0}{a_0} \qquad \Pi_{Ri} = \frac{(\Delta\rho)_0 g}{\rho_{avg} w_0} \qquad \Pi_F = \frac{\dot{m}_0}{\rho_{avg} a_0^2}F_0$$

This acknowledges that to maintain similarity with respect to continuity, one must achieve similarity with either the diffusive or convective time scales according to respective dominance. The historical challenge is that evaluation of these parameters often requires evaluation of passive phenomena, which resist such straightforward treatment.

One may infer that similarity with respect to momentum will be dependent on the geometry of the model facility, the velocities achieved and frictional losses. Now consider continuity, momentum and energetic phenomena through the appropriate conservation equations. These equations will be considered for the air ingress scenario, as well as the upward propagation of ingress air under steady conditions. Additionally, boundary conditions and other closure relationships will be considered as appropriate.

4.1.0.1 Scaling of the Differential Energy Equation

Energetic phenomena of interest will be limited to thermal energy rather than mechanical. Further, as this facility seeks to achieve similitude with respect to bulk fluid thermal response, micro-scale phenomena are neglected.

Consider the conservation of energy equation in the y-direction

$$\rho c_v \frac{\partial T}{\partial t} + \rho c_p w \frac{\partial T}{\partial y} = k \frac{\partial^2 T}{\partial y^2} + q'''_{loss} + q'''_{core} \qquad 4.20$$

k represents the thermal conductivity of the fluid. While the previously defined dimensionless parameters will be substituted, it should be made clear that dimensionless temperature is defined as follows for the energy equation, $T^* = \frac{T - T_{in}}{T_{out} - T_{in}} = \frac{\delta T}{\Delta T}$.

One finds that

$$\frac{\rho c_v \Delta T}{\tau} \frac{\partial T^*}{\partial t^*} + \frac{\rho c_p \Delta T w_0}{L_0} w^* \frac{\partial T^*}{\partial y^*} = \frac{k \Delta T}{L_0^2} \frac{\partial^2 T^*}{\partial y^{*2}} + q'''_{l,0}({q^*}'''_{loss}) + q'''_{core,0}\,(q'''_{core}) \qquad 4.21$$

Reorganization and substitution of the reference velocity according to the previous definition yields

$$\frac{1}{\tau} \frac{\partial T^*}{\partial t^*} + \frac{w_0}{L_0} w^* \frac{\partial T^*}{\partial y^*} = \frac{\alpha}{L_0^2} \frac{\partial^2 T^*}{\partial y^{*2}} + \frac{q'''_{l,0}}{\rho c_v \Delta T} {q^*}'''_{loss} + \frac{q'''_{core,0}}{\rho c_v \Delta T} {q^*}'''_{core} \qquad 4.22$$

$$\frac{1}{\tau} \frac{\partial T^*}{\partial t^*} + \Pi_{conv} w^* \frac{\partial T^*}{\partial y^*} = \Pi_{cond} \frac{\partial^2 T^*}{\partial y^{*2}} + \Pi_{loss} {q^*}'''_{loss} + \Pi_{core} {q^*}'''_{core} \qquad 4.23$$

$$\Pi_{conv} = \frac{w_0}{L_0} \qquad \Pi_{cond} = \frac{\alpha}{L_0^2} \qquad \Pi_i = \frac{q'''_{i,0}}{\rho c_v \Delta T}$$

4.1.0.2 Scaling of the Air Ingress Velocity

Air ingress into the lower plenum is of particular concern as it represents the initiation of experimental investigation. This ingress manifests as a density driven lock exchange flow (Cite).

The primary variables of interest are the expansion wave velocity of the cold air current, $\boldsymbol{u_{LP}}$, and the hot current velocity, $\boldsymbol{u_H}$.

Of these, $\boldsymbol{u_{LP}}$ is of significantly greater interest, as it is directly related with the ingress velocity of the cold air. Experimental results show that it may be expressed as

$$\boldsymbol{u_{LP} = 0.44\sqrt{\frac{gd(\rho_C - \rho_H)}{\rho_C}}} \qquad 4.24$$

However, Chang Oh also presents a time scale which is calculated as the ratio of duct length and superficial velocity. Lowe presents clear methods for calculation according to density ratios, and for the prototypical conditions expected, Oh predicts a time scale on the order of 19.5 seconds.

Both methods provide effective predictors of similitude according to design parameters – namely, duct length and height.

4.1.0.3 Scaling of the Heat Transfer Boundary Conditions

Previous scaling efforts examine local phenomena. While interesting, a bulk examination of facility performance would be very useful. To provide this, consider again a subchannel. One may reasonably assert, assuming sufficient insulation, that any heat transfer through the channel walls via conduction would be advected into the fluid under natural circulation. Explicitly,

$$\boldsymbol{q_{conv} = q_{adv}} \qquad 4.25a$$

$$\boldsymbol{-k\left.\frac{\partial T}{\partial x}\right|(x = 0) = \bar{h}\Delta T_{lm}} \qquad 4.25b$$

That is, over the subchannel length, the average heat transfer coefficient and log-mean temperature difference of the fluid within the subchannel are necessarily related to the temperature gradient across the channel wall.

This analysis a priori assumes an isothermal channel wall boundary condition. Given the thermal inertia associated with the prototype facility, this assumption seems reasonable.

From the simplification

$$-k\frac{\Delta T_w}{\Delta x} = \bar{h}\Delta T_{lm} \qquad 4.26$$

One finds

$$\frac{\bar{h}L}{k_s} = \frac{\Delta T_w}{\Delta T_{lm}}\frac{L}{\Delta x} \qquad 4.27a$$

$$Nu' = \Theta\Pi_{Geom} \qquad 4.27b$$

Thus, if a certain thermal response is desired, then it is necessary to achieve similitude between the modified Nusselt number and subchannel geometry. Furthermore, this provides a useful diagnostic tool in that measurement of the temperature gradient through the subchannel wall can provide insight into the convection going on at any given moment within the facility.

Based on these results, and considering those derived from the top-down analysis, it’s clear that the key parameters for this facility are going to be geometry and buoyant phenomena. Table 36 shows the scaling ratios produced through this analysis,

Table 18. Scaling ratios to be used for the SFSETF

Parameter	Prototype Value	Model Value	Scale
L_{HT} (m)	2.93	1.5	0.511945
q'' (W/m^2)	17817.9	17820	1.000118
Q (W)	39000000	4.40E+03	0.000113
d_h (mm)	15.69	15.75	1.003824
dT_{lm} (K)	560	550.0812184	0.982288
T_s	1250	600	0.48
T_out-T_in	360	184.322053	0.512006
T_s-T	580	600	1.034483

Additionally, when considering these bulk parameters, it bears noting that the diffusion coefficient is also temperature dependent. Thus, it was necessary to calculate the binary diffusion coefficient at the scaled temperatures presented in Table 36, the results of which are presented in Table 37. In this way, the reference Richardson number (the ratio between the value in the prototype and model facilities) may be considered with respect to the ratio of diffusive to convective forces at different temperatures.

However, that is not to say that it is necessary to maintain thermal similarity. Given that a binary gas mixture of helium and air is used, the diffusive potential is fundamentally altered in the model facility. Thus, if the ratio of diffusive and convective forces is to be maintained, it then follows that the bulk temperature of the facility should be adjusted accordingly. As the ratio of densimetric and diffusive phenomena are expected to drive the onset and establishment of natural circulation, the ratio between the two forces achieving unity in the reference value is critical to maintaining 1:1 temporal behavior.

Table 19. Diffusion parameter calculation for Richardson number evaluation

Temperature	T_{Mix} (K)	773	723	573	473	423	373
Lennard-Jones Parameters	σ_{He}	2.57					
	σ_{N2}	3.67					
	σ_{mix}	3.12					
From Tans. Phenom	Ω	0.66	0.65	0.68	0.70	0.71	0.72
	M_{He}	4.00					
	M_{N2}	28.01					
	ε/k_{He}	10.2					
	ε/k_{N2}	99.8					

	ε/kmix	31.90					
Reduced Temperature	T'Mix	24.23	22.66	17.96	14.83	13.26	11.69
Pressure	p(atm)	1					
Diffusion Parameter		3.30	3.04	2.07	1.51	1.25	1.02
		1	1.09	1.59	2.19	2.65	3.24
Surface Tenperature	Ts (K)	1000	950	800	700	650	600
Temp Ratio		227	227	227	227	227	227
		1	1	1	1	1	1
Length	L (m)	2.97	2.72	1.97	1.76	1.51	1.26
		1	1.09	1.5	1.6875	1.97	2.35
Ref Richardson Number	$\boldsymbol{Ri_R} = \frac{\boldsymbol{dT \times L}}{\boldsymbol{D^2}}$	1	1.10	1.35	1.00	1.09	1.25

Using the information obtained in Table 37, one may conclude that it may indeed be possible to achieve similarity between the buoyant and diffusive forces at a reduced temperature and length. This is desirable, as it significantly reduces the logistical burden associated with construction of this facility.

4.1.1 Physical Overview

The following sections provide a comprehensive overview of the experimental facility, the SFSETF. The SFSETF comprises three vessels, as shown in Figure 33: The vertical standpipe (VS) to simulate the reactor containment volume, the cross duct connecting it to the next vessel, the primary pressure vessel, which is meant to simulate the reactor vessel.

Primary Pressure Vessel

The PPV shell consists of three flanged sections: The lower plenum shell, the cylindrical shell, and the upper plenum shell. The body shell features an internal diameter 12.39”, and made from 12” schedule 10 pipe, which features a wall thickness of 0.180”, and is constructed from 316L Stainless Steel (SS). Complete materials data is captured in the Harris Thermal Engineering Transfer, which can be made available upon request.

Both the upper and lower plena shells are machined from 304 SS, and have an outer diameter of 16”. They are connected to the body shell via fillet welded body flanges, inner diameter of 12.75”, which is welded to the exterior of the body shell. The lower plena shell is unique in that it features two penetrations: One penetration is horizontal, while the other inserts vertically. This is done to preserve access geometry (how the ingressing plume approaches the lower plenum) as a parameter of investigation. The vertical insertion is formed via a 90^{o} elbow made from 4” schedule 40S made of 304 SS.

The primary pressure vessel features four (4) penetrations on the upper and lower plena shells (and corresponding body flanges) limiting the applicable torque to the sealing flanges. The PPV also features numerous ½” NPTF penetrations to accommodate extensive instrumentation configurations, routing paths, and cluster arrangements, as well as a supported penetration on the top plenum cover plate, which is customized to support gas chromatography instrumentation. The support is fillet welded over a 1.5” penetration, and extends 8 3/8” beyond the exterior of the top plenum over plate.

A note: A custom machined coupling (measuring 20” in length) was constructed from 6061 aluminum to provide additional instrumentation support at the upper plenum cover plate, where the GC instrument is primarily located.

SFSETF Core Region

The core region resides within the PPV. The core consists of the following components: SS coolant channels, upper and lower baffle plates, tie rods, and heater rods. The core bundle that these components form is wrapped in fiberglass insulation, and secured with sheet metal; the interstitial space between the bundle and body shell forms the downcomer. The central cavity is also filled with fiberglass insulation so as to provide a more uniform radial temperature profile during operation.

Figure 35 shows a top-down view of the core configuration, which is meant to simulate a prismatic configuration.

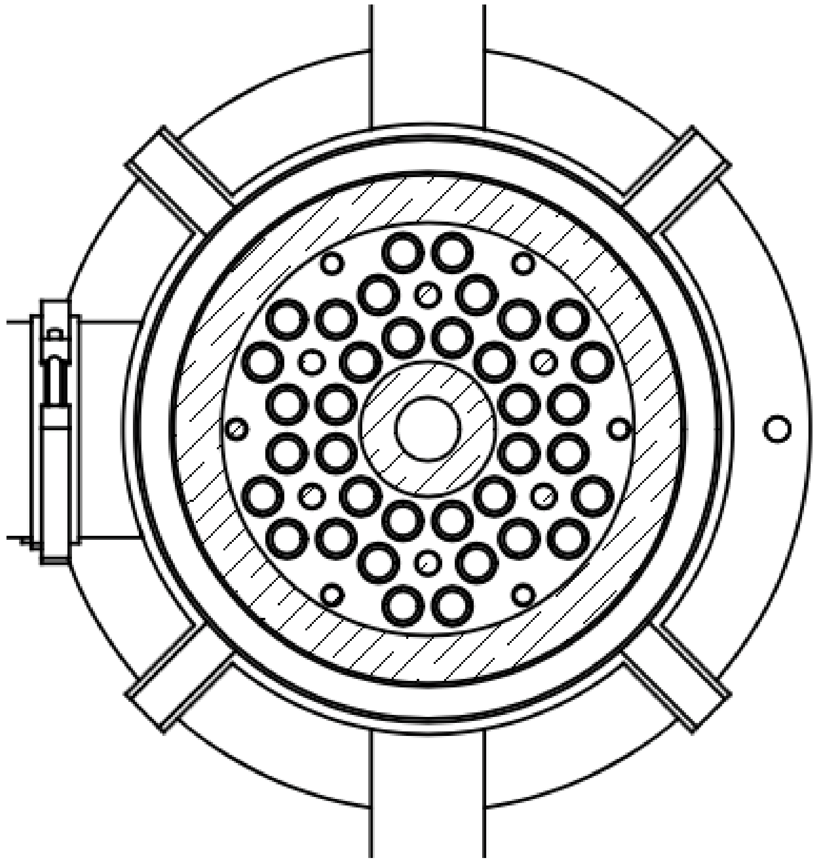

Figure 35. Top-down view of the SFSETF core configuration.

In order to support system control, and with limited intent towards non-dimensional factor calculation, one coolant channel was selected to be the Instrumented Coolant Channel (ICC). The ICC features two (2) penetrations to permit thermocouple installation.

The interstitial volume between the coolant channels will be backfilled with helium, deviating from the ceramic core blocks utilized in the reference design, as well as the HTTF. While this distorts the radial temperature profile across the core region (meaning that it deviates from the projected values and/or ratios of the HTTF and other Integral Effects Test Facilities (IETFs)), this is considered acceptable as radial temperature distribution is not expected to have a strong influence on plena transfer up to and including ONC.

Additionally, an astute observer might notice the lack of radial and axial reflectors. These function similar to neutron reflectors, in that they serve to limit the heat flux escaping the interior core blocks. This becomes of particular note to maintain similarity with bypass flow, and other integral effects. As this facility is in no way concerned about these effects, such additional material is happily neglected. However, separation between the upcomer is provided via 1.5” of fiberglass insulation and mechanically held via steel cladding.

Electricity provides heating via OMEGA Engineering STRI-7245/120 cartridge heaters. As standard cartridge heaters, they are straight, cylindrical immersion heaters, featuring a 0.475” OD, Incoloy 800 cladding, 120V AC input, and a maximum sheath temperature of 870C. This limit is monitored via the ICC. Specifically, externally mounted thermocouples on the ICC permit inference into the maximum sheath temperature experienced during operation, and procedures are written (or shall be written) so as to preclude exceeding this operational limit.

Referring to Figure 36, one may see the heater rods arranged in the core configuration as the smaller diameter baffle plate penetrations. Leads to the heater rods are protected by alumina tubes. Figure 37 provides an axial cutaway, showing instrumentation clusters in the upper and lower plenum, as well as the ICC.

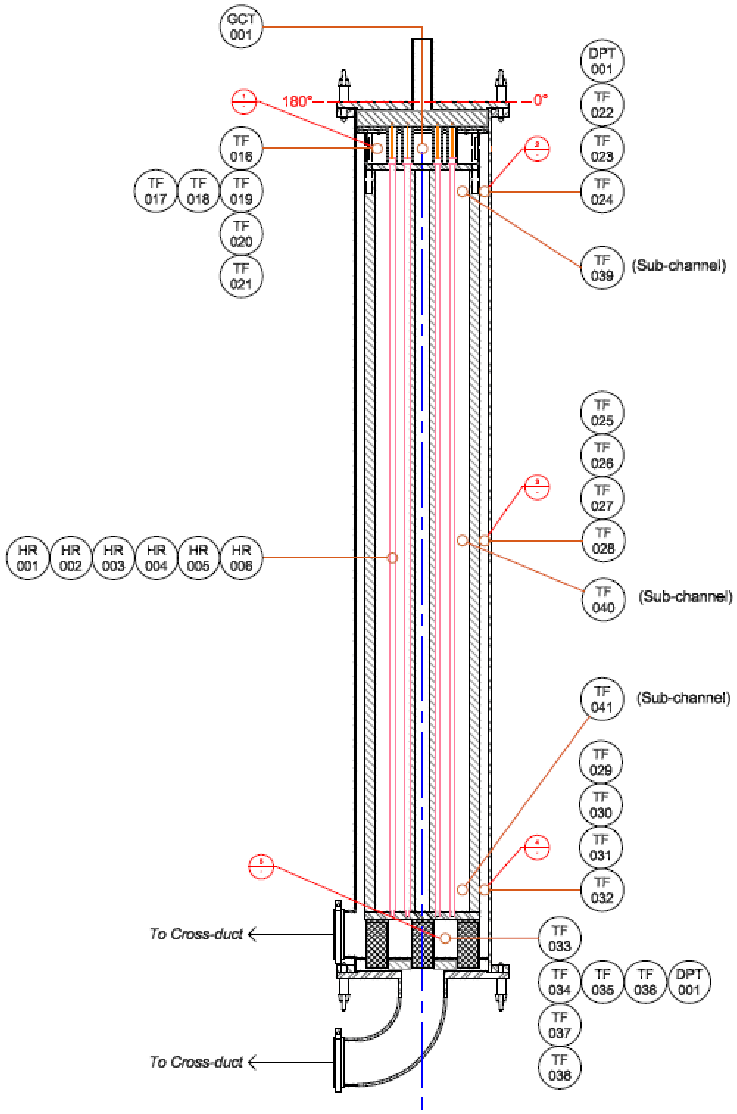

Figure 36. PPV instrumentation diagram, axial cut away view

Cross Duct

The SFSETF features a cross duct that couples to the VS and the PPV via flanged connections. This deviates from the concentric inlet/outlet ducts of other IETFs. This deviation is acceptable, as the simplified geometry does not impede or distort heat and mass transfer between the plena prior to GFC onset.

Made from 304 SS, the cross duct, like the elbow, is constructed from 4” schedule 40S piping, and features a 0.219” wall thickness, and is fillet welded to a V-band clamp which provides a secure connection at the PPV penetration(s).

The cross duct may be relocated from the “HIGH,” or horizontal ingress position, to the “LOW,” or vertical ingress position. Bidirectional flow is expected within the cross duct at all points during active experimentation, and therefore the cross duct features several ports to install appropriate instrumentation, including the 1½” IPS pipe and port that forms the gas chromatography instrument support. This is shown clearly in Figure 37, as GCT 001, which also shows the flow switch insertion points (FSL 001/002), the pressure transducer (PT 002), a thermocouple (FT 001), and the 4” ball valve (BV 001).

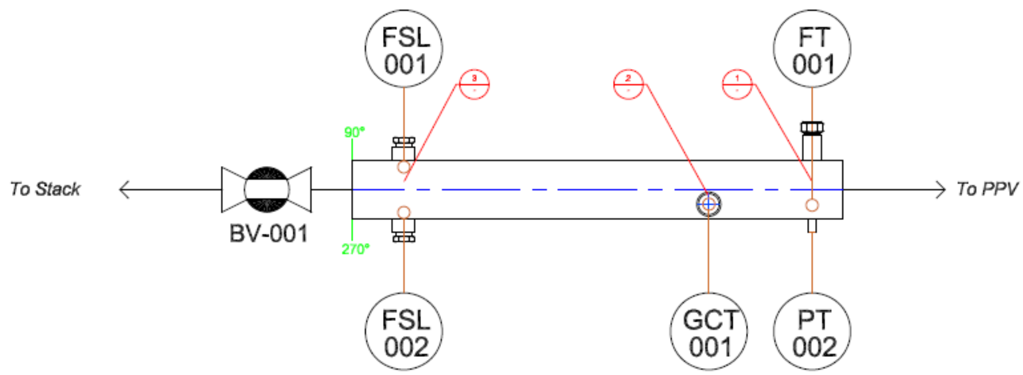

Figure 37. Cross duct instrumentation diagram

Duct length was selected by the length necessary to eliminate or preclude microscale phenomena of the flow. Specifically, a flow conditioner, the VorTab Insertion Plate, is necessary to eliminate any vorticity or eddy effects in the ingressing plume front. Additionally, nine (9) nominal diameters are required for full effect; for a four (4) inch pipe, that becomes a 36” process length.

Vertical Standpipe

The vertical standpipe (VS) is, as the name implies, a vertically oriented right circular cylinder, constructed of 304 SS 6” schedule STD pipe. It measures approximately 96” in length, and is supported by an aluminum structure which also features as the mounting location for local process switches and equipment.

Meant to simulate the reactor cavity in the reference facility, and analogous to the Reactor Cavity Simulation Tank (RCST) in the HTTF, its only purpose is to hold the ingressing fluid, and to serve as the second reservoir in thermodynamic contact with the PPV.

This limited application also drives the instrumentation selection surrounding the vessel. The VS instrumentation serves to provide data sufficient to determine or calculate initial state properties. As shown in Figure 38, this objective is achieved via thermocouple clusters at the along the VS, as well as an absolute pressure transducer located near the vessel bottom. One may initially assume no presence of helium, but beyond initial conditions, VS mass fraction of helium is of limited interest to the current experimental program. These factors may lead a designer to conclude that minimal instrumentation, sufficient to infer initial state properties, is necessary. Further instrumentation may be installed to infer fluid behavior as the experimental program progresses.

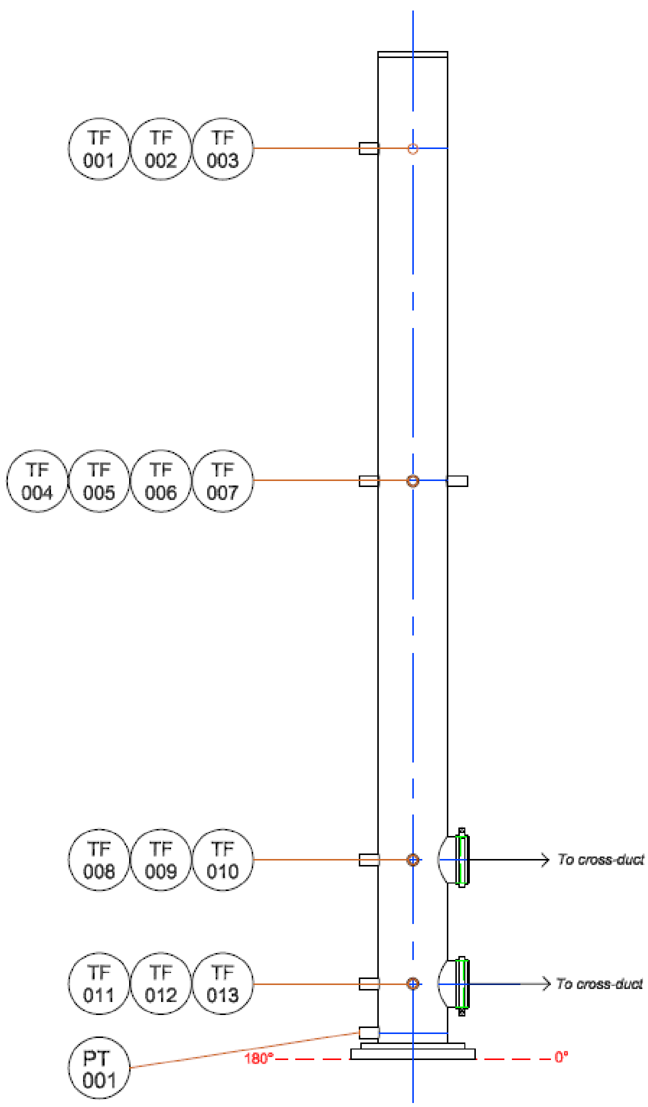

Figure 38. Vertical standpipe instrumentation diagram

4.1.2 Instrumentation Requirements

To support this experimental program, instrumentation requirements were identified, with priority being given to modularity and availability, as shown in Table 17.

Table 20. Instrumentation requirements and supporting bases.

Requirement	*Basis*
Sampling rate > 100 Hz	Bounding velocity calculations to determine Nyquist frequency, safety factor of 20 applied.
Transmit on 4-20 mA	Maintain consistency of signal type and magnitude to streamline DACS design and construction.
Modularity	The SFSETF will accommodate future experimental efforts; therefore, adaptability to new experimental objectives is of significant interest.
No custom parts or sensors	Custom parts and sensors usually experience significant delays in installation due to their iterative development cycle, standard parts will streamline instrumentation installation and commissioning.

The flow parameters of interest and location are presented in Table 18. These include sufficient parameters to clearly define the state of the fluid.

Table 21. Interrogative methods used to inform instrumentation selection in the SFSETF.

Parameter	*Interrogation Method*	*Basis (if applicable)*
Temperature	Thermocouples[2]	State property
Velocity	Thermal dispersion flow meter	Convection diagnosis
Pressure	Absolute, differential	State property

[2] Instrument uncertainty should be considered.

Direction	Thermal flow switch	Convection diagnosis
Composition	Oxygen sensor[3]	State property, convection diagnosis

From these requirements, a prospective instrumentation system was examined and developed. These key evaluation criteria, as well as initial cost estimates, are collected and presented in Tables 19 and 20.

Table 22. Components and equipment list to construct the SFSETF DACS

Component	*Description*	*Supplier*	*Qty.*	*Unit cost*
Controller and Chassis	CompactRio (Model NI cRIO-9068) *Chassis Slots:* 8 *OS:* NI Linux Real Time *Design Software:* LabVIEW Real-Time *Processor:* 667 MHz Dual-Core ARM Cortex-A9 *FPGA:* Atrix-7 *Memory:* 512 MB DDR3 *Non-volatile storage:* 1 GB *Ports: 1 USB, 2 Gigabit Ethernet, 3 serial ports*	National Instruments	1	$3,999.00

[3] Use of ambient air was authorized, as the prismatic core configuration was achieved with steel rather than graphite.

	CompactRio Power supply (Model NI PS-15) *Input:* 1-phase 115/230 VAC *Output:* 24 to 28 VDC, 5 A	National Instruments	1	$221.00
	CompactRio Panel mounting kit	National Instruments	1	$63.00
Data Acquisition Modules	Thermocouple module (Model NI 9213) Built-in Cold-Junction-Compensation *Channels:* 16 *Voltage Output:* $\pm\mathbf{78}$ mV *Resolution:* 24-bit *Sensitivity:* Up to 0.02 ℃ *Speed:* 1,200 S/s (aggregate)	National Instruments	3	$1,185.00

	Current Input (Model NI 9208) *Channels:* 16 *Current Output:* $\pm\mathbf{21.5}$ mA *Resolution:* 24-bit *Speed:* 500 S/s (aggregate) *Connector: 37-pin D-Sub*	National Instruments	1	$603.00
	Terminal Block (Model NI 9923) For current input module.	National Instruments	1	$135.00
Control Modules	Current Output (Model NI 9265) *Channels:* 4 *Current Input:* 0 to 20 mA *Resolution:* 16-bit *Speed:* 100 kS/s (per channel)	National Instruments	1	$384.00

	Strain Relief Connector (Model NI 9927) For current output module.	National Instruments	1	$30.00
			Total:	$8,990.00 (w/ TC)

Table 23. Sensors and transduces equipment list to construct the SFSETF DACS

Component	Description	Supplier	Qty.	Unit cost
Thermocouple	(Model No. KQSS-M30G-300) K-type Grounded hot junction ALOMEGA (Ni-Al) Standard connector *Sheath:* 304 SS *Diameter:* 3 mm *Length:* 300 mm *Range:* -200 to 1250 ℃ *Uncertainty:* 2.2 ℃ or 0.75%	OMEGA Engineering Inc.	40	$26.00

	Response time: UNLISTED *Temperature limit of connector body:* 220 ℃			
Absolute pressure transducer	(Model No. PX409-030AI) Absolute *Process fitting:* ¼ NPT (Male) *Connector:* Cable termination *Output signal:* 4 to 21 mA *Range:* 0 to 2.1 Bar *Accuracy:* 0.08% (BSL linearity, hysteresis and repeatability combined) *Temperature compensation*: -29 to 85℃ *Thermal accuracy:* $\pm$ 0.50% (Zero Shift) $\pm$ 0.50% (Span Shift) *Response time:* <1ms	OMEGA Engineering Inc.	2	$510.00
Differential pressure transducer	(Model No. PX409-050DWUI)	OMEGA Engineering Inc.	1	$775.00

	Differential Wet/Wet *Process fitting:* ¼ NPT (Male) *Connector:* Cable termination *Output signal:* 4 to 21 mA *Range:* 0 to 3.5 bar *Accuracy:* 0.08% (BSL linearity, hysteresis and repeatability combined) *Temperature compensation*: -29 to 85℃ *Thermal accuracy:* ± 0.50% (Zero Shift) ± 0.50% (Span Shift) *Response time:* < 1ms			
Mass flow meter	(Model No. ST51) *Thermal accuracy:* ± 0.50% (Zero Shift) ± 0.50% (Span Shift)	Fluid Components International LLC	1	$2,416.00

	Response time: < 1ms			
Oxygen analyzer	(Model No. 300TB) *Bulkhead mounted, trace oxygen analyzer* *Insta-Trace B2C Sensor* *Range:* 0-10ppm to 10,000ppm *Output Signal:* 0-1VDC and 4-20mADC *Power Supply:* 85-240VAC	Teledyne Analytical Instruments	1	$15,150.00
			Total:	$20,401.00 (w/ TC)

Of particular note is the oxygen analyzer, the Teledyne 9060H Oxygen Analyzer Probe, which represents the greatest single expenditure on an instrument in this program.

Table 21 quantifies the instrumentation channels the constructed DACS will provide.

Table 24. Quantification of instrument channel types in the OSU SFSETF

Channel Type	Number of Channels
Thermocouple Channels	48

4-20 mA Analog Input	28
4-20 mA Analog Output	4
10VDC Digital Input	1
10VDC Digital Output	0

4.2 Design Stage Uncertainty Analysis

To determine the adequacy of this system, and its constituent sensors and transducers, a design stage uncertainty analysis was conducted. In particular, it is of significant interest to determine the 95% confidence interval associated with state property sensors. Key design decisions will also be presented, and discussed as appropriate.

4.2.1 Implementation of Multiple (3) E-Type Thermocouple and the Uncertainty of Several Identical Sets of Instruments

Clusters of three (3) thermocouples will be utilized wherever possible, rather than singular thermocouples, to reduce the overall uncertainty associated with that measurement. The purpose of this section is to outline why this strategy is implemented, and to calculate its effect on the confidence of the necessary measurements to be made in this facility.

Consider first the residuals associated with a small set of $\boldsymbol{N}$ measurements, for which the mean $\boldsymbol{\bar{X}}$ has been calculated. Their sum is the precision index, S.

$$\boldsymbol{S} = \sqrt{\frac{\mathbf{1}}{\boldsymbol{N}-\mathbf{1}}\sum_{i}^{N}(\boldsymbol{X_i}-\boldsymbol{\bar{X}})^{\mathbf{2}}} \qquad 4.28$$

While it has been well established that $\boldsymbol{N}-\mathbf{1}$ represents the degrees of freedom associated with this particular measurement, it is restated here so as to reinforce the importance of utilizing the correct statistical model. Referring to the Student's t-table, one finds that for 3 thermocouples ($\boldsymbol{\nu}=\mathbf{2}$), the 95% confidence interval factor is 4.303. This should be compared to the normal distribution's 99% confidence interval given by 3σ. Such is the cost of imperfect knowledge of the true standard deviation of a population.

There will be 4 bundles of thermocouples within the upper and lower plenum; therefore, it is of significant interest to determine the effects of this grouping, as 4.303C threatens to render the measurement unusable.

Statement: 4 sets of 3 E-type thermocouples are to be used both in the upper and lower plenum. Calculate an overall value of the mean, and provide the 95% confidence interval associated with that measurement.

The general mean may be calculated by the following expression

$$\bar{\bar{X}} = \frac{\sum_i^M N_i\left(\bar{X}_i - \bar{\bar{X}}\right)^2}{\sum_i^M N_i} = \frac{1}{4\cdot 3}\sum_i^{4\cdot 3} X_i \qquad 4.29$$

For several (4) sets of small N (3), the precision index of the mean is given by the weighted average of the precision indices, which are of course weighted by the individual degrees of freedom, such that

$$\bar{\bar{S}}_N = \sqrt{\frac{\sum_i^M \nu_i S_i^2}{\sum_i^M \nu_i}} = \sqrt{\frac{1}{M}\sum_i^M S_i^2} \qquad 4.30$$

This reduces the precision index by a factor of 3.46 ($\sqrt{12}$); therefore this instrumentation scheme is of significant value to the plena estimates of temperature, which are then characterized by a confidence interval such that

$$\bar{\bar{X}} \pm \frac{t_{MN-M,p}\bar{\bar{S}}}{\sqrt{MN}} \qquad 4.31$$

The maximum residual that may be calculated for any grouping of thermocouples is given by maximizing the precision error to 1.0C, giving a conservative value of $S_i = 1.22C$. For 4 groups of thermocouples, assuming each has a maximized residual,

$$\bar{\bar{S}}_N = \sqrt{\frac{\mathbf{5}}{\mathbf{12}} \cdot (\mathbf{1.22^o\ C})^2} = \mathbf{0.791^o C} \qquad 4.32$$

The t-statistic for this grouping should be calculated, as shown in Equation 4.21, with $\boldsymbol{MN - M}$ degrees of freedom, due to the fact that M parameters must be estimated, in the form of the residuals. This, however, leaves 8 degrees of freedom (very similar to the number outlined above!) with which to estimate the true mean. Referring to the Student's t-table shows that for a 95% confidence interval, one finds the value as 2.306. Or, more precisely, the most conservative estimate of the uncertainty of a steady plena temperature measurement is given by

$$\boldsymbol{X} \pm \left(\mathbf{2.306} * \frac{\mathbf{0.791^o C}}{\sqrt{\mathbf{12}}}\right), \boldsymbol{p} = \mathbf{95}\% \qquad 4.33$$

$$\boldsymbol{X} \pm \mathbf{0.526^o C}, \boldsymbol{p} = \mathbf{95}\% \qquad 4.34$$

This is excellent, and is an acceptable amount of uncertainty. It also is a significantly better estimate than a single thermocouple may provide. A brief note: Standard limits of E-type thermocouples are 1.7C, but the special limits (1.0C) are implemented because they were:

1. Verified within that tolerance.

2. These instruments were ordered in advance to comply with the special tolerance limits [34].

4.2.2 Uncertainty Associated with Hydraulic Diameter

While the details of length and diameter measurement will be best left for another report, it is worth mentioning that measurement of the hydraulic diameter is of significant importance. It was measured both at the inlet and outlet a minimum of eight times, as shown in Table 7, which allows this analysis to claim credit for multiple sets of data when evaluating the uncertainty of this measurement.

Specifically, with 2 sets of 8 measurements, the relevant degrees of freedom are 14, and the associated 95% confidence interval can be calculated to be $\pm\mathbf{0.0522}\ \boldsymbol{mm}$, or 0.332%. The methodology is similar to that outlined above, and will therefore be left as an exercise to the devoted reader.

4.2.3 Uncertainty Associated with a Single Bank of Thermocouples

It was known early in this work that several banks of thermocouples would not always be usable, due to the constraints placed on the hydraulic diameter of the coolant subchannels (15mm). However, it was decided that instrumentation should be included within the subchannels as an indicator of experimental progression. This section will examine the utility of these thermocouples, as they will occur at a minimum of three (3) different locations along the instrumented coolant subchannel.

To achieve any reasonable statistical information, 3 thermocouples will be routed into place. Using a similar process to that outlined above, the residuals are maximized and added in quadrature, yielding $\boldsymbol{S = 1.22C}$.

Therefore, a conservative estimate of the 95% confidence interval is given by

$$\boldsymbol{X \pm 4.303 * 1.22^{o}C = X \pm 5.25^{o}C, p = 95}\% \qquad 4.35$$

For the sake of clarity, this work will now consider the use of a single thermocouple, with a verified uncertainty of $\leq \boldsymbol{1.0C}$, as this methodology will become important later in this analysis. Due to this knowledge of the uncertainty, this work may claim a KNOWN standard deviation of $\boldsymbol{2} \cdot \boldsymbol{R}$, where $\boldsymbol{R}$ represents the maximum range possible for that particular instrument. Under these circumstances, the confidence interval is formulated by assuming that measurements conform to a known normal distribution, thus allowing the use of the z statistic such that

$$\boldsymbol{X \pm \frac{z\sigma}{\sqrt{N}} = \frac{2.0C * 1.96}{\sqrt{1}} = 3.98C, p = 95}\% \qquad 4.36$$

While this gives a better estimate of the confidence interval, the author would like to state that banks of thermocouples are preferable in this experiment, as they provide defensible, statistical data rather than relying on a heuristic formulation associated with a singular thermocouple.

4.2.4 Uncertainty Estimation of ST-100 Flow Meter

The ST-100 flow meter is a thermal dispersion mass flow meter. While a full overview of the theory and operation of this instrument is beyond the scope of this document, the goal of this section is to describe, estimate, and calculate the uncertainty associated with this particular instrument. Further, it is imperative to relate that uncertainty to that of the Reynolds number.

However, consider a brief description of the theory of operation from the operation manual [35], in lieu of a more thorough treatment for the purposes of this analysis. In point of note, these are an industrial standard instrument, and therefore have received rigorous treatment by the American Society of Mechanical Engineers [36]

The instrument is essentially a probe that is inserted into a fluidic medium, usually a gas. The probe contains a flow shield, a low powered heater element, and two resistance temperature detectors. It connects to a flow conduit via a 1” or 1.25” NPT connection. The heater element produces a thermal differential between the two RTDs, by heating one above the process temperature. This differential changes proportionally with respect to mass flow, which is converted to a transmittable signal via some transfer protocol, usually HART. The unheated RTD provides the process temperature value.

As part of the procurement process, it was requested that the instrument be calibrated by the manufacturer and that they provide a calibration certificate. While this was certainly provided there is some confusion regarding the values provided. The specifications data available for the instrument cites an accuracy of 0.75% of reading, and repeatability of 0.5% of reading [35]. Added in quadrature, this produces a total expected error of 0.901% of reading. However, upon inspection of the calibration certificate, one notices certain points of interest, specifically:

1. Gaseous equivalence between 100% air and 50% helium and 50% air is stated but the criteria for equivalence is neither established nor discussed.

2. Comparison measurements are provided for the instrument against a “Desired SFPS Per Stand,” along with an actual percent reading difference and an allowed percent reading difference. However, this doesn’t necessarily correspond to known values for these flow rates by any indication on the calibration certificate.

3. The % reading differences, if taken as errors, are outside the 0.901% maximum expected error. Moreover, the % differences do not correspond to percent differences between the “Desired” stand and the “Model.”

4. There is an “Allowed % Reading Difference” column that does not correspond to any known criteria.

5. There is no description of the calibration methodology.

6. On page 2, a table is provided that relates several parameters, but the sources of these values isn't discussed in any detail, calling into question exactly how they relate to the instrument's calibration.

In the absence of any further information, this work will treat this instrument as a singular reading, as the thermocouple example outlined previously. Utilizing the maximum gross uncertainty over the calibration range, 1.25% of reading at 5.004 surface feet per second (SFPS) yields a gross uncertainty of 0.063 SFPS.

With a maximum range of 0.1251 SFPS as an assumed KNOWN standard deviation, then the confidence interval for a singular point measurement is given by

$$\boldsymbol{X \pm 1.96 \cdot 0.125\, SFPS \rightarrow X \pm 0.245\, SFPS} \qquad 4.37$$

It may be seen in contemporary works that velocity jumps on the order of <1.0 m/s may be expected [37] [18] [38]. Therefore, one may see that, in experimental application, this may be of limited utility to determine ONC; however, useful interrogation of bulk flow may still be possible under such uncertainties. However, upon deployment of this instrument, several operational concerns were noted, eventually leading to the decommissioning and removal of the instrument from the facility.

4.2.5 Uncertainty Associated with the Data Acquisition System

In addition to the instrument uncertainties provided and discussed above, there is another potential source of error – the DAQ module. It then remains to evaluate its contributions to overall system uncertainty.

The greatest single contributor to DAQ contribution of uncertainty is the analog-to-digital conversion (ADC); however, blessed technological progression has made even this quantity relatively small. The amount of error introduced by this is a function of the resolution of the ADC device and the range of the signal. Specifically,

1. NI 9213 Thermocouple Module

$$\epsilon_{quant} = \boldsymbol{16 \cdot \left(\frac{21.5mA}{2^{24}}\right) = 0.0205}\% \qquad 4.38$$

2. NI 9208 Current Input Module

$$\boldsymbol{\epsilon_{quant}} = \mathbf{16} \cdot \left(\frac{\mathbf{21.5}\boldsymbol{mA}}{\mathbf{2^{24}}}\right) = \mathbf{0.0205}\% \qquad 4.39$$

Assuming no further elemental sources of error, one may apply a universal quantization error on all ADC modules, and incorporate this into the general uncertainty analysis; however it functionally only applies to the Reynolds number, and negligibly so at that.

Table 22 provides magnitudes, uncertainties, and references of these parameters where necessary.

Table 25. Uncertainty magnitude and references to evaluate the Reynolds and Grashof numbers

Parameter	*Uncertainty (to 95% Confidence where applicable, % Scale unless otherwise noted)*
Velocity	0.245 SFPS (4.90%)
Temperature DIfferential†	0.744C (0.298%)
Hydraulic Diameter	0.332%
Quantization	0.00205%

†The temperature differential uncertainty is calculated by adding the upper and lower plenum temperature uncertainties in quadrature

From this, one may see that uncertainty is dominated by velocity uncertainties, as well as other experimental contributions in the form of flow field properties.

4.2.6 Data Acquisition and Control System

The SFSETF is instrumented for steady-state and transient operation. The number, type, and uncertainty of the installed instrumentation is sufficient for the experimental program outlined in the *SFSETF Instrumentation Report* [39]. But, the SFSETF will initially be configured to handle the instrumentation channels outlined in Table 23.

Table 26. Quantification of instrument channel types in the OSU SFSETF

Channel Type	Number of Channels
Thermocouple Channels	48
4-20 mA Analog Input	28
4-20 mA Analog Output	4
10VDC Digital Output	0

Control of the SFSETF will be implemented through LabView software to seamlessly integrate data acquisition and facility control through one platform. The facility operator will utilize an on-site terminal that is directly connected to the primary I&C panel, via S-cable or Ethernet connection. This terminal will also be connected to the cRIO chassis, which hosts a local RT processor and an FPGA. These two components allow a significant amount of operational flexibility; however, they are primarily implemented in lieu of additional signal conditioning, such as pre-amplification, multiplexing, etc., as these are sources of experimental uncertainty and signal noise.

Figure 39 outlines the facility configuration of the SFSETF Data acquisition and Control (DAC) system. It highlights the wiring paths from the SFSETF, to the panel, which then relays process data to the terminal. All data collected during a test will be stored both on the local terminal, and on a remote server which is secure and routinely backed up, in order to provide diverse and redundant storage volumes for process data.

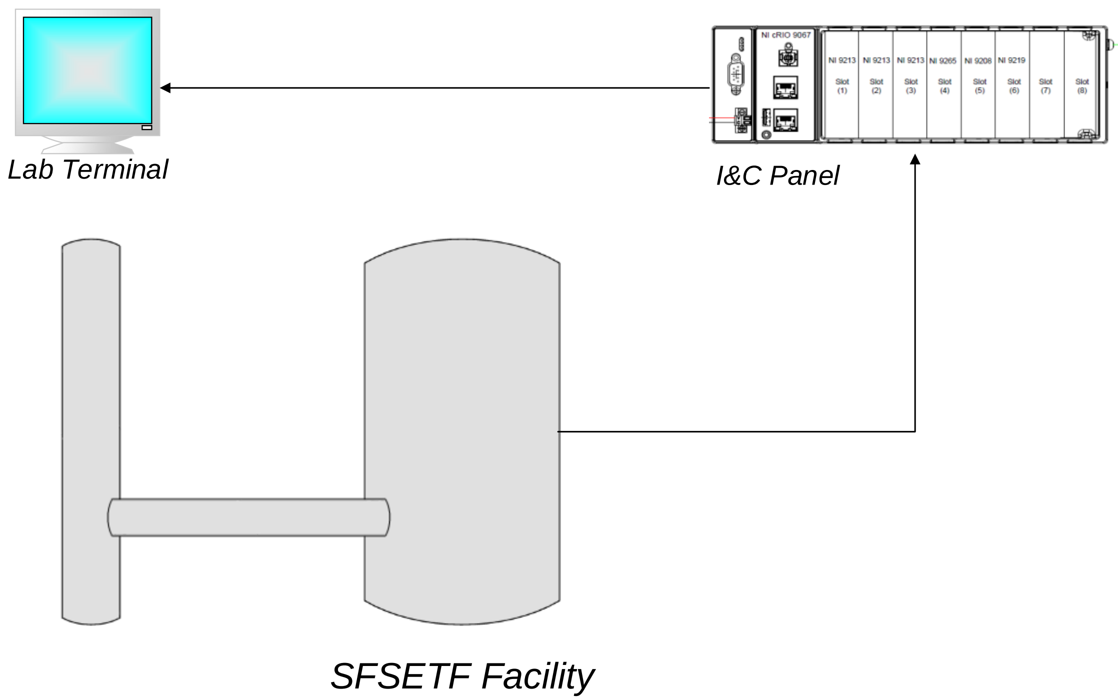

Figure 39. SFSETF instrumentation and control configuration, including I&C panel and lab-space terminal

The LabView software which hosts the SFSETF DAC System is executed by three Virtual Instruments (VIs) which are hosted by three separate pieces of hardware. The first component, the FPGA controller, interfaces with National Instruments (NI) modules which are installed on the cRIO chassis. The FPGA controller runs the FPGA VI, which utilizes an operation mode called the ‘scan interface’.

This interface creates an image of all measurement channels at a specified frequency, and stores that image into the memory of the second hardware component, the real-time processor on board the cRIO hardware. This processor is connected to the FPGA hardware via a PCI bus, which provides extremely fast and reliable data transfer between the two components. The RT processor runs the RT Host VI, which processes the data into separate channels, and buffers a data stream which is sent out to any number of destinations. The RT Host VI also accepts commands from connected clients, which it then processes and sends to the FPGA for deployment to the facility hardware. The control PC runs the Control Station VI, which collects measurement data for processing, writes the data to a hard disk, and provides an interface for user control of the facility via commands sent to the RT Host VI.

The RT processor and FPGA hardware essentially function as one unit, with incoming and outgoing data being processed by the RT processor and all hardware communication being handled by the FPGA controller. This greatly simplifies the development process for the LabView system, because the scan interface allows for the RT Host VI and the FPGA VI to have direct access to each other, and for the data acquisition function of the hardware to be deterministic within the cRIO environment. All non-deterministic communication, such as network queries, disk writing, or USB data transfer, are implemented using a data buffer to protect the core data acquisition process from being exposed to unexpected delays. If the control PC were to be disconnected from the cRIO in the middle of a test, then this configuration would allow for the data stream to be paused and continued without affecting the integrity of the collected data.

The limitations of the scan interface are worth considering, with the primary drawback being a reduction in the sample frequency of the hardware, since the FPGA is executing a generic program to simply capture all the incoming data in a single image. If a sample rate above 200 Hz is required at a later point in development of the facility, a hybrid mode can be used, which allows some NI modules to run custom FPGA VIs, while the remainder utilize the scan interface. This hybrid operational configuration would still utilize the RT Host VI for control of data input and output to the system, but would require custom FPGA related programming to achieve the higher sample rate required.

4.2.7 Piping and Instrumentation Diagrams, Wiring Diagrams

The following section provides the piping and instrumentation diagrams (P&IDs) used to route instrumentation and build the DACS so as to comply with the requirements highlighted above.It also provides graphical presentation of where instrumentation is placed within the facility.

Primary Pressure Vessel

The PPV P&ID is shown in Figures 40 and 41, which provides detailed views and instrument identification numbers that may be connected to the SFSETF termination schedule for complete traceability.

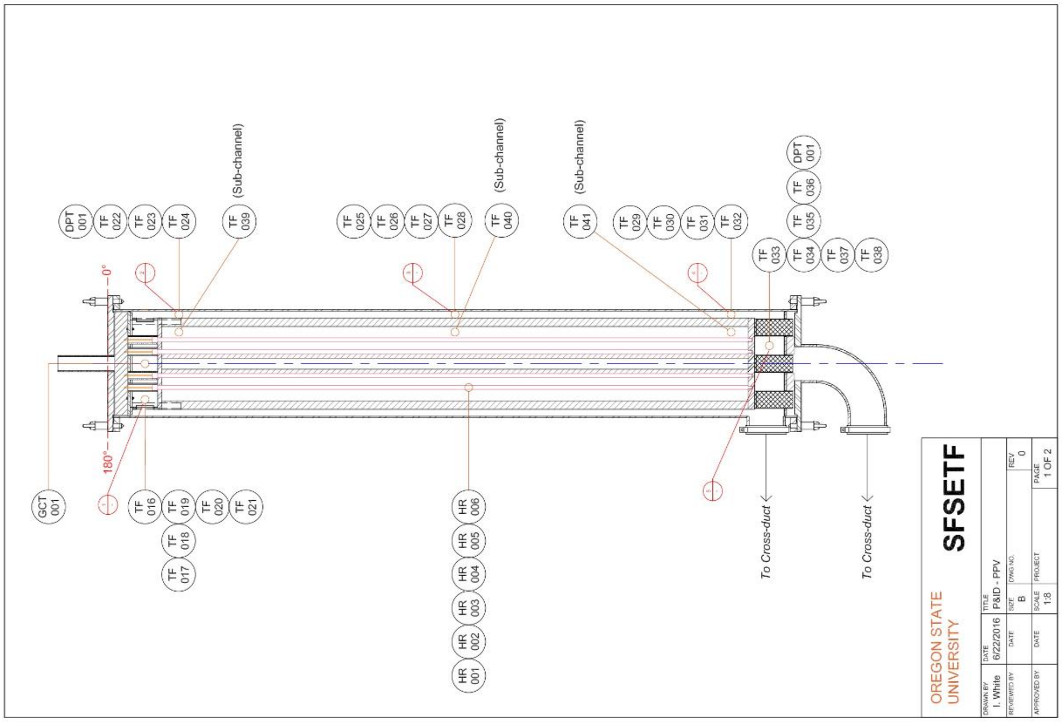

Figure 40. PPV axial view, showing instrumentation ports and identification numbers for the PPV.

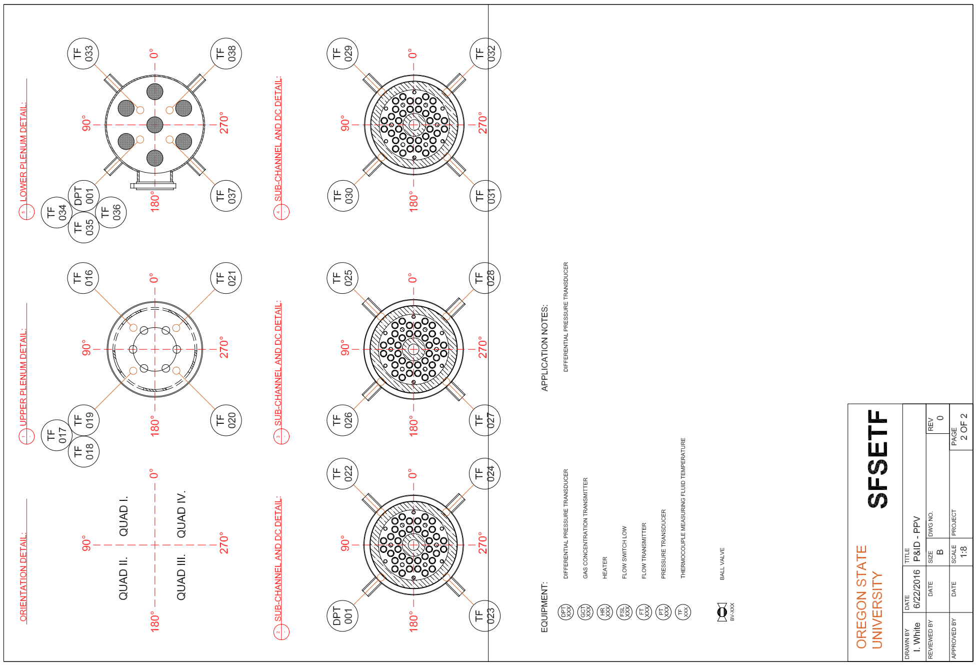

Figure 41. PPV top-down, detail view, showing instrumentation routes and identification numbers for the PPV.

4.2.8 Vertical Standpipe

The VS P&ID is shown in Figures 42 and 43, which provides detailed views and instrument identification numbers that may be connected to the SFSETF termination schedule for complete traceability.

Figure 42. VS P&ID, showing instrumentation ports and identification numbers.

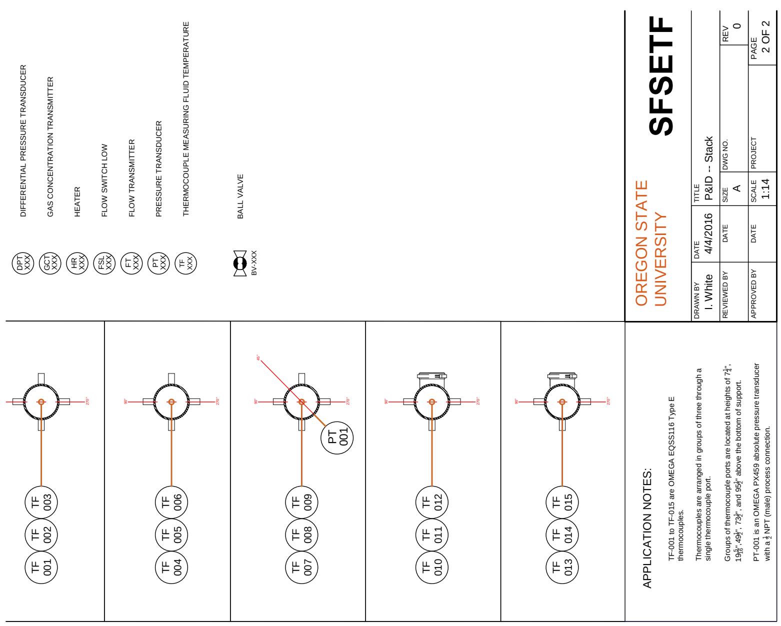

Figure 43. VS P&ID, showing instrumentation ports and identification numbers.

4.2.9 Cross Duct

The cross duct P&ID is shown in Figure 44, which provides detailed views and instrument identification numbers that may be connected to the SFSETF termination schedule for complete traceability.

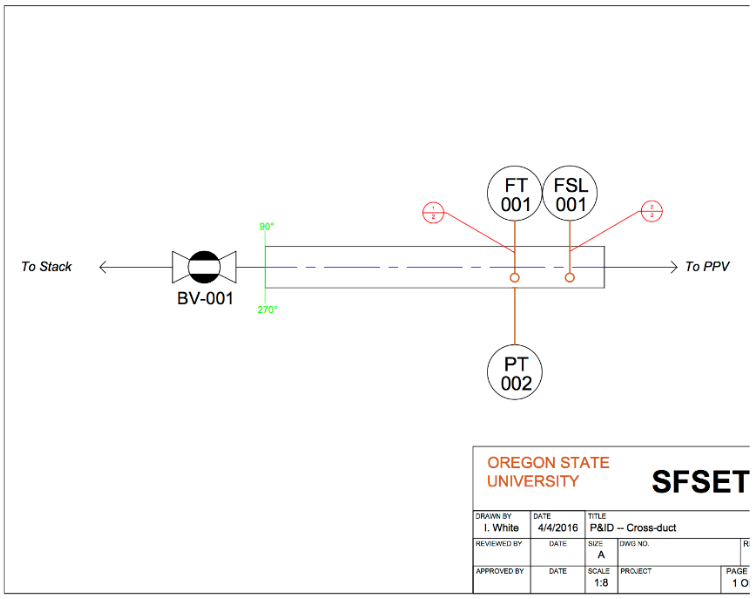

Figure 44. P&ID showing a side view of the cross duct, as well as instrumentation ports and identification numbers.

The termination schedule preserves traceability of all deployed instruments from installation location to channel number in the cRIO. Red shaded cells indicate instrument failure. Notes are presented in order to capture re-assignment of the instrument identification number after instruments were abandoned in place.

4.3 Shakedown Testing Plan

Shakedown testing was an integral part of qualifying the SFSETF for use in an experimental program. The objectives of shakedown testing are stated as follows:

i. Verify the design characteristics of facility.

ii. Verify the functionality of the instruments and their calibration.

iii. Verify the functionality and adequacy of process control systems.

iv. Verify the functionality and adequacy of safety set-points and interlocks.

v. Characterize the differential pressure, heat losses, facility thermal performance, and component performance under steady-state conditions.

vi. Develop operational procedures for use under Test Matrix Testing.

The SFSETF will meet these objectives by examining the following operational conditions:

i. Startup from ambient to hot, and shutdown from hot to ambient conditions.

ii. Intermediate temperature steady operation: Nominally 200C.

iii. Ambient steady operation: Nominally 25C.

iv. Pressure boundary integrity via pressurization with helium to 200 kPa.

v. Exchange flow and diffusive plena transfer transient operation.

These requirements will be met through the shakedown tests described below.

Pre-Operation: The purpose of this test is to prepare the SFSETF for power range operation. The test objectives are to establish a baseline facility configuration and verify operability of all components controlled from the operator's terminal.

Purge Circulator and System Thermal Inertia Characterization: The purpose of this test is to characterize the performance of the purge circulator, and verify operability of flow velocimetry/switch instrumentation. It may also be used to collect differential pressure data across the core region for expected gas types, but this is not critical to the success of the experimental program.

Exchange Flow and Diffusion Test: The purpose of this test is to prepare the SFSETF for powered transient operation, and characterize the performance of the 4" ball valve, which simulates a break. This series of test will be conducted with the cross duct in the HIGH and LOW positions, and at the high and low temperatures selected from the Test Matrix to explore the effects of gas density and geometry on exchange flow.

Ambient Operation Characterization: The purpose of this test is to characterize the test facility during startup, shutdown, and steady state operation without heat input. The objective is to measure facility data without heat input to fully characterize any drift or hysteresis. Ambient conditions are defined as verified within tolerance ICC thermocouple readouts as being within 1.5C of each other (applicable to all operable TCs), and below 30C.

4.3.1 Intermediate Power Operation Characterization

The purpose of this test is to characterize the test facility during startup, shutdown, and steady state operation with intermediate heat input. The objective is to measure facility data with a nominal heat input to fully characterize any drift or hysteresis. Intermediate power conditions are defined as verified within tolerance ICC thermocouple readouts as being within 1.5C of each other (applicable to all operable TCs), above 175C and below 200C.

4.3.2 PPV Mass Loss Characterization

The purpose of this test is to characterize the mass losses from the SFSETF. The test objective will be to collect pressure and gas composition data from the facility over an extended period of time, from which mass loss can be calculated.

4.3.3 PPV Heat Loss Characterization

The purpose of this test is to characterize the heat losses from the SFSETF. The test objective is to collect process data from the facility during cooldown to ambient, from which heat losses can be calculated.

4.4 Experimental Procedure

4.4.1 Experimental Program and Test Hypothesis

The OSU SFSETF is designed to examine heat and mass transfer that occurs during an air-ingress scenario in order to determine and quantify ONC time in the SFSETF. The purpose of this testing is to provide data and guidance for code validation, and to provide guidance with respect to ingress mitigation system design. While this may be done in several ways, this work has adopted a simple statistical difference test in order to maximize experimental efficiency.

The experimental hypothesis is stated again here.

Diffusive ingress biases experimental results. Therefore, recreation of diffusive ingress mechanics will have demonstrable effect on ONC time in a similar facility. This may be stated as a null hypothesis in the following way

$$H_0 : \tau_{ONC}(diff) = \tau_{ONC}(con)$$

Rejection of that hypothesis directly confirms the importance of ingress mechanics on event progression. Restated with average estimates of onset time, and with respect to duct position, this becomes

$$H_0 : \bar{\tau}_{ONC}(Duct\ High) = \bar{\tau}_{ONC}(Duct\ Low)$$

This statement is driven by the expectation that experimental conditions will feature pre-existing convective currents driven by thermal stratification (and in turn by heat transfer within and out of the SFSETF). These currents will interact with ingressing air in the lower plenum to onset free convection within the facility within minutes, possibly immediately depending on the kinetic energy of those currents. Further, it is expected that precluding direct access to those currents is a more effective mitigation strategy than other flow retardant methods.

Therefore, cross duct placement, High or Low, will be the method by which that argument is interrogated. Insufficient instrumentation exists to determine flow rates, or direction, for bulk transport; restriction to ONC time as a significance indicator of ingressing fluid access to those currents is chosen as the appropriate interrogation method. However, the selection of initial conditions challenges this work, as it fundamentally differs from other scaling analyses and experimental efforts.

And so, the following consideration is given towards initial conditions.

i. Achieving steady conditions across the entire SFSETF is unlikely. However, priority should be given towards achieving steady plena conditions as much as possible. Plena that undergo active heating/cooling in this configuration may bias convective results in that direction.

ii. Heat input should be kept as steady as possible and should, ideally, keep pace with heat rejection through the SFSETF walls or top cover plate.

Table 27 presents the test matrix used in this work. Due to time constraints, caused by delays in achieving a qualified pressure boundary, has severely limited the repeatability of the tests. Therefore, a strict focus was placed upon repeating experiments with minimal intervention before repositioning the cross duct. Additionally, test data was collected in the following format in order to streamline analysis and minimize file size.

XXX_001122_00X.csv

Each test is assigned a designation, outlined below, in order to minimize computational burden when manipulating collected data files. Numerics refer to the date the test was performed, or to the repetition number. Few repetitions were performed.

i. Ramp-up to Temperature (RUT): These tests feature the soak time used in the SFSETF. The duration of these tests is limited by either thermal stability of the upper or (more frequently) lower plena, or the alarm state of the O2 sensor.

ii. MT*X*: Matrix test, using either MTH or MTL to signify whether the cross duct was in the high or low position, respectively. These tests are terminated according the O2 sensor output, or according to time constraints.

iii. Overnight (ON): These tests were performed in order to collect long lived concentration data, or to provide further data when a presence in the lab could not be provided (in such cases, mains voltage was disengaged from the SFSETF).

iv. CntrlXX: Unheated control tests, these tests were performed in order to quantify heat input to system response. However, stagnant helium led to the O2 sensor being constantly in alarm state, and was therefore not energized (and output data is unavailable).

v. Leak Test (LT): These tests saw the SFSETF pressurized to 200+ kPa with air and helium, and then bubble tests were performed, as per OSU-SFSETF-TEST-9100-001 (cite). Additionally, the system pressure is monitored in order to provide quantitative mass leak rates.

In order to properly initiate experiments, the following steps were taken prior to each experiment.

0. Initiate DACS system and assure that mains voltage is connected, and instrumentation voltage is applied.

1. Evacuate the Facility using the Vacuum Pump mounted to the VS seismic stand. A medium vacuum, here defined as less than or equal to 10 kPa_{abs}, is to be drawn.

2. Assure that BV-01 is in the CLOSED position.

3. Fill the PPV with helium until pressure readings read approximately 100 kPa, or ambient conditions. Confirm pressure boundary is holding with PT-002 readout.

4. Open the Vacuum Pump isolation valve and allow the VS to fill with ambient air from the laboratory space.

5. Heat the PPV to the desired initial conditions are achieved. Excess helium should be bled off using the relief valve in order to approximate ambient conditions.

   a. Nominally, this involved a steady UP temperature of no less than 175C, but plena temperatures are largely independent of active control.

   b. Thermal gradients across plena were usually of approximately 100C.

6. Open BV-001 to initiate the experiment.

7. Allow to run for no longer than 600 minutes, then disengage heater rods, terminate experiment, and secure mains voltage connection. Experiment may be terminated O2 sensor output confirms sustained presence of oxygen, as that is taken to indicate natural convection has onset.

Table 27. Matrix test set used in the SFSETF.

Date	*Matrix Test Name(s)*	*Duct Position (Horizontal, Vertical)*	*Average Plena Temperature (UP; LP; Celsius)*
May 5	Cntrl01_050518	NULL	NA; NA
May 6	Cntrl02_050618	NULL	NA; NA
May 7	Cntrl31_050718	NULL	NA; NA
May 11	MTH_051118	H	NA; NA
May 13	MTH_051318	H	189.64; 64.01
May 14	MTH_051418	H	188.07; 59.54
May 15	MTH_051518	H	195.18; 80.78
May 16	MTH_051618	H	NA; NA
May 17	MTH_051718	H	188.24; 96.37

May 19	MTL_051918	V	83.92; 63.33
May 21	MTL_052118	V	181.48; 87.05
May 23	MTL_052318	V	200.24; 86.55
May 24	MTL_052418	V	156.47; 71.56

5 Results and Observations

The following section provides a comprehensive overview of the results achieved from execution of the matrix test set outlined in Table 24.

5.1 Diagnosis of Onset of Natural Convection (ONC)

The primary challenge associated with this, and all other similar works, is the determination of when to terminate the experiment. Based on previous phenomenological understanding, that is interpreted to mean at the onset of global free convection. While visual methods provide a convenient, and instantaneous method, two-vessel apparatuses must utilize discrete measurements. Given the O2 sensor placement, a detectable and growing presence of oxygen in the upper plenum is selected as indication of ONC. Figure 46 presents a time-dependent trace of the O2 sensor output in order to illustrate the diagnosis more clearly.

A note: The time stamp is a function of the DACS system up-time; however, the test time begins when BV-01 is opened. This moment may be found using the pressure transducers in the cross duct and VS, PT-002 and PT-001 respectively. Regard Figure 45, which presents an example of such pressure equilibration, as an example. The time associated with this moment will be presented, alongside the determined ONC time, if applicable.

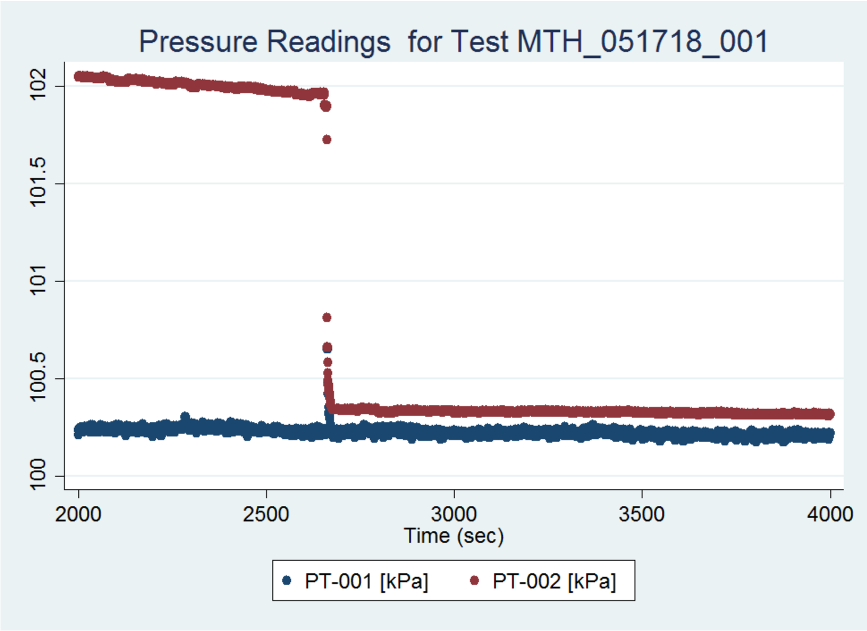

Figure 45. Example pressure traces, indicating pressure equilibration, and experiment initiation.

Figure 46 presents the oxygen sensor output for the matrix test MTH_051118_001; one may note the null sensor response for the duration of the transient. Valve open time and ONC time are determined, respectively, as: 216.1 seconds, and no ONC time was determined for this test.

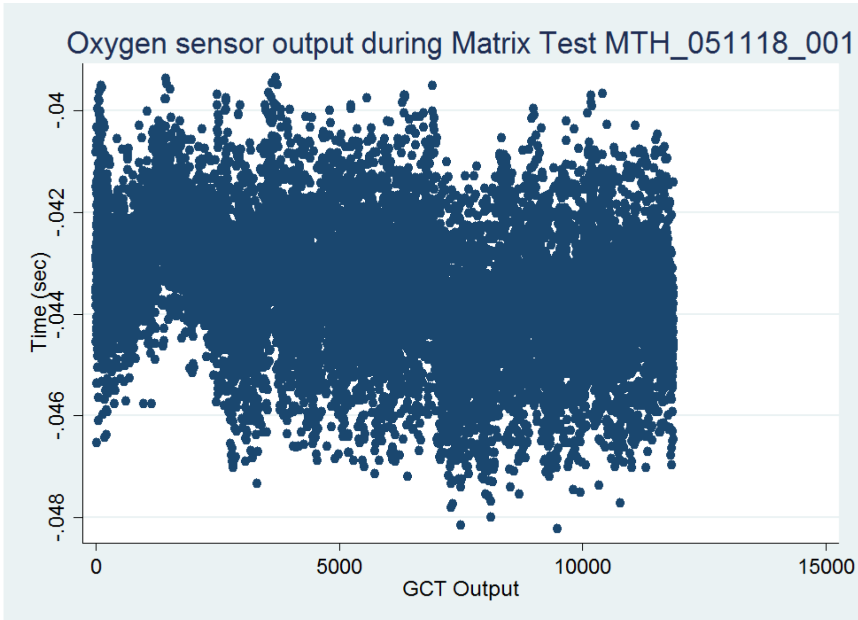

Figure 46. Oxygen sensor output during Matrix Test MTH_051118_001. Constant "Probe Low Temp" alarm noted in transmitter error log.

Figure 47 presents the oxygen sensor trace for Matrix Test MTH_051318_001. Note the initial rise and subsequent 'plateout' of the sensor response. Valve open time and ONC time are determined, respectively, as: 137.3 seconds, and 1065.5 seconds.

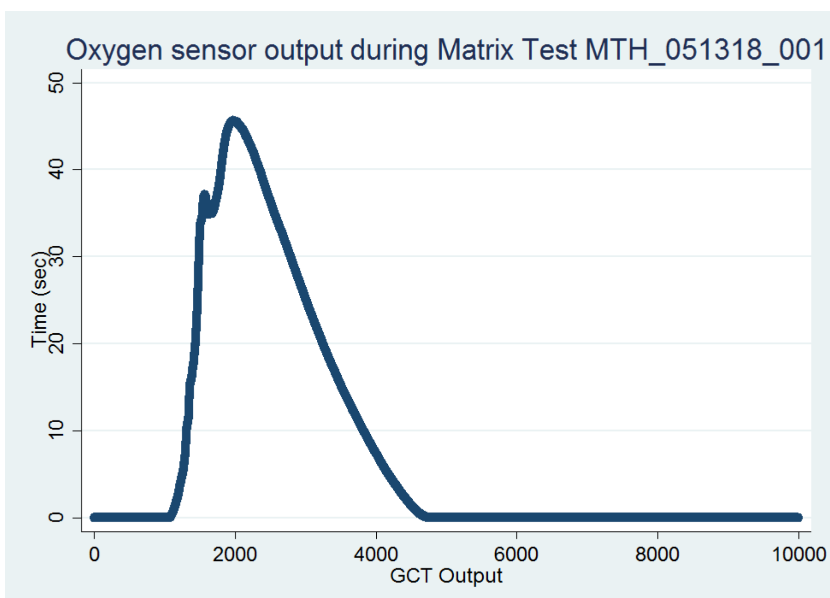

Figure 47. Oxygen sensor output during Matrix Test MTH_051318_001

Figure 48 present the oxygen sensor output for Matrix Test MTH_051418_001. Valve open time and ONC time are determined, respectively, as: 137.3 seconds, and 1065.5 seconds.

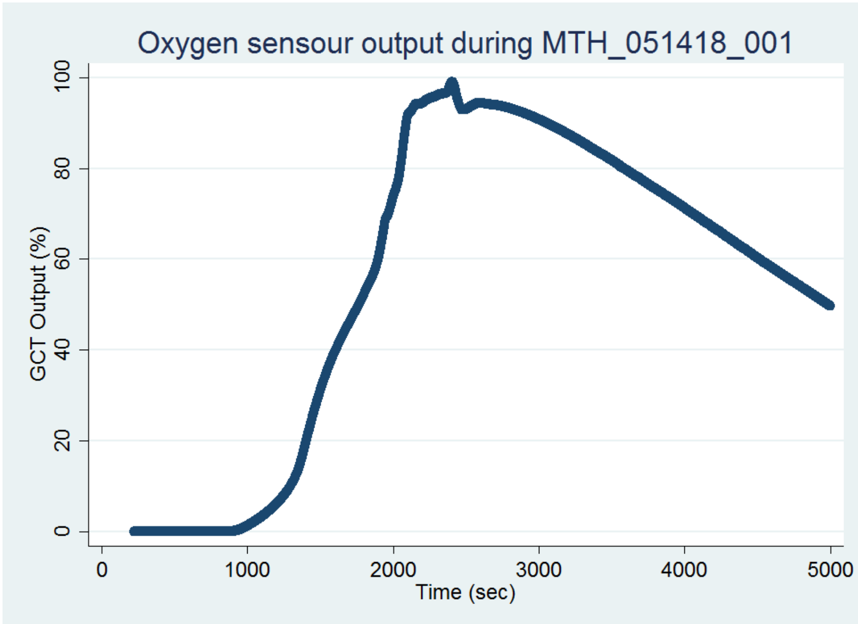

Figure 48. Oxygen sensor output for MTH_051418_001.

Figure 49 presents the sensor output for MTH_051518_001. Note the null response from the instrument during the matrix test. Valve open time is taken as 83.1 seconds, but no ONC time is determined.

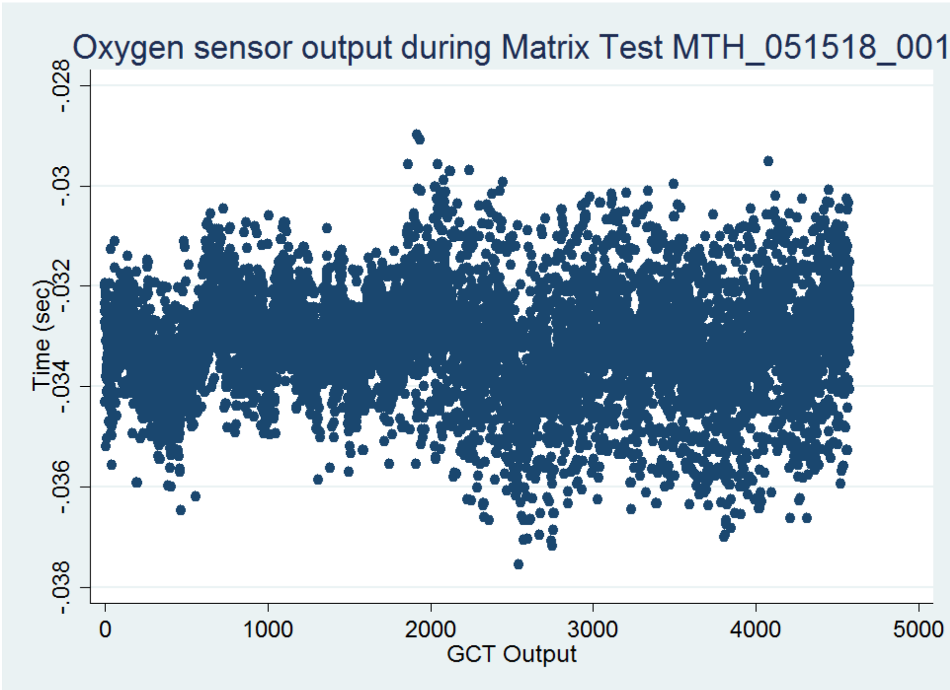

Figure 49. Oxygen sensor output for Matrix Test MTH_051518_001.

Figure 50 presents the oxygen sensor output for Matrix Test MTH_051618_001. Note the lack of immediate effect on ONC to upper and lower plena average temperature. Valve open time for this test is 257.2 seconds, and the ONC time is 2161.0 seconds.

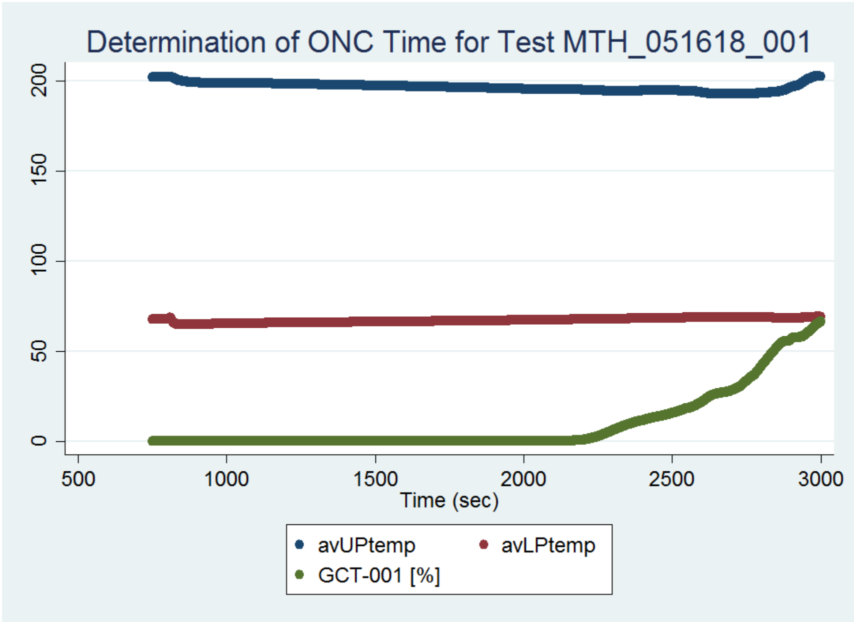

Figure 50. Oxygen sensor output and average upper and lower plena temperatures for Matrix Test MTH_051618_001

Figure 51 presents the oxygen sensor output for Matrix Test MTH_051718_001. Again, note the effect of ONC on upper plenum average temperature. Valve open time for this test is 567.8 seconds, and the ONC time is 4509.9 seconds.

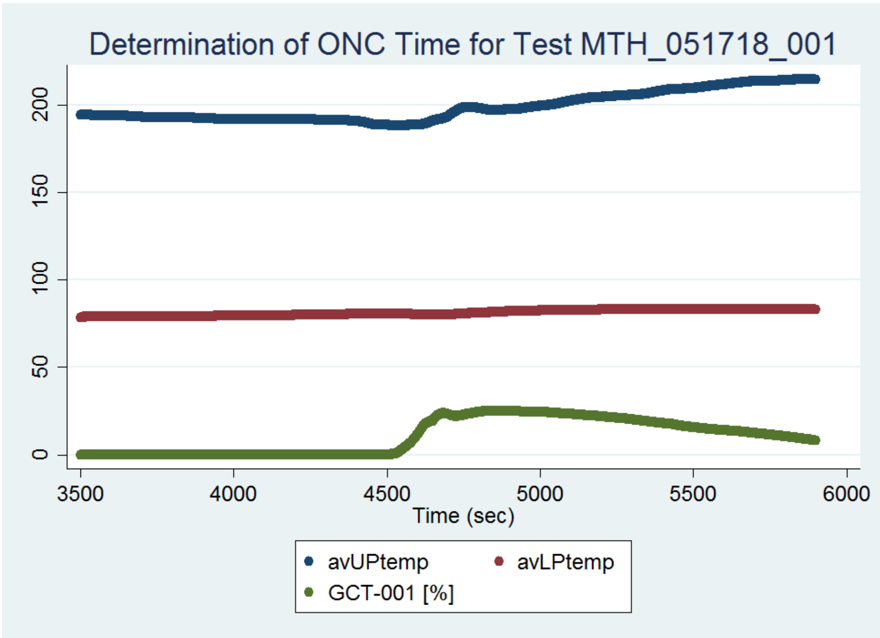

Figure 51. Oxygen sensor output and average upper and lower plena temperatures.

Figure 52 presents the O2 sensor output for Matrix Test MTL_051918_001. Due to time constraints, Overnight Test data is used to determine ONC, as shown in Figure 53. Valve open time is 2546.2 seconds, and ONC time is determined as 8263.8 seconds into overnight test.

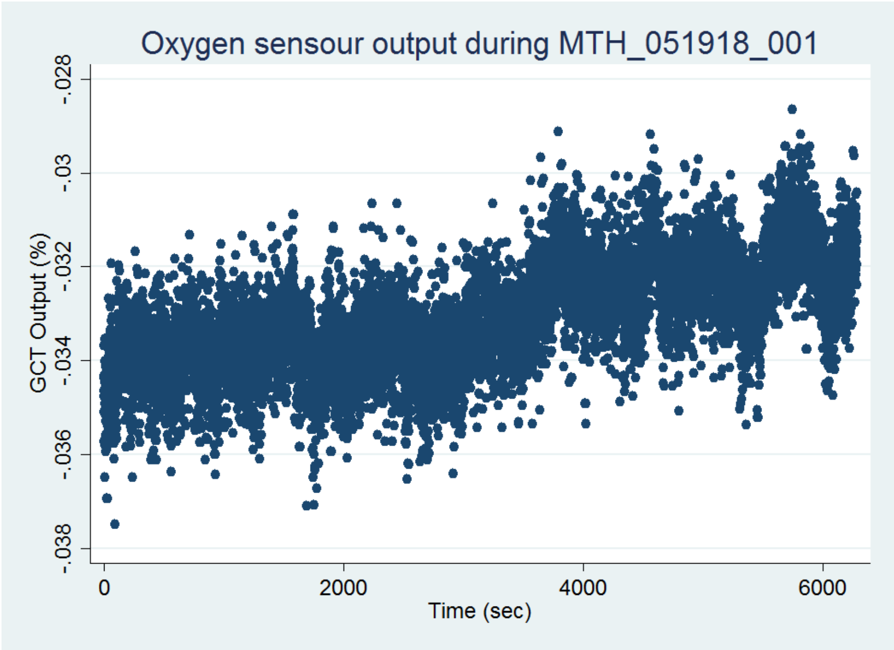

Figure 52. Oxygen sensor output during Matrix Test MTL_051918_001.

Figure 53 presents the oxygen sensor output for the overnight test data used to determine ONC for Matrix Test OT_051918_001.

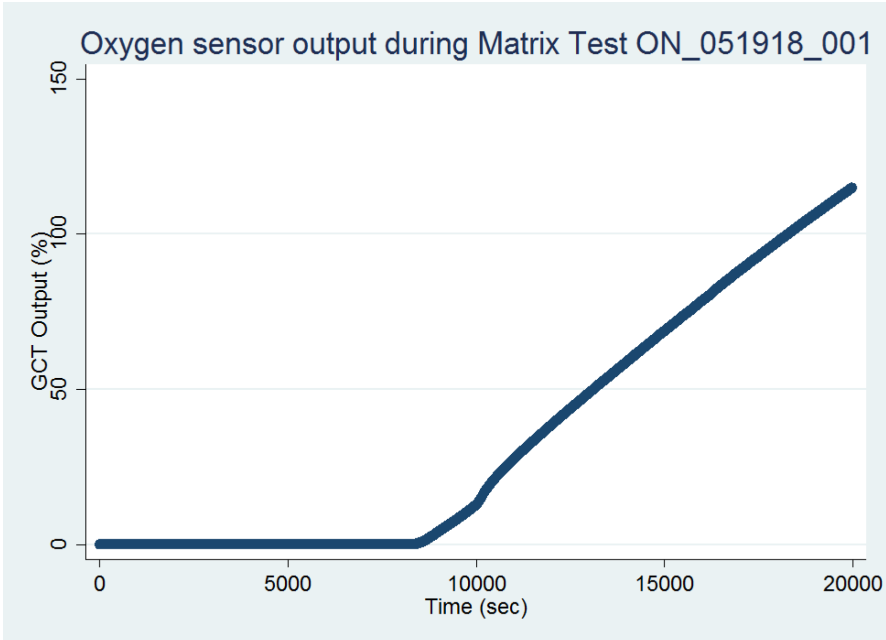

Figure 53. Oxygen analyzer during overnight test configuration, showing oxygen presence in the upper plenum after power had been disengaged.

Figure 54 presents the oxygen sensor output for Matrix Test MTL_052118_001. Note the null value of instrument response. Figure 55 presents that sensor output from the overnight test used, OT_052118_001. Valve open time is 537.1 seconds, and ONC is found 4184 seconds into OT_052118_001.

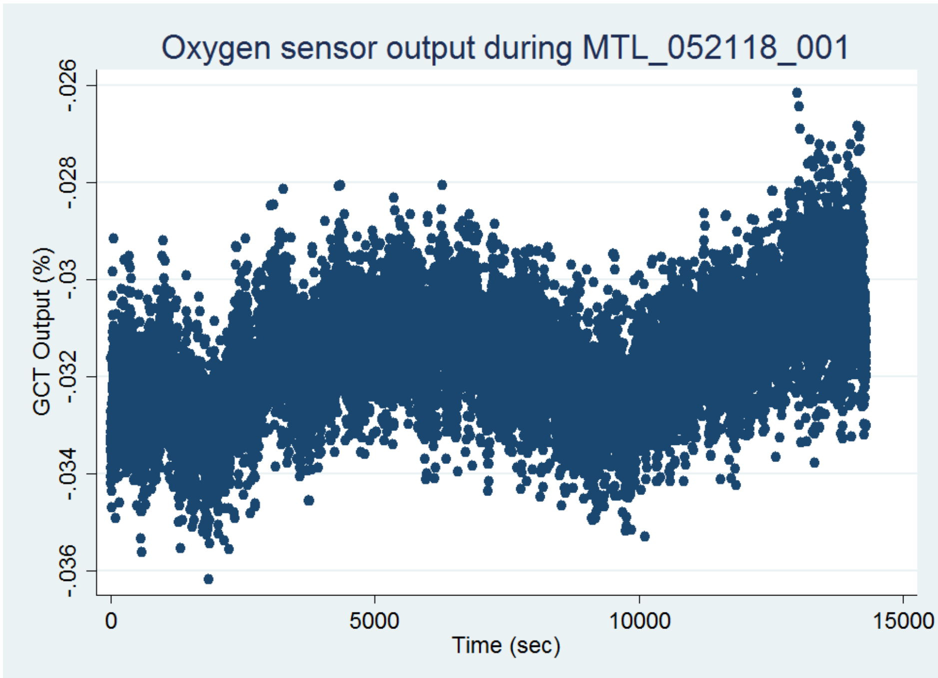

Figure 54. Oxygen analyzer output during Matrix Test MTL_052118_001.

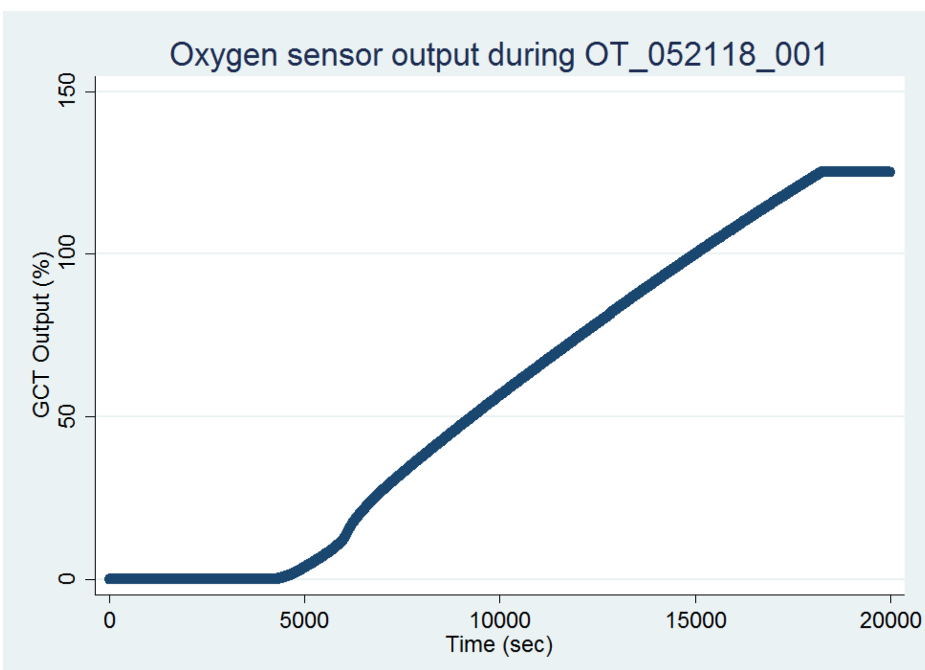

Figure 55. Oxygen sensor output from Overnight Test OT_052118_001.

Figure 56 presents the oxygen sensor output during Matrix Test MTL_052218_001. Valve open time is 71.8 seconds, and ONC is found at 8685.9 seconds.

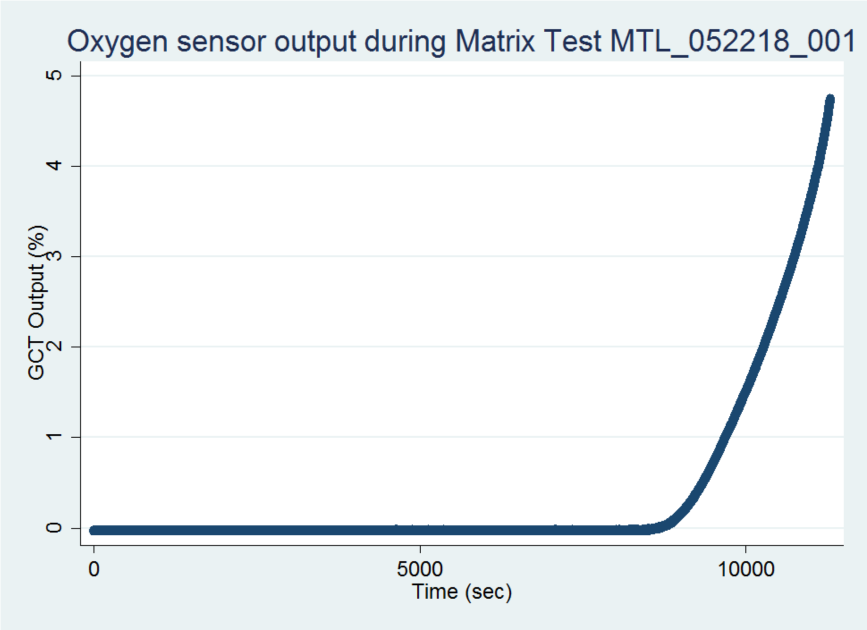

Figure 56. Oxygen analyzer output during Matrix Test MTL_052218_001

Figure 57 presents the oxygen sensor output for Matrix Test _MTL_052318_001. Valve open time is 614.1 seconds, and ONC is 1677.9 seconds. That is approximately 20 minutes, whereas the other tests has taken hours to demonstrate an oxygen presence in the upper plenum.

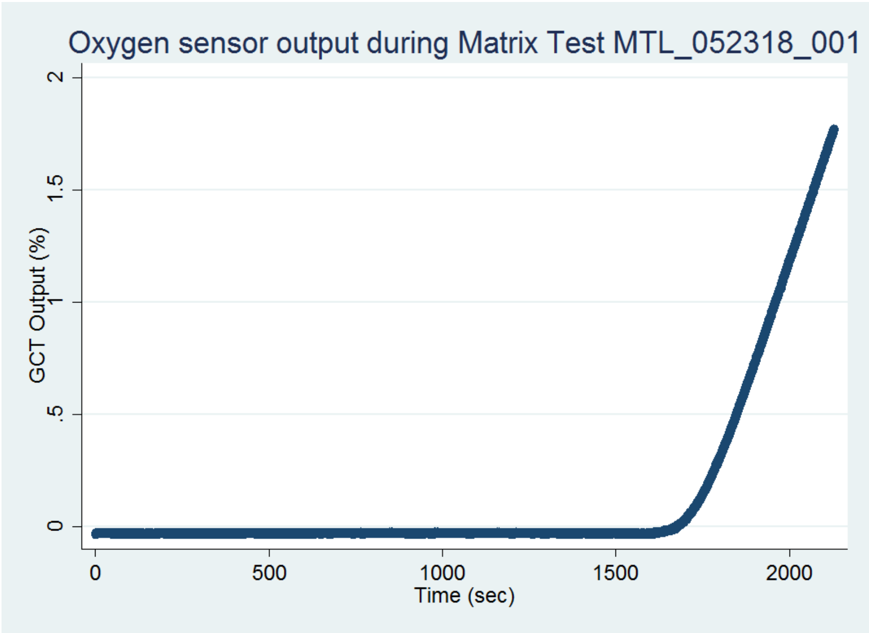

Figure 57. Oxygen analyzer output during Matrix Test MTL_052318_001. Note the time of detected oxygen presence.

Figure 58 and 59 present the oxygen sensor output for Matrix Test MTL_052418_001, and the Overnight Test OT_052418_001. Valve open time is 3451.5 seconds, and ONC is determined at 100042.5 seconds into the overnight test.

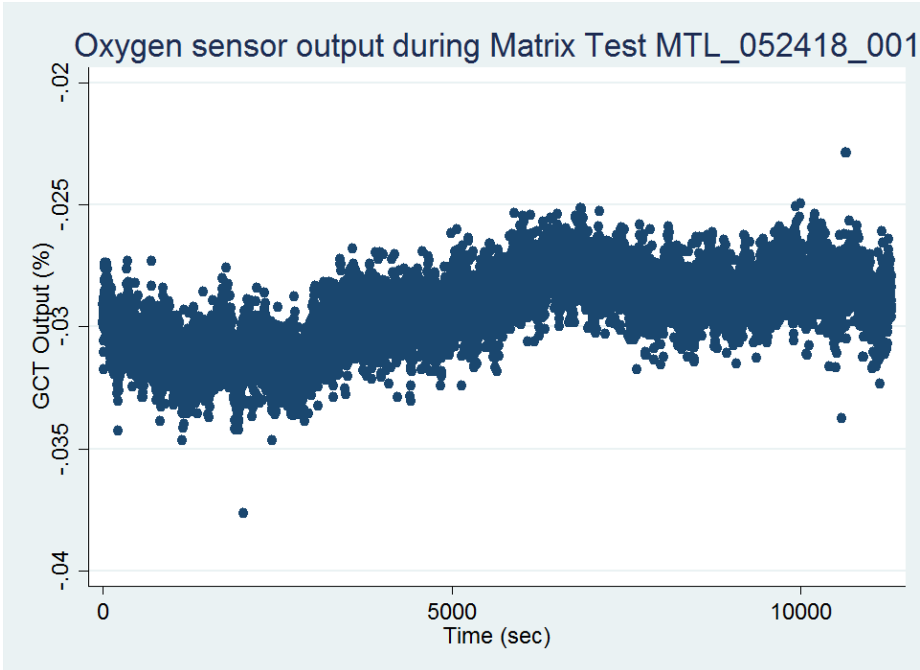

Figure 58. Oxygen analyzer output during Matrix Test MTL_052418_001.

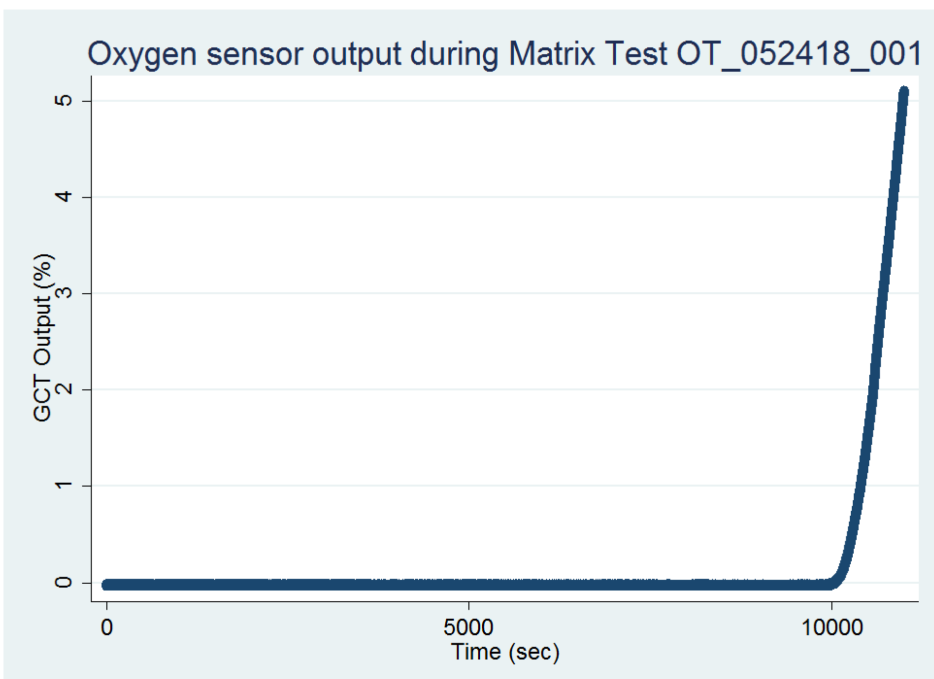

Figure 59. Oxygen analyzer output during Matrix Test OT_052418_001

Using the zero threshold of instrument as the indication of ONC, Table 25 presents the experimental onset of natural convection times determined for each matrix test where appropriate. However, Matrix Test MTH_051118_001 is noted as lacking oxygen analyzer data, and was verified in a constant error state. Operator error may have contributed to this gap in the experimental record.

An additional note on Matrix Tests MTL_0519/21/24: Personnel constraints provided a dilemma in data collection, as long soak times were necessary in order to clear the oxygen analyzer error states, as well as to achieve steady plena conditions. Therefore, these tests terminated without oxygen analyzer response, but still credit the time towards ONC on the following basis:

Any convective action, regardless of the direction of gross energy flux, constitutes an accelerative element with respect to the assumed diffusive ingress. Therefore, PPV cooldown is considered an additional convective element and contributes to ONC time.

Table 25 presents the experimental ONC times determined from the experimental program. Additionally, the diffusive and convective scaling groups for the continuity equation (presented above in Equation 4.18) are also presented. The reference velocity is calculated using the average of the open channel boundary condition calculated in Equation 4.6 to determine an average velocity, as shown in Equation 5.0.

$$\boldsymbol{w_0 = \frac{\int_0^L \sqrt{(2g\beta y\Delta T)}\,dy}{\int_0^L dy} = \frac{2}{3}\sqrt{2Lg\beta\Delta T}} \tag{5.0}$$

The question of when to evaluate the thermal gradient is of significant interest. As the intent is to achieve similarity with respect initial and boundary conditions, the thermal gradient immediately prior to valve open time is selected.

As this calculation is primarily interested in the average momentum input via heating, the integration is restricted to the channel length. However, determination of the diffusive length does account for the increase in length imposed by repositioning the cross duct. A note on the thermal expansion coefficient, $\boldsymbol{\beta}$. Due to time constraints, a scalar value of 0.00369 1/K was implemented, even though this value holds only for air at ambient conditions. Re-evaluation of the value may lead to more meaningful insights, but is left for future work.

Table 28. ONC times for the executed test matrix along with calculate mass transport scaling parameters, evaluated at ONC time.

Test Name	*ONC Time (sec)*	*Duct Position (H/V)*	*Avg Temp. Difference b/w Plena*	$\boldsymbol{\Pi_{dIff}}$	$\boldsymbol{\Pi_{conv}}$
MTH_051118_001	NA	H	125.62	4.76E-05	0.150
MTH_051318_001	928.2	H	128.53	4.76E-05	0.152
MTH_051418_001	546.4	H	114.40	4.76E-05	0.144
MTH_051518_001	83.1	H	91.87	4.76E-05	0.123
MTH_151618_001	1903.8	H	63.33	4.76E-05	0.107
MTH_051718_001	3942.1	H	94.44	4.76E-05	0.131
MTL_051918_001	11,999.8	V	112.15	3.47E-05	0.142
MTL_052118_001	13,768.4	V	113.70	3.47E-05	0.143
MTL_052218_001	8614.1	V	84.91	3.47E-05	0.124
MTL_052318_001	1063.8	V	125.62	3.47E-05	0.151
MTL_02418_001	17,800.8	V	128.53	3.47E-05	0.152

Pending a statistical analysis, one is encouraged to examine the $\boldsymbol{\Pi}$ groups, as they are representative of diffusive and convective action, as outlined in the scaling analysis. Of particular interest is the large variability in ONC time, and the relatively small variation in either the convective or diffusive group. This supports the assertion that fluid injection direction strongly contributes to determination of ONC time.

Moreover, this particular experimental matrix lends itself very well to the paired t-test, which is very fortunate, given that it is a robust test and the assumption of a normal distribution is dubiously presented at this time. Table 26 presents the results of this analysis, performed in Stata, and using the ONC times presented in Table 25.

Table 29. Results of paired t-test interrogating experimental hypothesis.

Variable	*Obs.*	*Mean*	*Std. Error*	*Std. Error*	*95% Confidence Interval*	
ONC_Hi	4	1830.43	759.79	1519.57	-587.851	4248.101
ONC_Lo	4	8861.53	2810.57	5621.15	-82.97	17806.03

$$\boldsymbol{H_0}: \bar{\boldsymbol{\tau}}_{\boldsymbol{Hi-Lo}} = \mathbf{0}\,; \mathbf{dof} = \mathbf{3}$$

$$\mathbf{Pr}(|\boldsymbol{T}| > |\boldsymbol{t}|) = \mathbf{0.1435}$$

$$\mathbf{Pr}(\boldsymbol{T} > \boldsymbol{t}) = \mathbf{0.9282}$$

That is, the means are statistically different at every level greater than 14.35%. However, using the one-sided implementation where $\boldsymbol{H_a}: \boldsymbol{mean}\left(\boldsymbol{\mu}_{\boldsymbol{ONC_{Lo}}} - \boldsymbol{\mu}_{\boldsymbol{ONC_{Hi}}}\right) > \mathbf{0}$, one may reject the null hypothesis with a confidence level of 92.82%.

One may immediately see the impact of the variability introduced by MTL_052318_001. Analysis shows that exclusion of that particular data point significantly impacts the confidence levels; however, this work asserts its inclusion as essential, as it represents the action of complex physics that do not reflect simple diffusion between semi-infinite reservoirs. However, this quantifiable and statistical suggestive (if not significant) lends further support to the following idea:

Cross duct orientation strongly influences the air ingress boundary conditions, and therefore strongly influences the onset time of natural circulation within HTGR facilities.

6 Conclusions

Based on the conducted experimental program, as well as a comprehensive review of the available literature, this work would like to make the following conclusions:

i. The contribution of diffusion to the air ingress scenario is limited exclusively to its dominance as an ingress mechanism, and the applicability of that ingress mechanism is directly coupled to facility geometry.

ii. Orientation of the cross duct along the gravitational axis has a detectable, if variable, retardant effect on the rate at which oxygen reached the upper plenum.

iii. Gravitational potential energy difference will drive mass transport between the PPV and containment, if fluid displacement within the lower plenum is permitted.

6.1 Observations

This section would like to present the observations of this work that do not fit elsewhere, and yet are germane (rather, are considered so by the author) to the applicability of this work.

i. The upper plenum volume exhibits complex convection patterns at steady state and during ramp up to temperature, and at steady state. Several tests indicate a periodic wave form at certain locations in the UP that may be of interest.

ii. Steady conditions are not necessarily at rest – implementation of previous initial conditions (which all set initial velocities to zero) simply is not achievable in an experimental setting. Additionally, initial matrix tests used the upper plenum average temperature as an indicator of facility readiness due to personnel/time constraints. The role of plena temperature change as an indicator of convective communication is a very rich subject that merits further exploration.

iii. The role of differential pressure with respect to diagnosis of ONC was disappointingly ineffective. While it does, at times, show signs of active communication between the upper plenum and the experimental volume, it does not provide sudden and dramatic change to indicate ONC.

iv. Sudden and dramatic change in any parameter is largely absent at any moment when oxygen is detectable with the O2 probe. While this may be a function of instrumentation delay, it is more likely that there simply is no dramatic shift to a global natural convection current, but rather a continuous convective current established by the temperature distribution in the core region.

6.2 Relevance of Work

This work challenges established assumptions regarding the air ingress event in High Temperature Gas Reactor applications; specifically, asserting that the role of molecular diffusion is limited strictly to its ability to influence mass ingress. In geometries that feature a path for fluid displacement driven by gravitational potential energy gradients, one may not assume molecular diffusion will play a significant role in transient progression. In doing so, this work hopes to shift the focus of the community towards establishment of realistically informed boundary and initial conditions regarding this transient.

Therefore, this work would like to offer the following consideration regarding facility design in the meantime:

In the absence of regulatory guidance, passive safety characteristics should be exploited to their fullest extent. Design choices that permit air ingress via fluid displacement do not fully exploit the passive safety afforded by molecular diffusion dominated ingress mechanics. Therefore, orientation along the vertical would maximize passive safety by extending oxygen ingress time (rather than ONC) by forcing molecular diffusion against the gravitational field.

6.3 Assumptions and Limitations

The assumptions of this work are few, but the limitations many. No assumptions were made regarding similarity of thermal gradients, magnitudes, or differences – limiting its applicability to geometrical considerations only. Moreover, no thought has been afforded the chemical reactions that would further accelerate this process via graphite oxidation, which would further accelerate ONC.

This work would also like to note the limitations imposed by instrumentation selection. Due to the low signal-to-noise ratio of the mass flow meter and relatively high uncertainties even in the design stage analysis, no velocimetric data is available for this experimental series. Moreover, even considering the presence of free convection velocities, the heat input and location of MFT-001 render it particularly susceptible to bias.

Additionally, the oxygen sensor also carries limitations. Due to the length of the probe sensor in the heated instrument, a custom coupling was implemented as support, and to position the probe in such a way as to minimize draw effects on the fluid continuum. Equation 6.1 presents the insertion length for the probe, as calculated in *OSU-SFSETF-1540-CALC-001*.

$$\boldsymbol{L_{penetration} = L_{probe} - L_{support} - L_{UP} = 11.375 - 8.375 - 2.25 = 0.75\ in.} \qquad 6.0$$

Location of the probe at such a high elevation was deliberate on the basis presented above. However, it also necessarily forces the probe into a less responsive location, meaning that it is quite possible for that choice to bias results to longer duration times. Future effort would be well spent parameterizing and quantifying that effect on test duration, if any.

7 Future Work

This effort was initiated to experimentally examining the air-ingress scenario in order to support code verification. While that has been accomplished through the generation of traceable data, as well as some basic means testing, it is obvious that there is still much further to go.

7.1 Additional, Broader Scaling Analysis and Comparison

Application of scaling analysis may yet yield valuable information; however, it must proceed unencumbered by the assumptions of previous experimental efforts. Specific areas of interest would include multi-dimensional effects, turbulent mixing, and shear entrainment (depending on problem geometry).

In particular, this work would like to suggest the following considerations as a recommendation for future scaling analyses:

1. Steady free convection in a coolant channel.

2. Steady heat rejection from the coolant to the core barrel, and then transport from the primary system.

These sources present the greatest singular locations of momentum input and output from a prototypical HTGR system, and therefore may reasonably be said to drive the air ingress event.

However, this should also be paired with regulatory guidance regarding treatment of this event, as this work has shown that misunderstanding of the phenomenology can noticeably impede technological development. Therefore, if a double-ended guillotine break is to be treated and accounted as a mechanistic source term, then definitions regarding bounding and initial conditions are critically necessary to advancing the state of the industry, as well as guiding future experimental efforts. The effect of dimensionality has also been noted in computational efforts, in addition to this experimental effort [38].

Equations 7.1 and 7.2 provide a (hopefully) useful starting point with future scaling analyses. Based on the earlier assertion that heat transfer will be dominated via conduction from the solid moderator, initial efforts should be made achieve similarity with respect to thermal gradients at the heat transfer boundary. Achieving those gradients will permit interrogation of the velocity gradients along the channel height, which is a critical next step. Similarly, achieving those gradients at the point of heat rejection (the core barrel), will be as necessary as the coolant channel analysis.

$$\boldsymbol{v\,v' = g\beta\big(T(y) - T_{\infty}(y)\big)} \tag{7.1}$$

$$\boldsymbol{\Delta T^{*}_{channel} = \Delta T_{0} \times \int_{0}^{L} f(v)\,dy} \tag{7.2}$$

Additionally, effort would be fruitfully spent to compare experimental ONC times to evaluated scaling parameters, in order to draw more meaningful and broader conclusions than available in this work.

7.2 Larger Database

While the paired means test is very robust, it does benefit from large volumes of data, and the quantification of the retardant effect of cross duct orientation may be significantly improved. The volume of experimental data speaks to this fact, and future effort may well be spent on replication experiments to reduce variability of ONC times, and improve the quality of provided means estimates.

7.3 Anemometry Studies

This study challenges the notion that any portion of the air ingress event will be governed by molecular diffusion in the reference geometry, and scaling according to diffusive group, as presented in Equation 0.4, will be of extremely limited value.

$$\boldsymbol{\Pi_{diff,R} = \frac{D_R}{L_R^2}} \tag{0.4}$$

Rather, characterizing initial temperature gradients, along with fluid velocities, will be key to the next step in maturing the HTGR technology. Therefore, an anemometry study, paired with computationally informed design and installation of an appropriate prismatic block structure, would be an obvious next step.

Appendix A: Shakedown Testing Results and Lessons Learned

Sealing Efforts and Leak Quantification

While testing was done open to the experimental atmosphere, an effective pressure boundary was critical to the validity of the experimental results. It simply would not do to have air ingressing from undesirable locations. However, this effort proved to be most troublesome due to facility design errors, in addition to other issues that arose during shakedown testing. While this document does not in any way seek to assign blame, it was determined to be of institutional value to highlight and capture these errors.

Critical Leak Locations

Several locations are called out in the Primary Pressure Vessel (PPV), Cross Duct (CD), and Vertical Standpipe (VS). The following section will discuss these leaks in further detail. However, prior to jumping in, it is important to consider the methodology of detection.

A brief note on leak checking with lab supply air: Lab supply air was used to perform the majority of leak checking. It became clear, as leak testing progressed, that long term testing with mass spectrometry equipment to locate and address diffusive leaks would be impossible, due to both physical and scheduling constraints. Rather, a bubble mixture was deemed appropriate for finding bulk leaks for which corrective action could be readily applied.

Also, as this process was a check, rather than official test, iterative with respect to certain corrective actions (epoxy and silicone placement, to be specific), and time consuming (often requiring 24 hours to cure), test records in the form of written and executed procedures were not kept or maintained for this process. Moreover, as the SFSETF leaked quite profusely during its initial startup, any benefit of a detailed and thorough record of sealing attempts would be strongly outweighed by its administrative and operational burden.

However, the procedure utilized largely followed that outlined in the procedural document, OSU-SFSETF-TEST-9100-001 [40] in which a flow path is established to the PPV, either directly if the CD ball valve is closed, or through the VS if open. Once pressure is applied, the isolation valve to the vacuum pump is closed, and the air supply disengaged so as to completely isolate the SFSETF.

At this point, the experimenter may regard the pressure trace to determine initial leak size, and listen for hissing in order to help locate the leak location. Special care should be taken so as not to confuse ambient sources of sound in the Radiation Center building for leaks and implement corrective actions for a falsely identified leak.

Leak locations were explicitly located by using a bubble mixture, once a preliminary estimate had been established, at which point corrective action recommendations were considered.

Persistent Leak Locations

Table 27 provides an overview of the leaks encountered, and provides discussion and insight into leak cause, based on leak check results.

Table 30. Overview of persistent leak locations, and brief discussion of leak.

Vessel	*Location (Figure #)*	*Discussion*
Top cover flange circumferential face	Figure 60	Persistent leaks detected at numerous locations at the face that were resistant to sealing with various forms of epoxy and sealant. Root cause is likely incomplete seal of packing material.
Top cover plate fasteners	Figure 61	Persistent leaks detected at superior and inferior faces, despite the inclusion of various gasket materials and torque values. Root cause is likely incomplete seal of packing material
Top cover plate bolt circle	Figure 61	Limited bolt circle penetrations, and vertical co-location with limited clearance with power line pass-throughs. Root cause is design oversight.
Bottom cover flange circumferential face	Figure 62	Persistent leaks detected at numerous locations at the face that were resistant

		to sealing with various forms of epoxy and sealant. Root cause is likely incomplete seal of packing material.
Bottom cover plate fasteners	Figure 62	Persistent leaks detected at superior and inferior faces, despite the inclusion of various gasket materials and torque values. Root cause is likely incomplete seal of packing material
Cross duct high flange face	Figure 63	Persistent leaks along the circumference. Various factors at work, including uneven mating surfaces, inappropriate gasket material, and ineffective installation.
Cross duct low flange face	Figure 63	Persistent leaks along the circumference. Various factors at work, including uneven mating surfaces, inappropriate gasketing material, and ineffective installation.
K-type thermocouple pass-throughs at Bulkhead Fittings T14, 24, 34, and 44.	Figure 65	Persistent leaks due to ineffective establishment of a pressure boundary at 75% penetration.
Power line pass-throughs	Figure 60	Persistent leaks due to inability to seal around the braided wire, and the facility feedthrough cannot be removed.

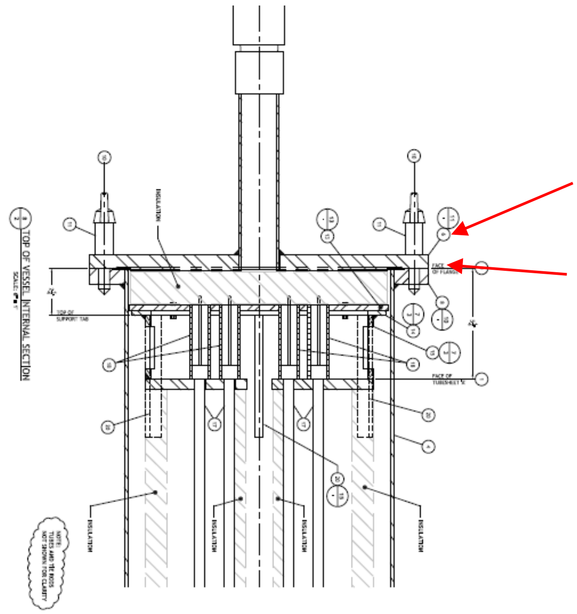

Figure 60. Persistent leak locations detected in the upper plenum area of the SFSETF, with callouts identifying persistent leak locations.

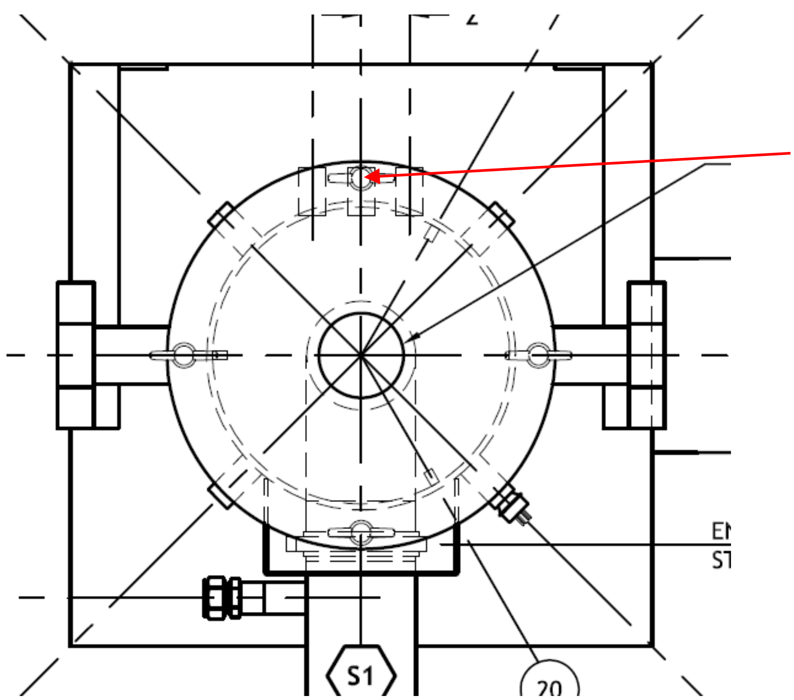

Figure 61. Upper plenum top cover plate detail view with callouts identifying persistent leak locations.

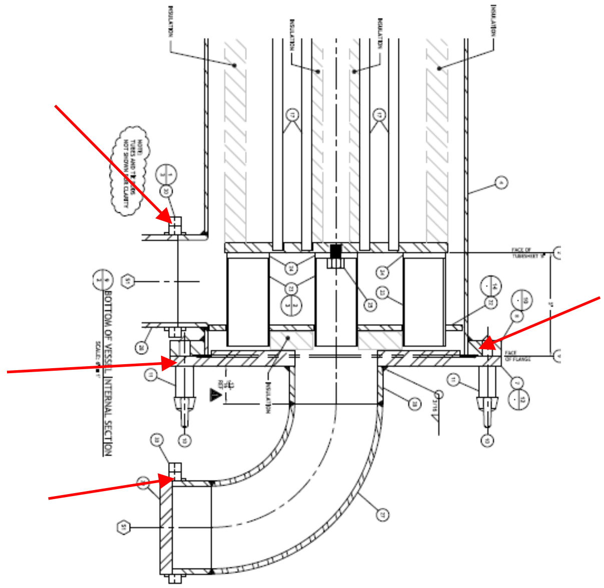

Figure 62.Lower plenum close up view, with callouts identifying persistent leak locations.

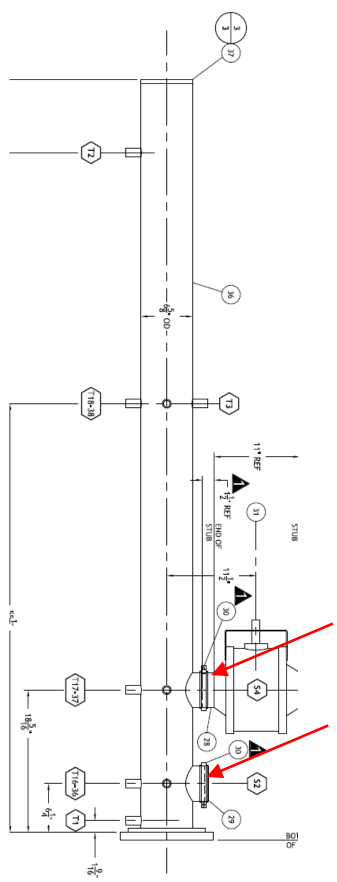

Figure 63. Vertical standpipe, side view, with callouts to indicate persistent leak locations.

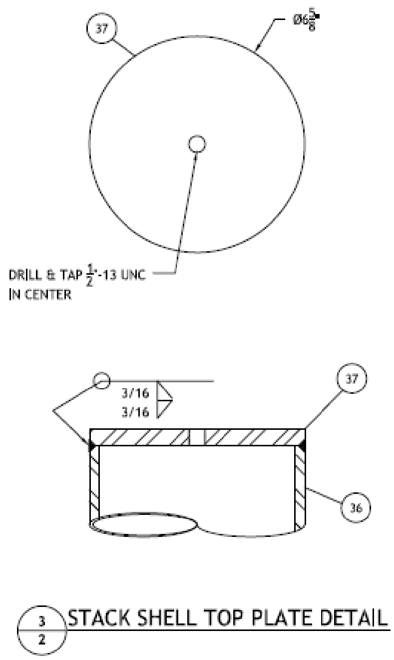

Figure 64. Vertical standpipe top detail, highlighting the presence of a tap location.

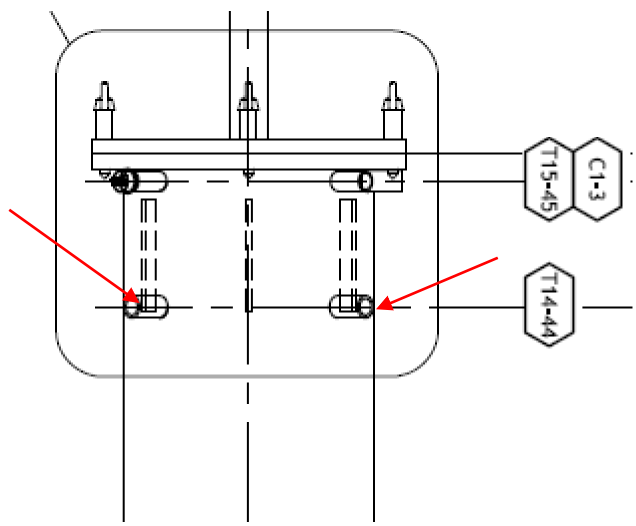

Figure 65. PPV detailed view, with callouts to highlight the locations of T14-44.

Vertical Standpipe

The Vertical Standpipe was the first target of sealing efforts, due to its relatively simple geometry and limited number of instrumentation pass-throughs. However, it provided an early example of future difficulties.

Figure 64 shows the stack shell top detail taken from the finalized shop drawings, provided by Harris Thermal. In particular, it details a drilled and tapped hole: ½”-13 thread.

It should be noted that the presence of this hole serves no instrumentation purposes, and moreover may have been tapped with a very worn die, as significant thread damage was found following initial bolt installation. This required the addition of significant chemical resistant PTFE tape, and a bolting torque of no less than 900 in-lbs.

Other leaks were detected at various compression fitting joints that required some additional torque, but were tightened no greater than 150 in-lbs.; though none met that torque rating before providing an adequate seal. However, one of the greatest challenges was presented by the v-band clamps implemented to join the cross-duct and vessels, as well as the vessel plugs for the unused duct fittings. A detailed view of these clamps is shown in Figure 66.

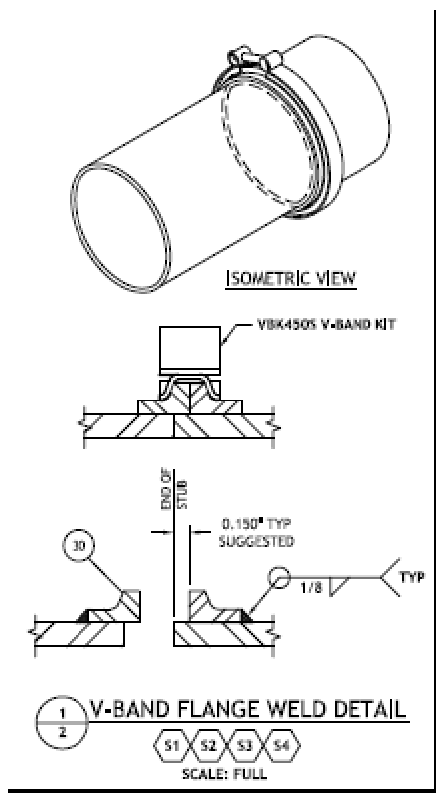

Figure 66. V-band flange weld detail in facility drawings.

Critical to note is the drawing shows metal-on-metal contact between flange faces. However, included in delivery on all v-band clamps were rubber gaskets whose outer diameter significantly exceeded the flange face outer diameter. This made achieving an effective seal impossible at the vertical standpipe locations and their analogs at the PPV. It also become clear that this gasket was not applied correctly, or formed a contiguous boundary.

Additionally, upon removal of the clamps, it became very clear that an even mating surface between both flange faces was impossible to achieve, with nicks and gouges in several locations, as well as warping of the faces due to uneven heating, likely from the welding process. Therefore, significant efforts were made to achieve a pressure boundary both here and elsewhere using a technique referred to by the Facility Manager as Negative Pressure Sealant Application, which will be discussed in the following section.

Corrective Actions: Negative Pressure Sealant Application

The challenge posed by these clamps is significant, in that clearance of no less than 1/16” existed in many locations around the circumference of any given clamp location, and occasionally increasing due to mechanical damage or warping. Such large gaps provide a significant challenge, as gaps provide a significant amount of “blowout” force that can severely impede any seal achieved by circumferential application.

Restriction of sealant mobility

An effective seal requires more interventions than a topical application of a sealant. Several observations led to the following confounding factors:

1. Leak paths may develop as loose material relocates while curing.

2. Leak paths may develop as material gets blown out of application areas.

3. Bubbles may nucleate at such sites that permit, such as the surface of braided wire.

The root cause of some of these confounding factors may be intuitively traced to the geometry and materials properties of the problem. That is, it is of significant interest where a.) Material is applied, and b.) Which material is selected.

High temperature silicone was an early choice as a sealant, and was applied extensively. While results were mixed, silicone proved to be especially susceptible to blowout, and a composite approach involving the high temperature, high pressure thread sealant, Copaltite, was implemented.

Even as a “Cement,” Copaltite is quite loose; or rather, Copaltite of any form is less viscous than silicone. Moreover, it cures very hard, and is resistant to temperatures and pressures up to 1200° F and 6500 psi on a flange joint without a gasket, according to the manufacturers. Therefore, the following process was developed in order to apply Copaltite and Negative Pressure Sealant Application to the affected areas:

1. At ambient conditions, remove v-band clamp, along with any packing material included (gaskets, PTFE tape, etc.). If necessary, clean with isopropyl alcohol and wire brush.

2. Apply Copaltite to flange joint using a 60 mL syringe or other functional application.

3. Cure for no less than 30 minutes using mobile heat source; specifically with a 600 W heat lamp, capable of producing temperatures up to 350° F from 5 inches away. With a duty life of 30 minutes at a time, it may be necessary to reposition the lamp after a cooldown period to assure that the Copaltite set up around the circumference of the joint.

4. Apply a strong vacuum on the SFSETF, taking care that fluid transfer path is open between the flow path and the joint (check the ball valve position), down to 30 kPa_{abs}. Wide tolerances may be implemented, but a relatively strong negative pressure is ideal.

5. Using the appropriate applicator(s), apply silicone to the circumference of the joint.

6. Once a FULL AND CONTINOUS BEAD of silicone is established, apply some form of restriction to reduce silicone mobility. Experimenters’ recommendations include self-adhesive tape (PTFE tape is also excellent, though requires NO LESS than 4 wraps to provide a seal, 6 was often favored), or correctly sized hose clamps for the bold and dexterous.

7. Let cure for NO LESS than 12 hours, or 24 for optimal results.

Once this process had been implemented at all clamp locations, other persistent leak locations were addressed. This process, repeated at every flange joint, led to an adequate seal at those locations.

Corrective Actions: Over Torque and PTFE Tape at the VS Top Cover Plate

The pernicious tap shown in Figure 5 was a straightforward penetration to address. However, it does bear noting that the tap was made with an exceptionally worn die, as the thread profile showed significant wear when removed, and required significant torque (no less than 1000 in-lbs) to seat the bolt effectively. With these corrective actions, all penetrations, welds, and pass-throughs in the VS passed air tests, and led to no greater than diffusive loss of helium under pressure.

Cross-Duct

The cross-duct features fewer penetrations than the VS, and therefore presented a substantially smaller challenge with respect to achieving an effective pressure boundary. However, the 4" Worcester ball valve did present a challenge, as several of the bolt locations showed leaks under bubble tests. It was therefore necessary to increase bolt torque at those locations (using the following the 6-bolt torqueing pattern) until all penetrations showed no indications of leaking.

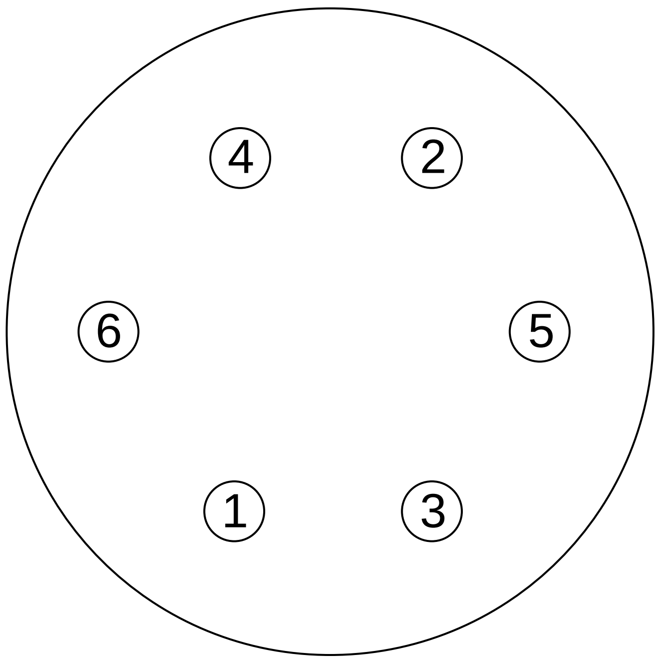

Figure 67. Worcester valve flange bolt torque pattern

Mercifully, no other penetrations, including the flow switches, mass flow meter, and oxygen sensor probe support (and plug), showed no leaks under air pressure.

Primary Pressure Vessel

The PPV demonstrated a formidable challenge as persistent leaks developed in a number locations, as outlined in Table 26. While hindsight is of considerable use, it was not immediately clear what that the root cause of the problems were. Thus, a brief discussion regarding interactions with Harris Thermal, the fabricator of the vessel, is essential.

Graphite packing as gasket material

The challenges associated with high temperature helium experimentation are numerous, though they may be fairly summarized as follows: High temperatures, (low to high) pressure, and high mobility.

To address these challenges, the design pressure of the SFSETF is not greater than 3 atm/44 psi. The design logic behind this choice is that limited pressurization is necessary to study the breakup of thermal and chemical stratification layers. But, high temperatures (>200C in some locations) may pose a challenge to certain available types of closed cell material, such as silicone rubber, when used in the hottest locations of the vessel. That is, silicone rubber may be effective in the lower plenum, the upper plenum may provide too challenging an environment.

Graphite packing was suggested during design meetings, and was eventually adopted and approved by the Facility Manager, as shown in Figure 68, which calls out McMaster Carr product #9457K5, which refers to a steam-resistant packing seal.

9	GASKET	2		CERAMIC FIBER	1/8" THK PACKING FIBER WRAPPED 3 TIMES OR MORE TO FORM 12-3/4" ID X 13-1/2" OD, MCMASTER CARR ITEM #9457K5 OR EQUAL

Figure 68. Closeup view of the line item suggested and approved for gasket material.

The assumption must have been that wrapped three times in the machined groove would provide sufficient resistance to achieve an effective seal. This is incorrect however, and was especially so when installation reached the lower plenum cover plate. Figure 69 shows the gasket groove machine into the lower plenum cover plate. Note in particular that it faces downward, which raises significant challenges for vertically configured installation attempts, like those depicted.

Figure 69. Close-up view of packing installation to the lower plenum cover plate.

However, if there were any concerns about repetitive wraps providing a strong effect, the upper plenum cover plate quickly provided contradicting evidence by failing repeatedly and in a variety of ways. While this work will endeavor steadfastly to avoid conjecture, it is still the adamant belief of the Facility Manager, with hindsight as helpful guide, that the weave, or discontinuous nature of the material, fundamentally precluded an air-tight seal, to say nothing of helium.

Later results would come to support this argument.

Utilization of packing material allowed for the relatively low torque application recommended previously [41]: 13.7 ft-lb/fastener (approximately 165 in-lb). Which is particularly convenient, as the total force requirement is well within bolt circle sealing capabilities. For the sake of absolute clarity, there are a total of four (4) drilled and tapped bolt holes in each fastener circle to seal the upper and lower plenum, and this represents a significant challenge to sealing efforts and it bears discussion:

i. Limited tensile yield strength of commercially available fasteners.

ii. Limited clearance for any adjustment to fastener size.

iii. Physical deformation (warping) of the cover plate if fasteners are over tightened.

Equation B.01 provides an estimation of the clamping force available from pre-existing hardware, assuming the following:

i. ASTM A193 B7 grade bolt material.

ii. 4 bolts available.

iii. Loaded to 60% of the minimum yield strength: 63,000 psi.

iv. Cross sectional area of ½”-13 UNC bolts is 0.1419 in^2.

$$W_{pre-existing} = 4 \times (63,000\ psi) \times \left(0.1419\ in^2\right) = 35,758\ lb_f \qquad \text{B.01}$$

It is therefore clear that the operational success of the SFSETF therefore required adjustment from this design in order to assure the pressure boundary integrity.

Use of Finger Clamps to Provide Clamping Force

The first priority should therefore be to increase the clamping capacity of the SFSETF. Finger clamps were an obvious choice, especially if paired with steel step adjustment blocks of the appropriate size to provide opposing moment forces.

Table 28 presents the relevant findings and parameters of the calculation.

Table 31. Parameters of interest taken from OSU-SFSETF-7140-CALC-002, on the selection of finger clamps.

Clamping force required	*Finger Clamp Size (Height x width x OAL)*	*Bolt Size*	*Bolt Grade*
89,274.35 lb_f	¾” x ¾” x 4”	¾”-10 | ½”-13 UNC in pre-existing locations	B7
Finger Shear Stress	*Finger Material*	*Finger Shear Yield Stress*	*Step Adjustment Block Material*
28,056 psi	1018 Steel	33,763 psi	1018 Steel

Assuming lubricated fasteners, Equations B.02 and B.03 briefly outline the torque necessary to apply to each bolt necessary to achieve that 89,275 lb_f of clamping capacity.

$$\tau_{Tightening} = kDnF \quad \text{B.02}$$

$$\tau_{Tightening} = (0.15) \times (0.75\ in.) \times \frac{89,274.35\ lb_f}{9\ bolts/circle} = 1115.93\ in - lb \quad \text{B.03}$$

Lubricated with graphite joint compound, this is achievable with the torque wrench found within the lab. As for the designation of utilizing nine (9) additional bolts per circle, the decision was based on the tensile strength of bolt geometries and steel clamp geometry firmly established as constraints.

Utilization of Graphite w/Stainless Steel Foil Insert Gaskets and Flange Sealing Strategy

With the increased clamping availability, it was necessary to size, select, and order the appropriate gasket. The following constraints guided gasket selection:

i. Increased surface area would be preferable, so that the gasket might sit between flange faces rather than within the groove. In so doing, significant installation challenges may be avoided, and a more effective seal might be assured.

ii. Closed cell structure; there absolute cannot be any obvious flow paths through the gasket.

iii. Absolute least clamping, or seating, force required.

With the inclusion of these constraints, and the recommendations of Hennig engineers, the GRAPH-LOCK 3125 (SS laminated with graphite 1/16” on either side) was selected as the gasket of choice. Featuring a y value of 2500 psi, and featuring a cross sectional are of 52.5 in^2, it is quite possible to supply sufficient clamping force necessary to seat this clamp, as well as additional margin to over-torque, if necessary.

Abandonment of Surface Mounted Thermocouples TF-040/42 and TS-01/2

Several interventions were attempted in order to achieve an effective seal at the instrument pass-throughs at the following bulkhead fittings: T14, 24, 34, and 44.

While the details of all the failed interventions are beyond this document, the following have been attempted:

i. Inclusion of silicone.

ii. Inclusion of JB-Weld, PC-7, and other epoxy materials.

iii. Complete removal of potted plugs in favor of Multiconductor Feed Throughs (MFTs) from Omega, with cladding to protect transmission wire.

iv. Further inclusion of silicone.

v. Relocation of plugs.

Figure 70 shows a detail view of the potted plugs following removal – note the nucleation holes at the wire OD and elsewhere within the potting material.

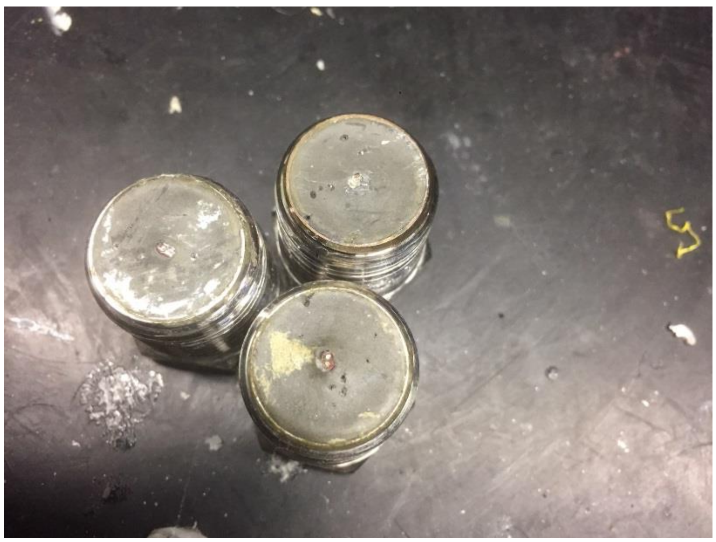

Figure 70. K-type potted thermocouple plugs, removed, showing the pressure side and nucleation sites.

The clearance rate on any given pressure test for these plugs never increased beyond 50%. Armed with this information, and painfully aware of operational failures to that point, on March 1, 2018, the Facility Manager authorized complete removal of the MFTs, along with pushing in wire tails in order to forge ahead with data collection. This represents a fundamental change in the instrumentation design of the Facility, and was therefore only done when absolutely necessary in order to produce usable data towards the facility’s mission. However, certain mitigating actions were taken in order to provide necessary functionality.

Supplemental Thermocouple Installation

Instrumenting the coolant channel with a thermocouple was not only of significant experimental value, it also provide very necessary information regarding SFSETF interior conditions. Specifically, they inform the administrative limits placed on internal temperature to protect the heater rod cladding.

It is therefore imperative to select another means by which interrogate that information. Blessedly, a previous modification to instrumentation ports in the upper plenum top cover plate, shown in Figure 71, provides access to a coolant channel as it joins the upper plenum. Figure 72 shows an overlay of the upper plenum top cover plate, and the coolant channel layout of the SFSETF (not to scale), in order to further illustrate the applied intervention.

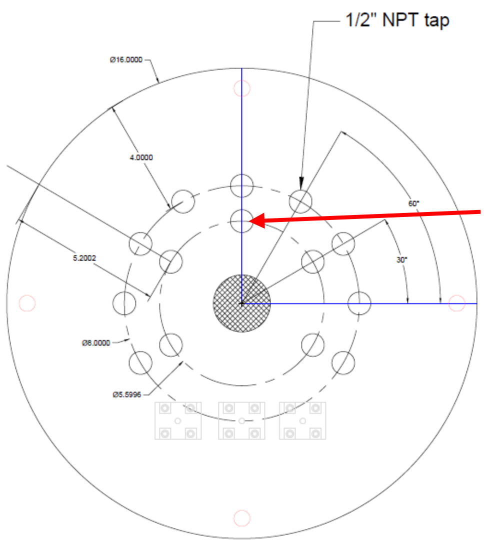

Figure 71. Upper plenum head plate cover port layout, with callout to instrumented coolant channel port.

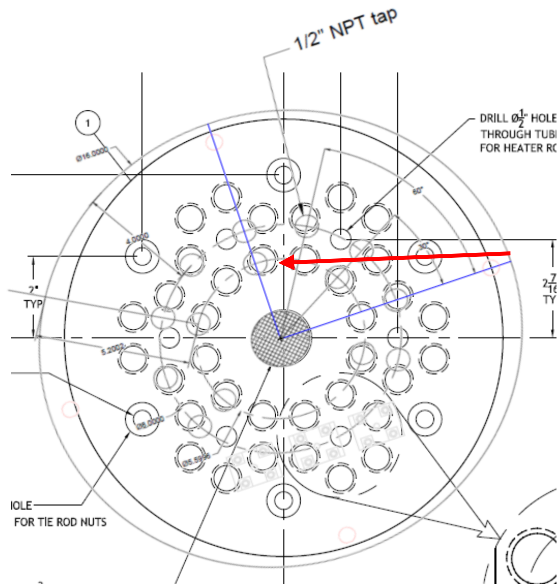

Figure 72. Upper plenum head plate cover and coolant channel overlay, with callout to instrumented coolant channel port.

A particular challenge should be noted with this reassignment. Because the positioning basket attached to the upper plenum cover plate is physically decoupled from the upper plenum top cover plate, the thermocouple is not assured to be in the centerline of the coolant channel. However, this is deemed acceptable for a number of reasons, provided below:

i. Due to the high elevation, there is unlikely to be laminar flow at any time during the execution of the experiment, according to the results of a boundary layer thickness scoping calculation [42]. Therefore distortion due to temperature profile is assumed to be minimal.

ii. Channel outlet data may be as useful, or more so, than centerline data at two points, with respect to providing state data on the interior void.

Moreover, this choice necessarily means that all Richardson number calculations from this data are no longer possible. Because all plugs were disconnected, no coolant channel surface data can be extracted, limiting the scaling value of the data somewhat. However, supplemental thermocouples may provide sufficient functionality and usable data, in the correct locations.

An additional k-type thermocouple was potted in bulkhead fitting 24, and was inserted at the same level as the upper plenum cover plate; and finally, thermocouples were placed in the T23 and T43 bulkhead fittings in order to interrogate the downcomer in opposing direction – nominally to capture any imbalances in core kinetics.

Table 29 provides the instrument ID, as called out in the data acquisition and control system (DACS), the previous instrumented location, and the new, amended location via bulkhead fitting.

Table 32. Bulkhead fitting reassignments for K-type thermocouples.

Instrument ID	*Previous Location*	*New Location*
TF-040	T24	Upper Plenum Port
TF-041	T34	T23
TS-01	T14	T24
TS-02	T44	T43

These thermocouples were routed in the simplest way possible, and using appropriately sized MFTs acting on the probe sheath, an effective pressure boundary was established. To demonstrate this fact, three different pressure tests were performed using helium as the working fluid. Nominally, tracking the pressure loss would provide an estimate of mass leakage, given that on may assume helium behaves as an ideal gas.

Mass Loss Calculation

Figure 73 shows the pressure trace from OT_041318_002, one of the pressurized shakedown test experiments. Overnight, it shows a loss rate of *9.37E-6 kPa/sec*, determined by performing a linear regression on the linear period of pressure loss. The results of this analysis, performed using STATA, are collected in Table 30. However, they are also presented in Equation B.04 for the sake of convenience.

$$\boldsymbol{P(t) = 117.152\ (\pm 1.29e-4) - (9.37e-6)(\pm 2.34e-9)} \times t \qquad \text{B.04}$$

Table 33. Summary of linear regression analysis of pressure trace results.

	Nom. Value.	*Std. Error*	*t*	*P>|t|*	*95% Conf. Interval*	
Coeff.	-9.37e-6	2.34e-9	-3997.52	0.000	-9.37e-6	-9.36e-6
Const.	117.152	1.292e-4	9.1e5	0.000	117.1517	117.1522

Of particular interest to this particular analysis, note the initial pressure increase. This is likely due helium relocation and heat transfer via conduction from the structural components in the upper plenum. The upper plenum features perpetually greater temperatures than the lower plenum due to the heater element in the oxygen sensor. As helium relocates from disruption, through engagement of the vacuum pump, relief valve opening, or through introduction of new material into the PPV, it interacts with the upper plenum to increase the pressure slightly throughout the system.

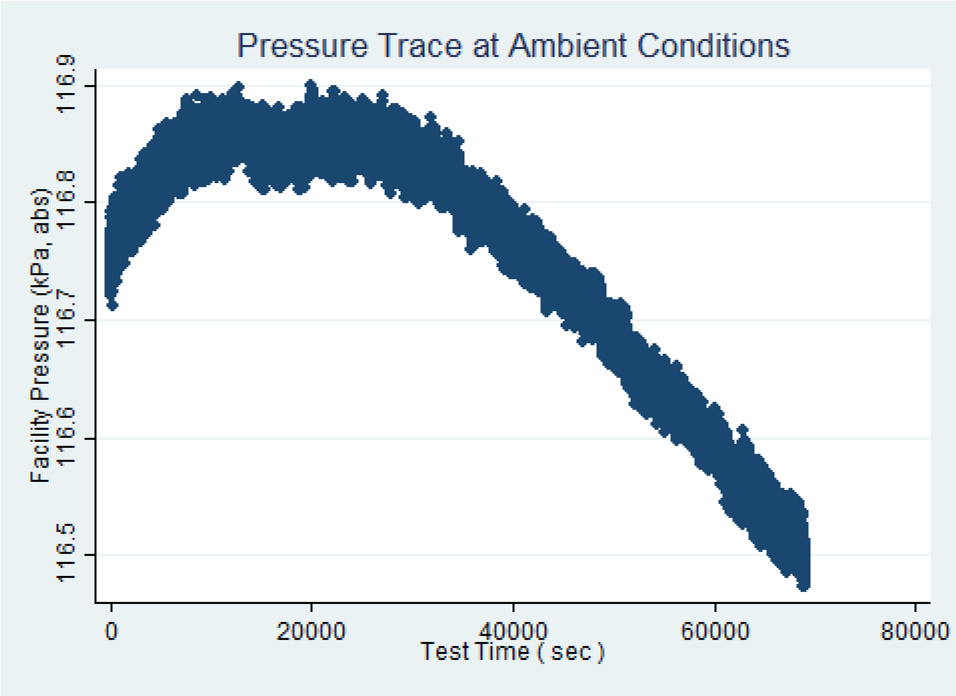

Figure 73. Overnight pressure trace from shakedown test results.

Figure 74 shows the linear region of that trace, between experiment time 40,000 sec and 69,029 sec (between hours 11.11 and 19.17). It is from this region that the loss rate above is calculated.

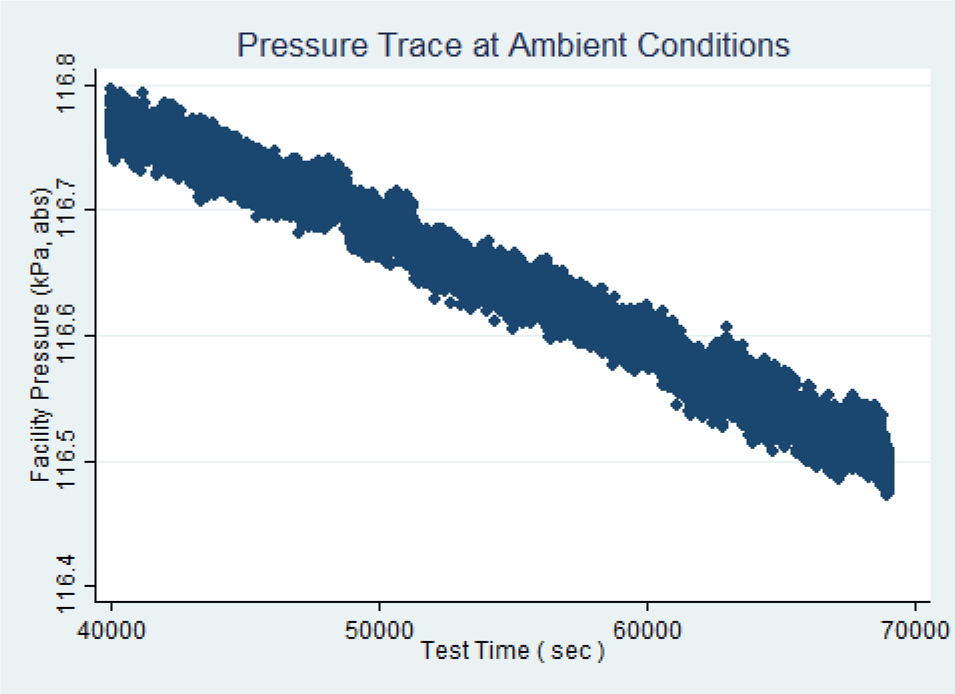

Figure 74. Linear pressure trace from shakedown test results.

Equation B.05 and .06 show the ideal gas equation, and the relation between pressure and mass loss.

$$\boldsymbol{PV = mR_{Sp}T} \qquad \text{B.05}$$

$$\boldsymbol{P = m \times \left(\frac{R_{Sp}T}{V}\right)} \qquad \text{B.06}$$

Taking the time rate of change of this equation, and assuming all other parameters remain constant, one soon finds, as in Equation B.07, that there is only a constant coefficient to relate them.

$$\boldsymbol{\frac{dm}{dt} = \frac{dP}{dt}\left[\left(\frac{R_{Sp}T}{V}\right)\right]^{-1}} \qquad \text{B.07}$$

The available void volume may be calculated to approximately 10200 in^3, or 0.167m^3. Further, if one determines the specific gas constant of helium to be: 2,077 J/(kg-K), then one may perform the calculation shown in Equation B.08.

$$\frac{dm}{dt} = \left(9.376e - 9\frac{Pa}{s}\right) \times (0.167\ m^3) \times \left(2,077\frac{J}{kg - K}\right) \times 300K \qquad \text{B.08}$$

$$= 9.765e - 4g/day$$

Equivalently, at operational pressures that comes out to approximately 5.4mL/day.

A similar analysis was performed after repositioning the cross duct, in order to qualify it for experimental use. Figure 75 shows the pressure trace from that experiment, while Equation B.09 presents the mass loss analysis. Table 31 presents the results of the linear regression analysis.

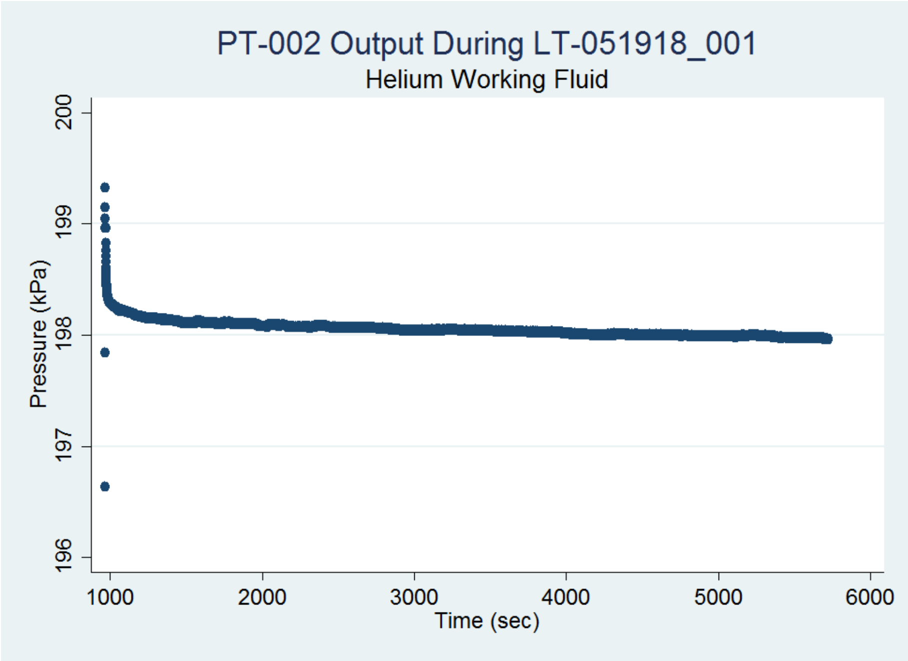

Figure 75. Pressure trace from Leak Test LT_051918_001, used to qualify the SFSETF for service.

Table 34. Summary of linear regression analysis of pressure trace results.

	Nom. Value.	*Std. Error*	*t*	*P>|t|*	*95% Conf. Interval*	
Coeff.	-3.08E-5	3.21E-8	-959.12	0.000	-3.08E-8	-3.09e-5
Const.	198.142	1.288e-4	1.5E6	0.00	198.14	198.14

$$\frac{dm}{dt} = \left(3.08e-8\frac{Pa}{s}\right) \times (0.167\, m^3) \times \left(2,077\frac{J}{kg-K}\right) \times 300K \qquad \text{B.09}$$
$$= 0.0032 g/day$$

While this represents a significant increase in the mass loss rate, as no bubbles were detected during the conduction of leak testing, it was accepted. For clarity, the mass loss rate in both configurations is presented in Table 32.

Table 35. Helium mass leakage rates in the SFSETF in various configurations.

Cross Duct High	0.9765 mg/day
Cross Duct Low	3.2 mg/day

For the sake of comparison with the NACOK facility, those rates correspond to holes in the pressure boundary corresponding to approximately 0.025mm and 0.046mm, respectively.

Power Line Penetrations

One of the final locations to experience persistent leaks, the power line pass-throughs were a particular challenge. Their geometry should be noted, as in Figure 76, which also shows the most commonly detected failure at this location. Of note, the pressurized fitting mates with a steel sheath that is crimped around the braided wire. This crimped sheath material also houses the potted line wires. It is impossible to remove these without removing the terminal blocks on the upper plenum, the oxygen sensor, all the UP thermocouples, and destroying the installed gasket. Essentially, an in-situ solution was required.

Figure 76. Power line pass-through, detailed view of the most common failure modality detected with bubble solution.

Thankfully, solid copper wire of the same gauge was spliced onto the mains line, and then covered with a dual wall heat shrink material. Specifically, adhesive-lined polyolefin from 3M was applied, along with silicone at joint locations to assure pressure seal.

Conclusion to Sealing Activities

Significant changes were made to the SFSETF in order to achieve an effective pressure seal. They are summarized as follows:

1. Installation of GRAPH-LOCK gaskets at the superior and inferior PPV flange faces (along with inferior and superior surface treatment with Copaltite).

2. Removal of k-type coolant channel thermocouple plugs.

3. Installation of k-type plugs with pressurized fittings acting on the probe sheath, acting at key locations.

4. Alteration of the power delivery lines to the SFSETF.

5. Inclusion of silicone and Copaltite in v-band clamp locations.

With these changes, the SFSETF is finally capable of holding pressurized helium, and features a nominal loss rate of 97.4 micrograms per day at operational conditions. Armed with this information, the SFSETF may begin an experimental program without fear of disruption via loss of test medium.

Thermal Inertia Calculations

To account for the stratified nature of the work, the following procedure was utilized to determine the applicable thermal inertia of the facility.

1. Draw a rough vacuum
2. Backfill with appropriate working fluid
3. Initiate data collection
4. Engage heater elements
5. Collect the upper plenum response
6. Using that data, calculate the linearized dT/dt, and with that, and the following equation, calculate the experimental thermal inertia.

$$\boldsymbol{Q_{in} = mc_p \frac{dT_{Upper\ plenum}}{dt}} \qquad \text{B.10}$$

Figure 77 shows a linear data selection from the power test data chosen to extract this information. Table 33 presents the results from the linear regression performed on that linear data selection.

Table 36. Linear regression results for thermal inertia data.

	Coefficient	*Std. Error*	*95% Conf. Interval*	*P>|t|*	*t*
Time	0.0386	8.38E-6	1.642E-5	0.000	4613.58
Constant	13.685	0.0117	0.0230	0.000	1165.95

$\boldsymbol{R^2 = 0.9994}$

For the sake of clarity, the model equation in shown in Equation B.11.

$$T(t)_{upper\ plenum} = \beta t + const. \qquad \text{B.11}$$

While there are energy leakage paths, this methodology is acceptable at low temperature ranges where the large thermal gradient necessary to drive conduction have yet to establish. This, combined with the mean power input of $\mathbf{723.6W \pm 0.448\ (6.196E-4)}$, to determine the thermal inertia, as shown in Equation B.12. The fractional uncertainties are combined in quadrature, *along with the instrumentation uncertainty*, to determine the following thermal inertia value when filled with air.

$$mc_{p,exp} = Q_{in} \div \frac{dT}{dt}_{upper\ plenum} = 1.873e4\frac{J}{C} \pm 0.0620\% \qquad \text{B.12}$$

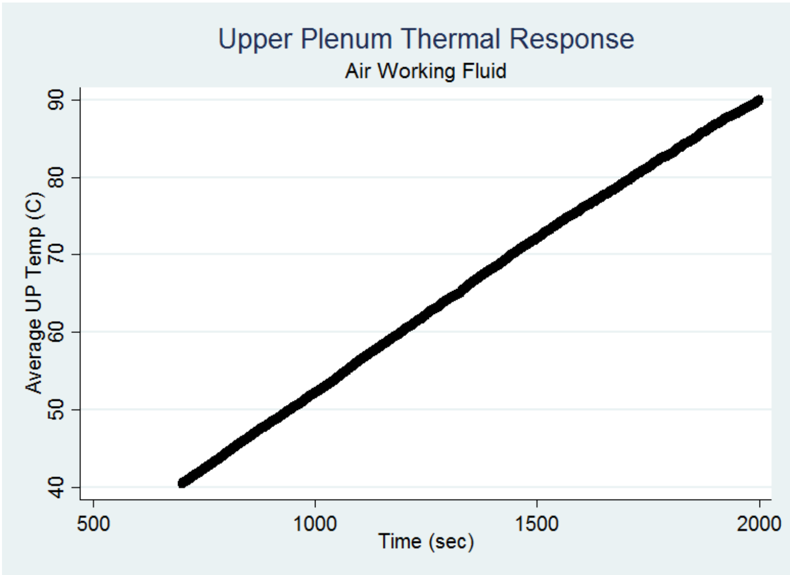

Figure 77 Average upper plenum thermal response from rest.

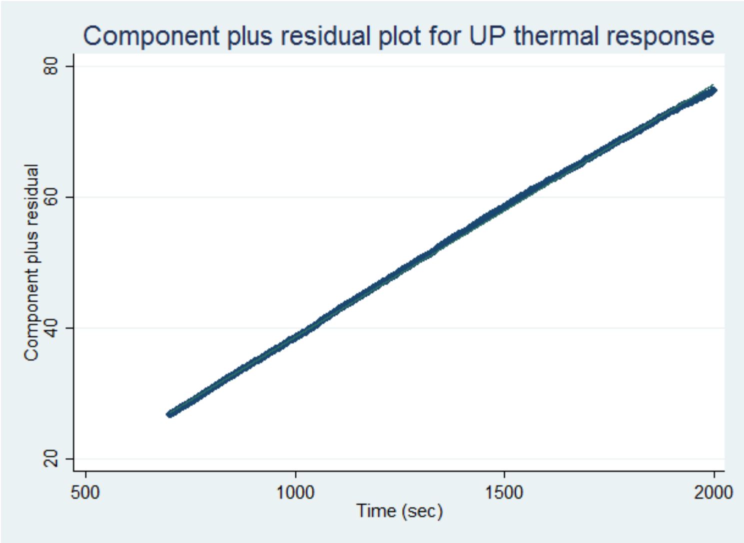

Figure 78. CPR plot showing the high degree of agreement between the model and test results.

The thermal leakage term may be calculated, as shown in Table 34.

Table 37. Results of the linear regression analysis performed on the thermal inertia data of the SFSETF upper plenum.

	Coefficient	*Std. Error*	*95% Conf. Interval*	*P>|t|*	*t*
Time	-0.0104	5.7E-6	1.117E-4	0.000	-1823.04
Constant	283.607	0.0666	0.130	0.000	4255.56

$R^2 = 0.9959$

7 *References*

[1] Framatome (AREVA), "AREVA HTGR Information Kit," Framatome (AREVA), 2014.

[2] Idaho National Laboratory, "NGNP Project Regulatory Gap Analysis for Modular HTGRs," INL, Idaho Falls, 2011.

[3] M. Hishida and K. Takeda, "Study on air ingress during an early stage of a primary-pipe rupture accident of a HTGR," *Nuclear Engineering and Design,* vol. 126, pp. 175-187, 1991.

[4] C. P. Liuo and e. al., "Stratified flows in horizontal piping of passive emergency core cooling systems," in *International Conference on Nuclear Engineering*, Beijing, 2005.

[5] C. Oh and E. Kim, "Air-ingress analysis: Part 1. Theoretical approach," *Nuclear Engineering and Design,* vol. 241, pp. 203-212, 2011.

[6] General Atomics, "Gas Turbine-Modular Helium Reactor (GT-MHR) Conceptual Design Descrtiption Report," General Atomics, San Diego, 1996.

[7] M. J. Fisher, M. H. Holmes and S. W. Chestnutt, "Fort St. Vrain desomissioning experience," in *Transaction of the Americal Nuclear Society*, Washington D.C., 1996.

[8] N. E. Todreas and M. S. Kazimi, Nuclear Systems I: Thermal Hydraulic Fundamentals, New York: Taylor and Francis, 1990.

[9] F. Bostelmann, G. Strydom, F. Reitsma and K. Ivanov, The IAEA coordinated research programme on HTGR unceratinty analysis: Phase I status and Ex. I-1 prismatic reference results, Nuclear Engineering and Design, 2016.

[10] J. M. Taylor, "Issues pertaining to the advances reactor and CANDU 3 designs and their relationship to current regulatory requirements," Washington D.C., 1993.

[11] S. Ball, M. Richards and S. Shepelev, "Sensitivity studies of air ingress accidents in modular HTGRs," *Nuclear Engineering and Design,* vol. 238, pp. 2935-2942, 2008.

[12] M. Holbrook, J. Kinsey and W. Moe, "Licensing Basis Event Selection Framework for Advanced Reactors," in *International Mechanical Congress and Exposition*, Phoenix, AZ, 2016.

[13] J. N. Reyes, J. T. Groome, B. G. Woods, B. Jackson and T. D. Marshall, "Scaling analysis for the high temperature Gas Reactor Test Section (GRTS)," *Nuclear Engineering and Design,* vol. 240, pp. 397-404, 2010.

[14] N. Zuber and e. al., "An integrated structure and scaling methodology for severa accident technical issue resolution: Development of methodology," *Nuclear Engineering and Design,* vol. 186, pp. 1-21, 1998.

[15] B. King, "Natural Circulation Scaling of a Pressurized Conduction Cooldown Event in the Upper Plenum of the Modular High Temperature Reactor," Oregon State University, Corvallis, 2012.

[16] R. Aldridge, "Scaling Study of the Depressurized Conduction Cooldown Event in the Hight Temperature Test Facility Using RELAP5-3D/ATHENA," OSU, Corvallis, 2013.

[17] I. Gutowska, "Study on Depressurized Loss of Coolant Accident and its Mitigation Method Framework at Very High Temperature Gas Cooled Reactor," Oregon State University, 2015, 2015.

[18] T. Schaaf, W. Frohling, H. Hohn and S. Struth, "The NACOK experimental facility for investigating an air ingress into the core of a high temperature reactor," *Kerntechnik,* vol. 63, pp. 107-112, 1998.

[19] Z. Zhang, H. Gerwin and W. Scherer, "Analysis of the Gas-Diffusion Process during a Hypothetical Air Ingress Accident in a Modular High Temperature Gas Cooled Reactor," *Institut fur Sicherheitsforschung un Reaktortechnik,* pp. 24-23, 1993.

[20] Idaho National Laboratory; Oak Ridge National Laboratory; Argonne National Laboratory, "Next Generation Nuclear Plans Research and Development Program Plan," INL, Idaho Falls, 2005.

[21] S. Chapman and T. G. Cowling, The mathematical theory of non-uniform gases; an account of the kinetic theory of viscosity, thermal conduction, and diffusion in gases, New York: Cambridge University Press, 1951.

[22] S. Shizowa, S. Fujikawa, T. Iyoku, K. Kunitomi and Y. Tachibana, "Overview of HTTR design features," *Nuclear Engineering and Design,* vol. 233, pp. 11-21, 2004.

[23] C. Oh, H. Kang and E. Kim, "Air-ingress analysis: Part 2-Computational fluid dynamic models," *Nuclear Engineering and Design,* vol. 241, pp. 213-225, 2011.

[24] J. J. Utberg, "Nitrogen Concentration Sensitivity Study of the Lock Exchange Phenomenon in the High Temperature Test Facility," Oregon State University, Corvallis, 2013.

[25] C. Oh, E. Kim, H. No and N. Cho, "Experimental Validation of Stratified Flow Phenomena, Graphite Oxidation, and Mitigation Strategies of Air Ingress Accidents," INL, Idaho Falls, 2009.

[26] D. Arcilesi, T. Ham, I. Kim, X. Sun, R. CHristensen and C. Oh, "Scaling and design analyses of a scaled-down, high-temperature test facility for experimental investigation of the initial stages of a VHTR air-ingress accident," *Nuclear Engineering and Design,* vol. 288, pp. 141-162, 2015.

[27] H. G. Jin, H. C. No and H. I. Kim, "Stratified flow-induced air-ingress accident assessment of the GAMMA code in HTGRs," *Nuclear Engineering and Design,* vol. 241, pp. 3216-3223, 2011.

[28] Oregon State SFSETF, "Oregon State SFSETF Instrumentation Plan," OSU, Corvallis, 2016.

[29] TSI Incorporated, "Air Velocity Transducer Model 8455 Operation and Service Manual," TSI Inc, 2013.

[30] T. Takeda and M. Hishida, "Studies on molecular diffusion and natural convection in a multicomponent gas system," *International Journal of Heat and Mass Transfer,* vol. 39, pp. 527-536, 1996.

[31] Bechtel et al., "Preliminary Safety Information Document for the Standard MHTGR," 1992.

[32] Idahon National Laboratory, "Prismatic Coupled Neutronics/Thermal Fluids Transient Benchmark of the MHTGR-350 MW Core Design Benchmark Definition," INL, Idaho Falls, 2010.

[33] S. Goodrich, "Natural Convection Heat Transfer and Boundary Layer Transition for Vertical Heated Cylinders," OSU, Corvallis, 2017.

[34] OSU-SFSETF-CALB-1300-001, "Procedure for Thermocouple Verification (completed)," OSU, Corvallis, 2016.

[35] Fluid Components International, "ST 100 Series Thermal Mass Flow Meter Installation, Operation and Maintenance Manual," Fluid Components International, San Marcos, 2015.

[36] American Society of Mechanical Engineers, "Measurement of Fluid FLow by Means of Thermal Dispersion Flow Meters," ASME, New York, 2011.

[37] D. Gould, D. Franken, H. Bindra and M. Kawaji, "Transition from molecular diffusion to natural circulation mode air-ingree in high temperature helium loop," *Annals of Nuclear Energy,* vol. 107, pp. 103-109, 2017.

[38] H. G. Jin, H. C. No and B. H. Park, "Effects of onset time of natural circulation on safety in an air ingress accident involving a HTGR," *Nuclear Engineering and Design,* vol. 250, pp. 626-632, 2012.

[39] OSU-SFSETF-TECH-005-001, "OSU SFSETF Instrumentation Description Report," OSU, Corvallis, 2017.

[40] OSU SFSETF, "Procedure to execute leak testing of the SFSETF facility," OSU, Corvallis, 2017.

[41] OSU SFSETF, "OSU-SFSETF-CALC-7140-001," Oregon State University, Corvallis, 2017.

[42] OSU SFSETF, "OSU-SFSETF-9130-CALC-02," Oregon State University, 2016.

[43] R. D. McCarty, "Thermodynamics Properties of He 4 from 2 to 500 K at Pressures to 10E8 Pa," *Journal of Physical Chemistry Reference Data,* vol. 2, no. 4, 1973.

[44] E. Lemmon, R. T. Jacobsen, S. F. Penoncello and D. G. Friend, "Thermodynamics Prperties of Air and Mixtures of Nitrogen, Helium, and Oxygen from 60 - 2000K and Pressure to 2000 MPa," *Journal of Physical Chemistry Reference Data,* vol. 29, no. 3, 2000.

[45] I. White, J. Fishler and A. Klein, "OSU-SFSETF-1200-CALC-001," Internal Use.

[46] Teledyne Analytical Instruments, "Model 9060 Zirconia Oxygen Analyser," Teledyna Analytical Instruments, 2006.

[47] J. Fishler and A. Klein, "OSU-SFSETF-0000-TECH-006," Oregon State University, Corvallis, 2015.

[48] Omega Engineering, "STRI Cartridge Heater Spec Sheet," OMEGA Engineering.

[49] S. Kakac and Y. Yener, Convective Heat Transfer, Boca Raton: CRC Press, 1995.

[50] K. Kadoya, N. Matsunaga and A. Nagashima, "Viscosity and Thermal Conductivity of Dry Air in the Gaseous Phase," *Journal of Physical Chemistry Reference Data,* vol. 14, pp. 947-970, 1985.

[51] E. Lemmon, R. Jacobsen, S. Penoncello and D. Friend, "Thermodynamics Properties of Air and Mixtures of Nitrogen, Argon, and Oxygen from 60 to 2000K at Pressure to 2000 MPa," *Journal of Physical Chemistry Reference Data,* vol. 29, no. 3, pp. 331-386, 1999.

[52] C. Hirt, S. Claessens, T. Fecher, M. Kuhn, R. Pail and M. Rexer, "New ultrahigh-resolution picture of Earth's gravity field," *Geophysical Research Letters,* vol. 40, no. 16, pp. 4279-4283, 2013.

[53] R. H. Nuun, Intermediate Fluid Mechanics, New York: Taylor and Francis Group, 1989.

[54] R. P. Wichner and B. S. J, "Potential Damage to Gas-Cooled Graphite Reactors Due to Severe Accidents," Orak Ridge National Laboratory, Orak Ridge, TN, 1999.

[55] D. G. Schweitzer and e. al, "Oxidation and heat transfer studies in graphite channels. I. The effect of airflow rate on CO2 and CO-O2 reactions.," *Nuclear Science and Engineering,* vol. 12, pp. 39-45, 1962.

[56] S. e. e. f. a.-i. i. h. f. vessel, "Kim, S; Yadav M S; Talley, J D; Ireland, A; Bajorek, S," *Experimental Thermal and Fluid Science,* vol. 49, pp. 1-13, 2013.

[57] A. Kadak and T. Zhai, "Air ingress benchmarking with computational fluid dynamics analysis," *Nuclear Engineering and Design,* vol. 236, pp. 587-602, 2005.

[58] D. Franken, D. Gould, P. Jain and H. Bindra, "Numerical study of air ingress transition to natural circulation in a high temperature helium loop.," *Annals of Nuclear Energu,* vol. 111, pp. 371-378, 2018.

[59] B. Woods, I. Gutowska and H. Chiger, "Scaling Studies for Advanced High Temperature Reactor Concepts, Final Technical Report: October 2014-December 2017," Unitder States, 2018.

[60] R. J. Lowe, J. W. Rottman and P. F. Linden, "The non-Boussinesq lock-exchange problem. Part 1. Theory and experiments.," *Journal of Fluid Mechanics,* vol. 537, pp. 101-124, 2005.

[61] M. Gradecka, "Modification of Lower Plenum Structure for Mixing Promotion during Normal Operation of the High temperature Gas Cooled Reactor," Oregon State University, Corvallis, 2015.

[62] S. Cadell, "Development of a Bindary Mixture Gas Composition Instrument for Use in a Confined High Temperature Environment," Oregon State University, Corvallis, 2012.